WEAK SHOCKS IN OPEN-ENDED DUCTS WITH COMPLEX GEOMETRY

Thesis by

James Eldon Craig

In Partial Fulfillment of the Requirements
for the Degree of
Doctor of Philosophy

California Institute of Technology
Pasadena, California

1977

(Submitted April 15, 1977)

ACKNOWLEDGMENTS

I am indebted to AMF/Harley-Davidson Motor Company and to Nelson Industries, Incorporated, who sponsored this project; and to Dr. Edmund Lary, Central Technical Staff, AMF Incorporated, for his role in developing the sponsorship.

Professors Anatol Roshko, Fred Culick, Gerald Whitham, and Paul Jennings offered useful evaluations of the thesis, improving its content and scope.

Professor Bradford Sturtevant has provided continual support during my five years at Caltech. His direction and guidance of my work was particularly helpful, as was his assistance in preparing my thesis.

The efforts of Mr. Earl Dahl and Mr. Vince Sodha for the many hours of lab and computer work, and of Mrs. Karen Cheetham for proofreading early versions of the thesis, will always be appreciated. Thanks to Mrs. Susan Dycus for her accurate typing of the final thesis. Mrs. Jacquelyn Beard's moral support was a continual source of optimism.

Lastly and mostly, I thank my wife Gyni for moments and thoughts that I will cherish forever.

ABSTRACT

The dynamics of weak shocks in ducts of complex geometry and the sound radiation produced by the reflection of a weak shock from the open end of a duct have been investigated. Duct geometries include expansion chambers with and without inlet or outlet tubes extended and enclosed perforated tubes. Internal and external pressure histories of the interaction of weak shocks with simple muffler elements have been recorded using a standard one-shot shock tube and a resonating shock-tube. The excitation shock Mach number ranged from 1.05 to 1.55. Analytical investigations, including a synthesis of existing works on internal weak-shock interactions and an acoustic treatment of the sound radiation produced by weak shock waves, are presented. Combining the above analyses, models for the reduction in radiated sound per unit of incident shock amplitude, as a result of inserting a muffler between the source and the tailpipe exit, are developed.

For expansion chambers with and without extensions, the dependence of the transmitted and reflected waves and of the radiated sound on area ratio is compared with predictions. In particular, measured transmission coefficients for expansion chambers agree reasonably well with the predictions for all shock strengths; however, for large area ratios, the predicted sound attenuation is not observed, as waves diffracted at the upstream junction cause more sound to be radiated. For expansion chambers with internal extensions, sound attenuation is increased for low incident shock strengths; while for increasing incident shock strength, the internal transmission characteristics deteriorate, thus reducing the sound attenuation.

For enclosed perforated tubes, the dependence of the transmitted and reflected waves and of the radiated sound on perforate area ratio and incident shock strength is compared with predictions. For perforated tubes with infinite enclosure, the transmission and reflection coefficients depend on both incident shock strength and perforated area ratio, as predicted. However, agreement with data is obtained only after inserting a perforation discharge coefficient with the perforated area ratio in the theory. The reduction of sound radiation with perforated area ratio is measured for one incident shock strength and then compared with predictions. For small area ratios, there is agreement but for large area ratios the measurements show that less sound is radiated than predicted. For large area ratios, gradual compressions with smooth fronts (not shock fronts) are transmitted, resulting in less radiated sound. Enclosures have no effect on the sound attenuation for small perforate area ratios; however, as the perforate area ratio increases, the enclosure eventually inhibits further increase in sound attenuation.

TABLE OF CONTENTS

Part	Title	Page
	Acknowledgments	ii
	Abstract	iii
	Table of Contents	v
	List of Figures	vii
I.	Introduction	1
1.1	Interaction of Shocks with Discrete Muffler Elements	5
	1.1.1 Discontinuous Area Changes	10
	1.1.2 Extensions	10
	1.1.3 Perforations	12
	1.1.4 The Open End	18
1.2	The Experiment	19
	1.2.1 Experimental Facilities	19
	1.2.2 Shock Pulse Excitation	22
	1.2.3 Acoustical Analysis of Test Mufflers	25
II.	Experiment	28
2.1	Experimental Facilities	28
	2.1.1 Resonance Tube	28
	2.1.2 GALCIT Six Inch Shock Tube	28
2.2	Muffler Description and Instrument Location	32
2.3	Data Acquisition and Handling	36
	2.3.1 Repetitive Pulse Excitation	36
	2.3.1.1 Periodic Signals and the FFT	44
	2.3.2 Single Pulse Excitation	48
2.4	Transducer Calibration	50
III.	Analysis	52
3.1	Introduction	52
3.2	Perforated Tubes	53
3.3	Discontinuous Area Changes	59
	3.3.1 Individual Elements	59
	3.3.2 The Expansion Chamber	63
3.4	Extensions	66
	3.4.1 Outlet or Inlet Extensions	66
	3.4.2 Expansion Chamber with Inlet Extension	70
	3.4.3 Expansion Chamber with Outlet Extension	73
3.5	Sound Radiation From Open Pipes	76
	3.5.1 Radiated Wave Forms	76
	3.5.2 Radiated Sound Pressure Levels	85

TABLE OF CONTENTS (Cont'd)

Part	Title	Page
IV.	Results-Internal Waves	89
	4.1 Perforations	89
	4.1.1 Wave Forms	90
	4.1.2 Wave Amplitudes and Empirical Data	98
	4.1.3 The Effects of Mean Flow	110
	4.1.4 Finite Enclosures	115
	4.2 Expansion Chambers	122
	4.2.1 Wave Forms	123
	4.2.2 Wave Amplitudes	131
	4.2.3 The Effect of Mean Flow	136
V.	Results-External Waves	142
	5.1 Sound Radiation From Open Pipes	142
	5.1.1 Radiated Wave Forms	142
	5.1.2 Wave Amplitudes	146
	5.2 Sound Attenuation by Perforated Tubes	154
	5.2.1 Wave Forms	155
	5.2.2 Radiated Sound Pressure Levels	158
	5.3 Sound Attenuation by Expansion Chambers	161
	5.3.1 Wave Forms	162
	5.3.2 Radiated Sound Pressure Levels	162
VI.	Summary of Results	170
	6.1 Internal Waves	170
	6.1.1 Perforations	170
	6.1.2 Expansion Chambers	170
	6.2 External Waves	172
	6.2.1 Perforations	172
	6.2.2 Expansion Chambers	173
	6.3 Applications	173
Appendix A	Numerical Solution of Second Order Equations	175
Appendix B	Shock Tube Data Handling Program	178
Appendix C	Estimation of Initial Test Section Conditions in Resonance Tube	180
	References	182

LIST OF FIGURES

1. Muffler Elements
2. Shock Interaction with a 90^{o} Step
3a. Shock Interaction with an Extended Inlet
3b. Shock Interaction with an Extended Outlet
4. Shock Interaction with a Perforated Duct
5. The Sound Produced by the Reflection of a Weak Shock from the Open End of a Circular Duct
6. The Geometry of Experimental Facilities
7. Comparison of Resonance Tube and Motorcycle Engine Pressure Wave Forms
8. Muffler Systems
9. Resonance Tube Facility
10. GALCIT Six Inch Shock Tube
11. Pressure Traces: Resonance Tube and Shock Tube
12. Perforation Systems
13. Expansion Chamber Systems
14. Interfacing Timing Diagram
15. ADC Controller
16. Phase-Locked Loop
17. Computer Programs
18. Wave Form and Spectrum
19. Transducer Calibration
20. Wave Diagram for Perforations
21. Wave Diagram for Area Expansion
22. Amplitude Dependence
23. Expansion Chamber System
24. Wave Diagram for Area Expansion with Inlet Extension

LIST OF FIGURES (Cont'd)

25. Wave Diagram for Area Contraction with Outlet Extension

26. Extended Inlet System

27. Extended Outlet System

28. Coordinates in Tailpipe Exit
28a. Radiated Pressure History
29. Effect of Perforate Area Ratio on Transmitted and Reflected Waves

30. Effect of Perforate Area Ratio on Transmitted and Reflected Waves

31. Effect of Incident Shock Mach Number on Transmitted and Reflected Waves

32. An X-T Diagram for the Propagation of Weak Shocks Past Long Sections of Perforations

33a. Transmission Coefficients of Perforated Tubes for Shock Mach Numbers

33b. Reflection Coefficients of Perforated Tubes for Shock Mach Numbers

34. Total Pressure Loss Across Perforated Tubes

35. Discharge Coefficients of Perforated Tubes

36. Transmission and Reflection Coefficients for Perforated Tubes, Data and Theory

37. Transmission and Reflection Coefficients for Perforated Tubes, Data and Theory

38. Transmission and Reflection Coefficients for Perforated Tubes, Data and Theory

39. Transmission and Reflection Coefficients for Perforated Tubes, Data and Theory

40. Transmission and Reflection Coefficients for Perforated Tubes, Data and Theory

41. Pressure Histories of Shock Propagation Past Perforated Tubes Without Enclosures, Repetitive Excitation

42. Transmission and Reflection Coefficients of Perforated Tubes,

LIST OF FIGURES (Cont'd)

with and without Enclosures

43. Initial Test Section Velocity, Repetitive Excitation

44. A Proposed Model of the Interaction of a Shock Wave with Enclosed Perforations

45. Pressure Histories of Shock Propagation Past Perforated Tubes

46. Pressure Histories of Shock Propagation Past Perforated Tubes

47. Pressure Histories of Shock Propagation Past Perforated Tubes

48. Pressure Histories of Shock Propagation Through Expansion Chamber B

49. Pressure Histories of Shock Propagation Through Expansion Chamber B with Inlet Extension

50. Pressure Histories of Shock Propagation Through Expansion Chamber B with Outlet Extension

51. Pressure Histories of Shock Propagation Through Expansion Chamber C

52. Transmission and Reflection Coefficients of Expansion Chambers

53. Transmission and Reflection Coefficients of Expansion Chambers with Inlet Extensions

54. Transmission Coefficients of Expansion Chambers with Outlet Extensions

55. Transmission Coefficients of Expansion Chambers

56. Reflection Coefficients of Expansion Chambers with and without Inlet Extensions

57. Transmission Coefficients of Expansion Chambers with Inlet Extensions

58. Transmission Coefficients of Expansion Chambers with Outlet Extensions

59. Radiated Pressure Histories of Shocks Propagating out of Circular Tubes

60. Radiated Pressure Wave Forms: On Tube Axis and at 90^{o} to Tube Axis

LIST OF FIGURES (Cont'd)

61. Radiated Pulse Amplitudes

62. Transducer Range and Identification

63. Radiated Pulse Amplitudes

63a. Shock Waves Through Discontinuous Area Changes

63b. On Axis Pressure Decay

64. Pressure Histories of Shock Propagation Past a Perforated Tube

65. Sound Attenuation by Perforated Tubes

66. Sound Attenuation by Perforated Tubes

67. Sound Attenuation by Expansion Chambers

68. Sound Attenuation by Expansion Chambers

69. Sound Attenuation by Expansion Chambers with Inlet Extensions

70. Sound Attenuation by Expansion Chambers with Outlet Extensions

71. Sound Attenuation by Expansion Chambers with Inlet or Outlet Extensions

INTRODUCTION

There exist many industrial products which create intense periodic, aperiodic, or transient sound and cause some very challenging design problems for the engineer. It is well known that as a consequence of fundamental nonlinear effects in fluids, shock discontinuities are formed in intense sound fields. Recently, disciplines such as nonlinear acoustics, jet propulsion, transonic and supersonic fluid mechanics, and more applied portions of the engineering industry, have been confronted with problems involving shock wave propagation. Some cases in which shock propagation is an important phenomenon are sonic boom, blast wave, jet engine noise, rocket motor instability, electric discharge lasers, valve noise, cavitation, and small internal-combustion engines. This paper specifically addresses the problem of propagation and suppression of steep-front pulses observed in the exhaust systems of small high-performance internal-combustion engines.

The exhaust systems used on small high-performance internal-combustion engines can be designed to utilize the strong pressure pulse generated by the "fast" opening time of the exhaust port or valve to enhance scavenging of combustion products and, in the case of two-cycle engines, to supercharge the combustion chamber. Consequently, a well-designed exhaust system can cause remarkably large increases of the power developed by the engine. Nomura and Naitoh (1971) report that two-cycle engine performance is greatly affected by the exhaust system and that the exhaust system accounts for a substantial portion of the 350 bhp/liter (5.74 bhp/cubic inch) attained by their four cylinder, 1/8-liter, two-cycle racing engine. At peak rpm the exhaust port in their engine opens completely in less than one millisecond. The large rate of increase of mass flux associated with fast port opening time creates the steep-front compressive disturbance driven from the exhaust port. The pressure jump is of the order of one atmosphere. Reflections of the pressure pulse are utilized to enhance engine performance.

Noise pollution, caused by motorcycles, chain saws, etc., has developed into a major public issue. The basic problem is that to develop high specific power output, an engine must have high cylinder pressure levels and fast opening exhaust valves. Consequently, the exhaust pulses have a large amplitude and a steep front. In fact, when nonlinear effects are important, the fronts will steepen sufficiently to be treated as shock discontinuities.

The sound radiation from the outlet of these exhaust systems is characterized by a source strength. For acoustic point sources, it is known that the radiated pressure field is directly proportional to the time rate of change of volume flux from the source (Morse and Ingard, 1968). Therefore, the source strength for the sound radiation by shock waves has two important parameters, which are the amplitude and thickness of the shock. Clearly, by weakening or thickening the shock, the sound radiation is reduced.

Generally, the shock strength is only affected by the duct geometry. It is known from geometrical acoustics (Whitham, 1974) that weak shocks will strengthen in duct contractions and weaken in duct expansions. Two area change configurations are discussed in this paper, namely, discontinuous area changes and discontinuous area changes with extensions (Fig. 1). Also, perforations in the side wall of a duct (Fig. 1) weaken the shock, as the fluid behind the shock will leak through the perforations. In addition to weakening the shock, perforations which extend for several duct diameters can thicken the shock.

Existing muffler technology, which was introduced by Stewart (1930), models the engine as an independent sound source and the exhaust system as an idealized acoustic transmission line. The acoustic theory predicts muffler performance quite well when the muffler is excited by sinusoidal waves of infinitesimal amplitude (Sachs and Allen (1972), Alfredson and Davies (1971), and Davis (1954)). Conversely, the acoustic theory does not predict the muffler performance when the muffler is excited by actual exhaust pulses. This discrepancy is caused by finite amplitude effects, particularly when shock discontinuities are formed in high-performance exhaust systems.

A single pulse theory for muffler design which confronts the problem of dealing with the steep-front disturbance was conceived by Davies (1964). The basic concept of the single pulse theory is that the interaction of the discontinuity in the exhaust pulse with individual muffler elements can be taken as an isolated event, independent of the existing fluid motions in the rest of the exhaust system. Then, simple models of shock wave interactions with muffler elements can be compiled. A shock wave muffler theory can be developed, in place of acoustic theory, to be used when the amplitudes of the exhaust pulses are significant.

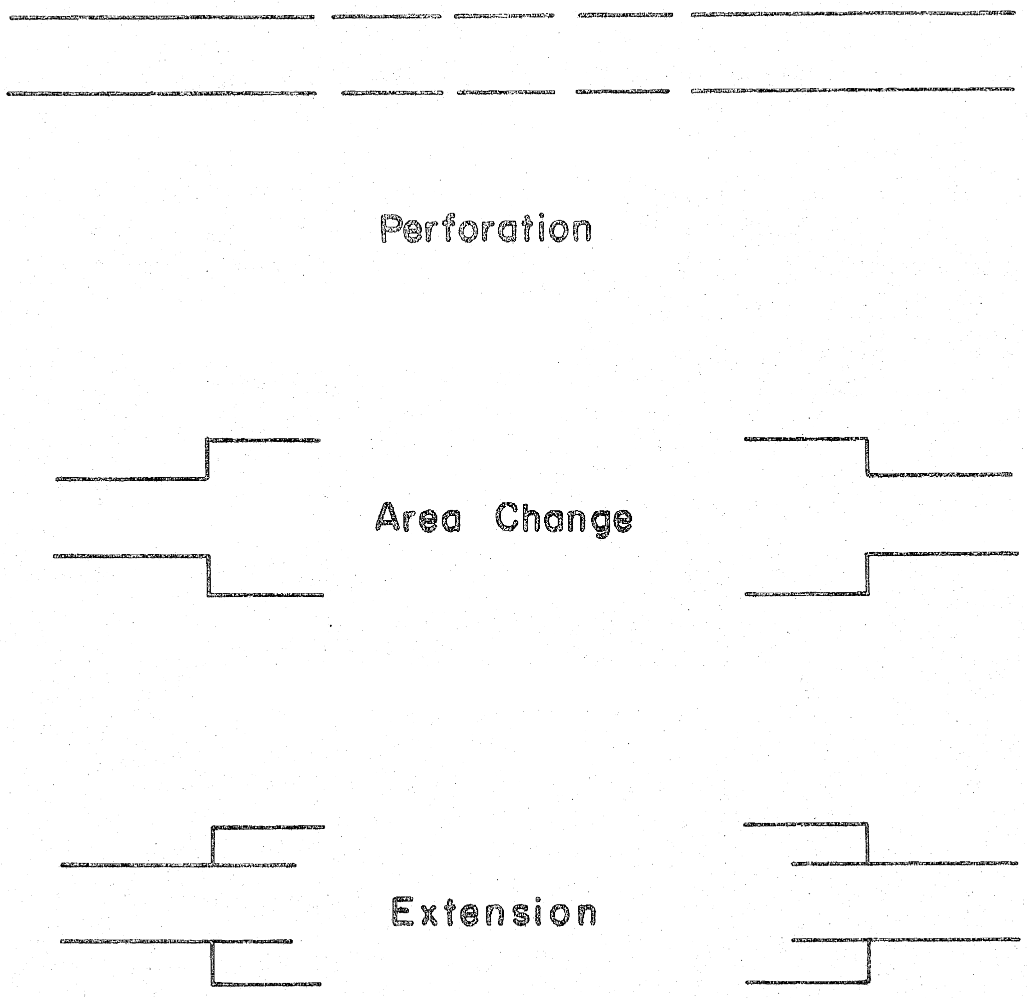

FIGURE I MUFFLER ELEMENTS

By using the shock wave to model the actual exhaust pulse instead of a sinusoidal disturbance, one can readily account for non-linear effects which are not in the acoustic theory.

Nonlinear phenomena which are important in exhaust systems include (1) the steepening of progressive waves, causing discontinuities to form, and (2) the local Mach number induced by the shock wave, causing the effects of compressibility and Reynolds number to be important. These phenomena are particularly important in muffler systems in two ways: (1) a discontinuity can be formed in the initial pulse after propagating only a short distance from the exhaust port, and (2) resonances in cavities or enclosures develop, causing the appearance of asymptotic wave forms which contain discontinuities. The local Mach number affects the fluid motions in mufflers when the dynamic pressure becomes a significant quantity, and Reynolds number effects may occur because shock waves certainly interact with boundary layers and may interact with separated and turbulent flow.

The basic geometries investigated in this work constitute fundamental components of existing, more complex systems. In general, the mechanism of sound attenuation utilized by most muffler systems can be categorized as reflection or dissipation of the energy in the shock. There are, no doubt, a large number of duct geometries which will produce sound attenuation; however, since the details of the mechanism are many times quite similar, there is much to be learned in a careful study of the basic geometries.

1.1 Interaction of Shocks with Discrete Muffler Elements

Of the many types of muffler elements available, three simple yet basic geometries are discussed in this paper (Fig. 1): those composed of tubes with a) orifices in the walls, b) discontinuous changes in cross-sectional area, and c) tubes extending beyond discontinuous changes in cross-sectional area.

To develop models for the interaction of a shock wave with a muffler element, let us examine two stages of the interaction: (1) the short time or transient behavior, and (2) the asymptotic conditions.

In general, for short times the interaction is between the shock and the transient waves created by the arrival of the shock at the muffler element. A long time after the arrival of the shock the transient waves have interacted with the shock, and the flow past the element is steady. Rudinger (1957) first proposed that the time for steady flow conditions to be established after the arrival of a plane shock wave at a junction in a tube would be non-zero and closely associated with the local acoustic travel time across the width of the duct. In particular, Rudinger determined the time for the steady conditions to develop following the arrival of a plane shock wave at the open end of a circular pipe was equivalent to the time in which a sound wave travels three exit diameters.

A similar approach to the understanding of the short-time behavior of the shock wave interaction with a muffler element can be discussed in terms of ideas about wave diffraction. When a plane shock, whose strength is constant along its front, propagates into a motionless fluid, the pressure field behind the shock is constant and is given by the shock strength. Conversely, when variations in the shock strength exist along its front, variations in pressure are left in the fluid behind the shock. In particular, when a shock passes over a step (Fig. 2), waves are created behind the shock front, causing variations in shock strength along its front. Since the shock propagates at a speed given by the local Mach number, the shock is no longer plane. For an expansion corner, waves behind the shock front cause it to curve away from itself. The waves in the nonsteady flow are termed diffraction waves and act to smooth the pressure field behind the shock.

Thus, when a discontinuity in shock strength occurs on the shock front, a wave front, which acts to smooth the pressure field behind the shock,is diffracted radially from the point of origin. Diffracted wave fronts can of course be of either sign; the portion of the wave diffracted into high-pressure region is an expansion, which acts to lower the pressure, while the portion of the wave diffracted into low-pressure region is a compression, which acts to raise the pressure. The expansion portion will not lead to a discontinuity in shock strength along its front, but it may be thin enough to be treated as a discontinuity. For an expansion corner, the diffracted wave front extends from the back side of the corner, 3, to the front side, 1, and intersects with the incident shock at 2. The expansion portion of the wave front propagates into the high-pressure region at the local speed of sound relative to the fluid in region two. The compression portion of the wave front propagates into the undisturbed fluid in region one in a direction normal to the local front at a speed given by the local Mach number.

If the shock and the diffracted wave front propagate at the undisturbed speed of sound, a_1, the diffracted wave front forms a circle of radius a_1t at time t. Further, the shock intersects the diffracted

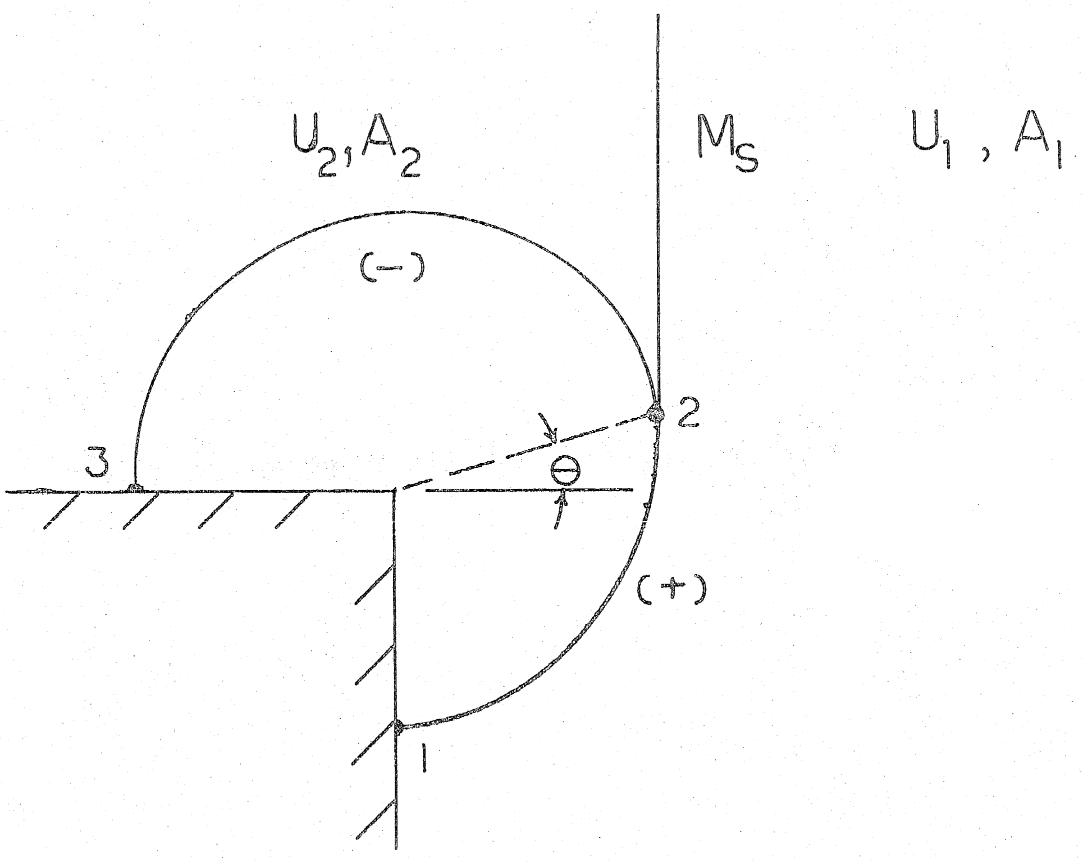

FIGURE 2 SHOCK INTERACTION WITH A 90° STEP

wave front at the point of tangency. This of course is not the true case for waves of finite amplitude; disturbances created behind a shock always overtake the shock because of the increase in the speed of sound and the effects of convection behind the shock. As a result of these nonlinear effects, the expansion portion of the wave front overtakes the shock front and their intersection propagates along the shock front with a nonzero velocity, c*. The velocity of intersection 2 along the shock front is given quite simply from a kinematics argument, by noting that relative to fluid in region two, intersection 2 has a radial velocity, a_2, and a horizontal velocity $(M_s \cdot a_1 - u_2)$. Thus, intersection 2 propagates along the shock front at speed $c^* = \left(a_2^{\,2} - (M_s a_1 - u_2)^2\right)^{\frac{1}{2}}$. These quantities are all functions of the shock Mach number, M_s, so that θ_2 is given for an expansion corner by the shock Mach number. For weak shocks θ_2 is equal to $\arctan \left(2(M_s - 1)/M_s^{\,2}\right)^{\frac{1}{2}}$. Because the shock strength decreases from point 2 to point 1, the curvature of the wave front changes between points 2 and 1. The theory of shock dynamics is discussed at length by Whitham (1957); here it is important only to see how the waves behind the shock interact with the shock and modify its strength. The shock remains plane above intersection 2.

With this brief discussion of the shock interaction with an expansion corner and the nonlinear effects which act to modify the incident shock, we may qualitatively examine how the diffracted wave fronts act to establish steady conditions at the junction of muffler elements. These steady conditions fix the asymptotic strength of the reflected and transmitted waves.

1.1.1 Discontinuous Area Changes

In particular, when the cross-sectional area increases, the diffracted wave front must look quite similar locally to the wave front in figure 2. However, an additional feature of this problem is that the transverse dimension of the duct is limited, so the diffracted wave fronts reflect from the side walls of the tube as they propagate in the upstream or downstream direction. Eventually flow conditions far upstream and downstream of the area change must be related by these steady conditions. When the junction is a discontinuity in cross-sectional area, the one-dimensional conditions relating the upstream and downstream fluid properties are (1) the change in mass flux across the junction is zero and (2) the change in momentum flux is balanced by the force on the junction.

1.1.2 Extensions

Extensions of the inlet or outlet pipe into a discontinuous change of area (Fig. 1) has been shown to improve acoustic muffler performance (Davis, 1954). Shock wave interaction with area changes can also be altered by extending the inlet or outlet pipe.

When a shock arrives at an area expansion with the inlet pipe extended, the wave front is diffracted as shown in figure 3a. Since a portion of the incident shock is diffracted into the annulus, the wave transmitted downstream is weaker than the equivalent wave transmitted from a discontinuous or standard area change. The diffracted wave front in the annulus reflects from its end toward the end of the extension. The result is that an infinite series of waves propagate in the upstream and downstream directions from the end of the extension.

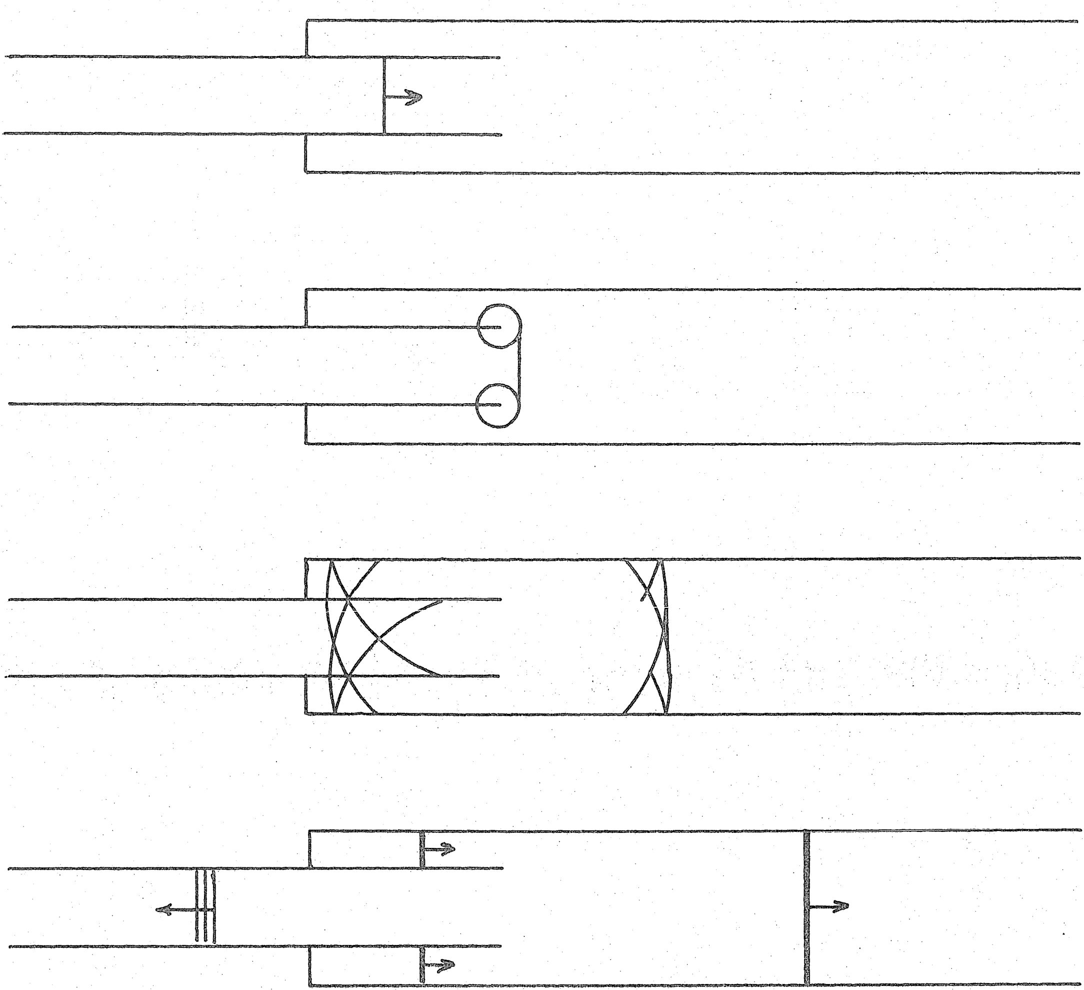

FIG. 3a SHOCK INTERACTION WITH AN EXTENDED INLET

When a shock arrives at an area contraction with the outlet pipe extended, a portion of the shock is passed through the junction without amplification (Fig. 3b). The extension of the outlet pipe at an area contraction is denoted a "cookie cutter." The rest of the shock reflects from the closed end of the annulus toward the end of the extension. When the wave in the annulus arrives at the end of the extension, a wave is propagated upstream and downstream and a wave returns into the annulus. Hence, an infinite series of waves propagate upstream and downstream from the end of the extension.

Therefore, extending the inlet pipe into an area expansion increases the attenuation caused by the area change; and extending the outlet pipe into an area contraction eliminates the amplification. This point is important because we will later find that even though a series of waves is transmitted, they will produce less sound than the wave transmitted when the area change has no extension.

1.1.3 Perforations

The last muffler element to be discussed is a tube with a perforated section. There are basically three types of walls: (1) porous wall, (2) thin wall, and (3) thick wall. In flows through porous walls, friction effects dominate and dynamic effects are negligible. Thin-wall and thick-wall perforations have large and small hole-diameter-to-wall-thickness ratios, respectively. The fluid leaving the tube through a thin-wall perforation is turned only slightly toward the axis normal to the orifice, whereas the flow through a thick-wall perforation is turned nearly parallel to the axis normal to the orifice.

Shock waves interact with perforated tubes because fluid is

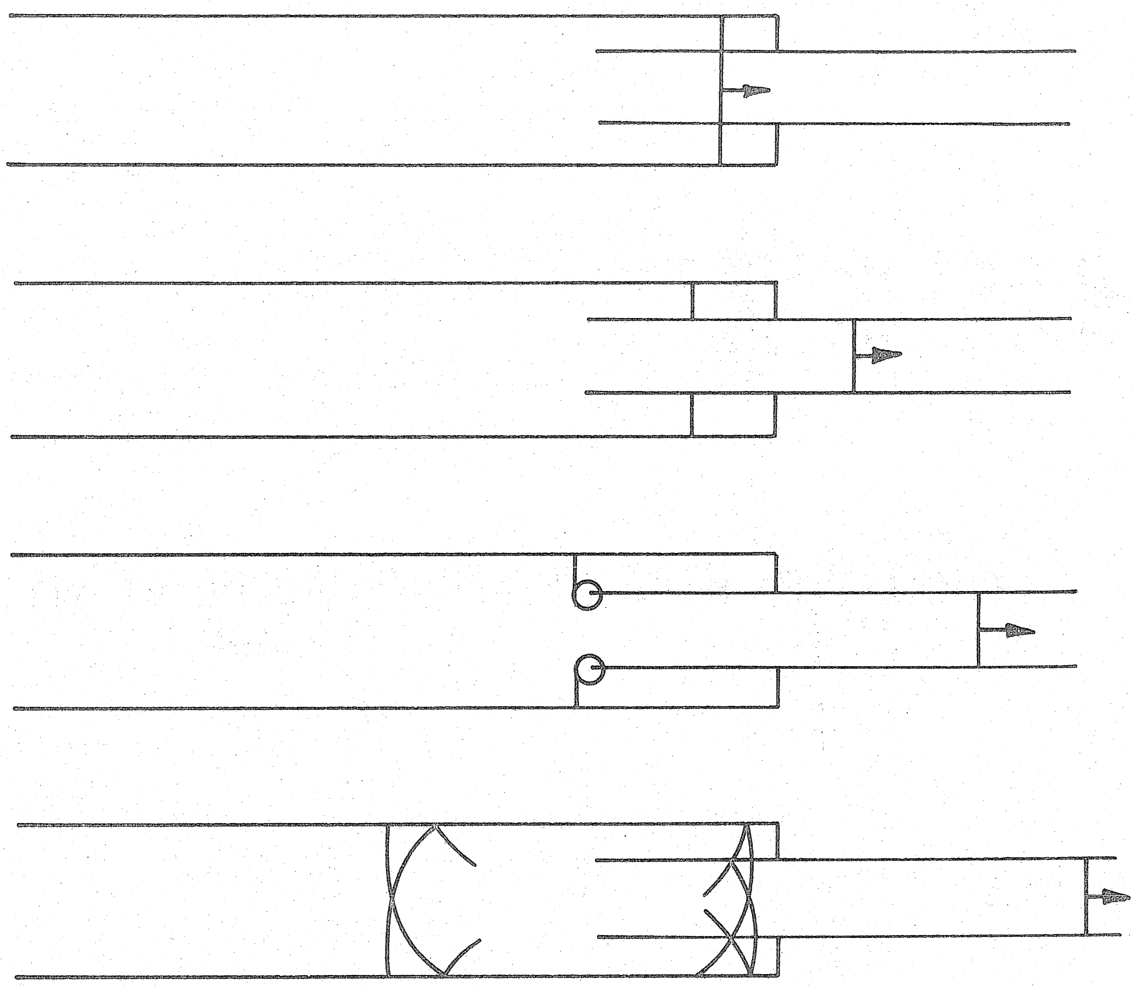

FIG. 3b SHOCK INTERACTION WITH AN EXTENDED OUTLET

pumped through the perforations when the shock wave increases the pressure inside the tube. The key effect is the mass removal through the perforated wall. As before, steady conditions at the perforations are established by a complicated series of diffracted wave fronts passing across the perforation. Two excellent spark schlieren pictures were published by Wu and Ostrowski (1971) depicting the interaction of a shock wave with a wall with a single slit and a uniform perforation, respectively.

The picture of the shock wave passing the slit shows the transient behavior of the diffracted waves. These diffracted waves establish the steady mass flow through the slit and weaken the shock by propagating across the backside of the front shock. When the perforations are uniformly distributed along the wall, each orifice interacts with the shock wave by increasing the amount of fluid which is being removed behind the shock.

The attenuation of plane shock waves, propagating in ducts with uniformly distributed perforations, has been numerically approximated by Rosciszewski (1959), Szumowski (1972), Wu and Ostrowski (1971), and Honda (1974).

The first three of these authors used a method based on the formulation of Whitham (1957) for shock propagation in nonuniform ducts. The common use of the approach merits some comment on the formulation.

One-dimensional nonsteady equations of motion are written in characteristic form including the effects of some kind of nonuniformity, which changes slowly along the duct. These authors have replaced the nonuniformity due to varying area with one due to mass flow through the tube wall. Then the characteristic rule is used:

> Write down the exact nonlinear differential relation for the C_+ characteristics. Substitute the expressions for the state variables and the velocity in terms of the shock Mach number. The resulting differential equation gives the variation of the shock Mach number with distance.*

The formulation is not limited to small amounts of nonuniformity, since large amounts may be accumulated over large distances. However, the formulation does neglect some aspects of the flow behind the shock. The reflected disturbances, which propagate on the C_- characteristics, are also re-reflected as they interact with the nonuniform region that the shock has already passed. The re-reflected waves propagate toward the shock along the C_+ characteristics and overtake the shock. The effect of the interaction of the re-reflected waves and the shock is neglected by the Characteristic Rule. For the case of varying area, the effect of neglecting the re-reflected waves has been analyzed by Chisnell (1957), and found to be quite small.

The problem formulation for the propagation of a plane shock along a perforated duct (Fig. 4) is straightforward, as shown by Szumowski (1971). The mass flow through the perforations is written as a function of the state variables and the velocity in the duct, both written in terms of the shock Mach number. These relations are substituted in the differential relation for the C_+ characteristics, which is then evaluated at the shock front. Integrating the differential expression

---

*Whitham, G. B., Linear and Nonlinear Waves, New York: Wiley-Interscience, 1974, pp. 270-271.

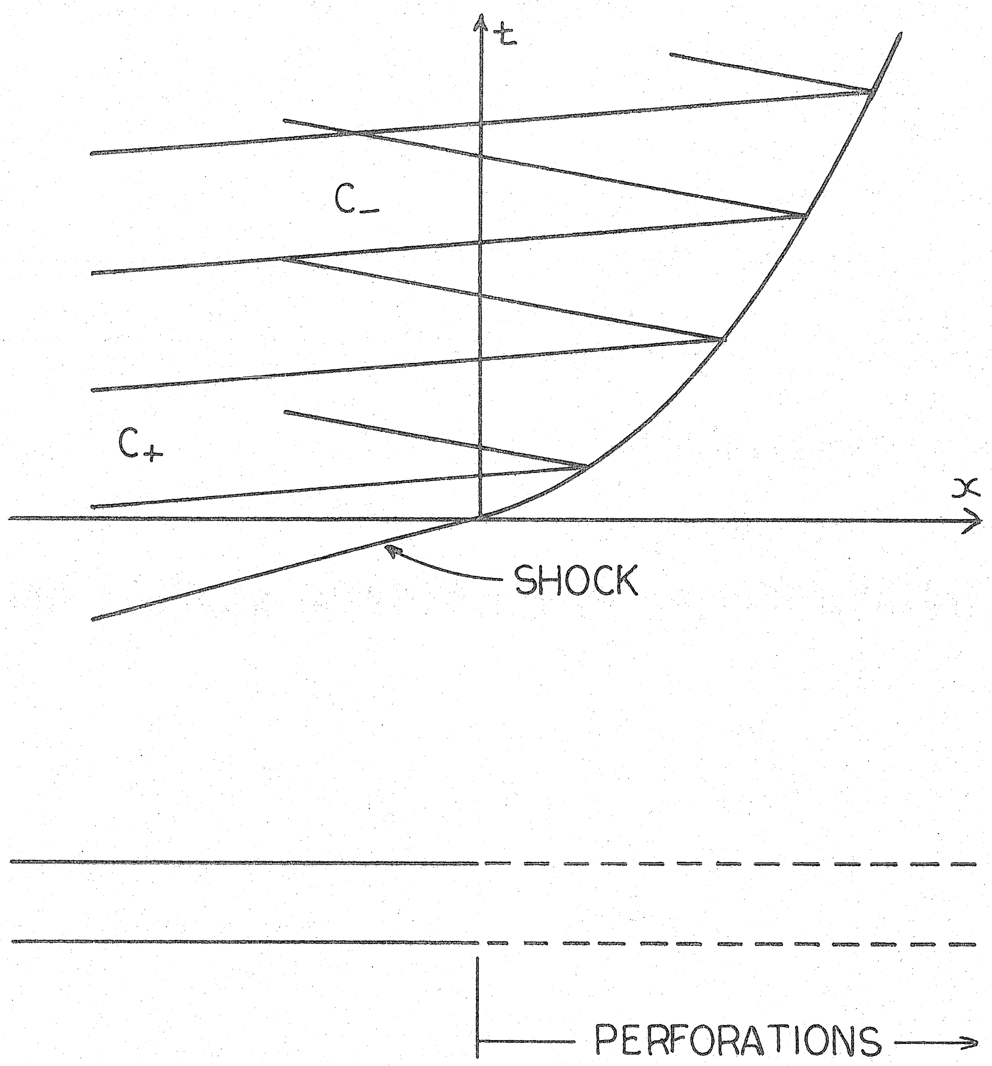

FIG. 4 SHOCK INTERACTION WITH A PERFORATED DUCT

gives the shock strength as a function of the distance along the duct.

Rosciszewski (1959) did the first calculations of the shock attenuation along a uniformly perforated wall. Linearizing the equations for the case of small mass removal, he obtained the differential expression described above. Rosciszewski obtained an expression for the mass flow through the perforate by assuming: (1) that the velocity was given by the static pressure drop across the perforate, (2) that the jet issuing from the perforated duct was normal to the axis of the tube, and (3) that the jet velocity distribution was uniform over the entire cross section of the orifice. Though Rosciszewski did not compare his predictions with values obtained from experiments, Wu and Ostrowski (1971) and Szumowski (1971) published comparisons of Rosciszewski's predictions with experimental data. In both cases the experimental rate of attenuation was much smaller than Rosciszewski had predicted. The discrepancy was caused by the assumptions that the jet through the perforation was normal to the tube axis and occupied the entire cross-sectional area of the perforation. A careful look at the details of such a flow (Stokes et al, 1954) reveals that, in addition to radial momentum, which is due to the pressure drop across the perforations, the fluid in the jets still has the axial momentum that it had inside the tube. Therefore, the jets tilt towards the tube, which reduces their cross-sectional area or the mass flow through the perforations. Wu and Ostrowski (1971) presented a method, based on a compressible hodograph approach developed by Troshin (1959), for calculating the actual mass flow in the jet. The ratio of the actual mass flow to the ideal mass flow is the discharge coefficient.

Szumowski (1971) used a steady flow facility to find an empirical relation between the discharge coefficient and the flow conditions in the duct. Honda (1974) derived a method to find the discharge coefficient by comparing experimental data with a linear theory. The important effect of the discharge coefficient on the shock wave attenuation is also discussed in Section 4.1.

Using spark schlieren photography, Wu and Ostrowski (1971) observed the transient wave interaction occurring at each orifice in a perforated wall. Honda (1974) used a pulsed ruby laser as the light source of a schlieren system to observe the propagation of strong shocks along perforated walls and the supersonic flow established behind the shock. The local flow Mach number in the duct was successfully approximated from the angle of inclination of the Mach wavelets, which propagate into the steady flow from the orifices.

1.1.4 The Open End

To link the internal flows produced by a shock wave in a muffler system to the resultant radiated noise, we have found the reflection of a weak shock from the open end of a tube to be an instructive example. Chester (1949) considered the behavior of the reflected and transmitted waves produced when a step-function sound pulse reaches and progresses beyond the end of a two-dimensional duct. Chester identified the n-th order diffracted fronts (the order is the number of diffraction processes a wave has experienced), which are cylindrical about the ends of the duct, and computed their asymptotic behavior. In addition, Levine and Schwinger (1948) considered the radiated sound from an unflanged circular pipe. For sinusoidal air motions in the pipe, they calculated the end correction to the length of the pipe, the reflection coefficient of the open end, and the axisymmetric sound radiation.

For an axisymmetric (or circular) duct, the first order diffracted fronts form circular toroids about the circumference of the end of the tube (a cross section is shown in figure 5). Only first order fronts will be discussed here. The portion of the diffraction front inside of the tube reflects in such a way that at large distances from the exit it forms a significant portion of the reflected expansion. The portion of the diffracted front outside of the tube is no longer toroidal for $t > R/a$ and begins to look axisymmetric about the axis of the tube for $t \gg R/a$. The width of the pulse is maximum at 90° to the tube axis and becomes very small on the axis. Quantitative features of this interaction are discussed in Section 3.5.

1.2 The Experiment

This work has two basic objectives: (1) the measurement and prediction of the internal and external disturbances produced when muffler elements are subjected to step-function excitation, and (2) the demonstration that ideal shock tube behavior may be modified or used directly to predict real muffler performance. The muffler performance is investigated in two different facilities, a standard one-shot shock tube and a repetitive shock tube.

1.2.1 Experimental Facilities

The one-shot shock tube provides well-defined test conditions in which muffler properties can be investigated quantitatively. In actual engine excitation each successive exhaust pulse generates a nonsteady fluid motion which propagates through the exhaust system. In many

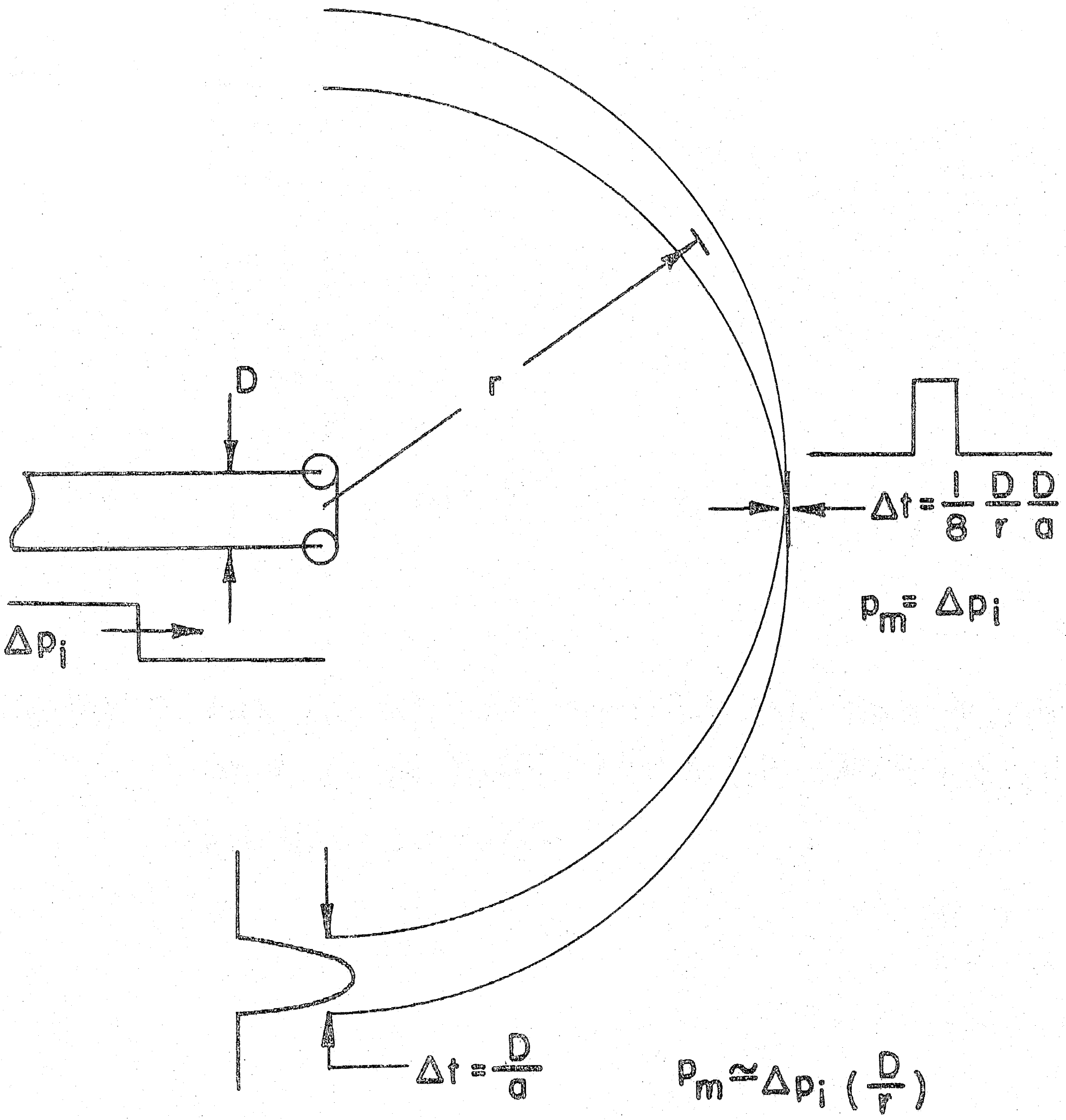

FIGURE 5 THE SOUND PRODUCED BY THE REFLECTION OF A WEAK SHOCK FROM THE OPEN END OF A CIRCULAR DUCT

applications the nonsteady motions have decayed sufficiently that uniform conditions exist ahead of the next exhaust pulse. In this case, the modeling of the actual exhaust system excitation with a single pulse from a shock tube is well justified.

The repetitive excitation facility is a resonance tube. Repetitive excitation provides two additional features not provided by one-shot excitation. The performance of muffler elements may be studied when (1) the excitation is periodic, and (2) the fluid motions have not decayed ahead of each successive exhaust pulse propagating through the exhaust system. Single and repetitive step-function excitation, in some sense, span the range of actual excitations observed in real exhaust systems.

The resonance tube has been an effective tool for studying finite amplitude wave motions (Sturtevant, 1974). The resonance tube, as discussed in Section 2.1.1, is a tube with an oscillating piston at one end. The gas motion excited near resonance in a closed tube has been studied experimentally and theoretically. Lettau (1939) observed the appearance of shock waves in the gas in closed tubes near resonance. Chester (1964) correctly predicted the range of frequencies about the closed end resonance, in which shock waves would occur, and the shock behavior in that range. Jimenez (1973) theoretically and Sturtevant (1974) experimentally investigated the response of partially and completely open tubes to large amplitude excitation near the closed and open end resonance. Sturtevant found that shocks could occur near the closed end resonance even when the passive end is partially open. This observation is utilized in these experiments.

The mufflers are attached to the resonance tube at the passive end; and at the closed end resonance, a sawtooth disturbance is observed. The mufflers are attached to the end of the shock tube in a similar way. The geometries of both facilities are shown in figure 6.

1.2.2 Shock Pulse Excitation

Both of these facilities produce waves which are in some way similar to those observed in high performance exhaust systems. The essential feature of the wave form in these exhaust systems is a steep-front compression followed by a slower expansion to the ambient pressure. The compression is caused by the high velocity gas which discharges from the cylinder through the opening exhaust port. The high exhaust gas velocity quickly decreases as the cylinder pressure drops and the open exhaust port area increases. The deceleration of the gas in the exhaust port causes expansion waves to follow closely behind the initial compression wave.

The wave form observed in the resonance tube possesses the essential features of actual exhaust pulses. Figure 7 shows a comparison of the wave form in the exhaust port of a single cylinder, 250 cc, two-cycle engine and the wave form produced by the resonance tube. In this case, a high performance exhaust system is used. The engine was operating under full load at 6000 rpm. The wave form driven into the exhaust system by the resonance tube so closely resembles the wave form of the actual exhaust pulses, that the point of attachment of the exhaust system to the resonance tube is denoted as the "simulated exhaust port". However, there is one quantitative difference between the simulated and engine-driven exhaust pulses; the rate of decay of the engine-driven pulse is faster than the decay in the simulated pulse.

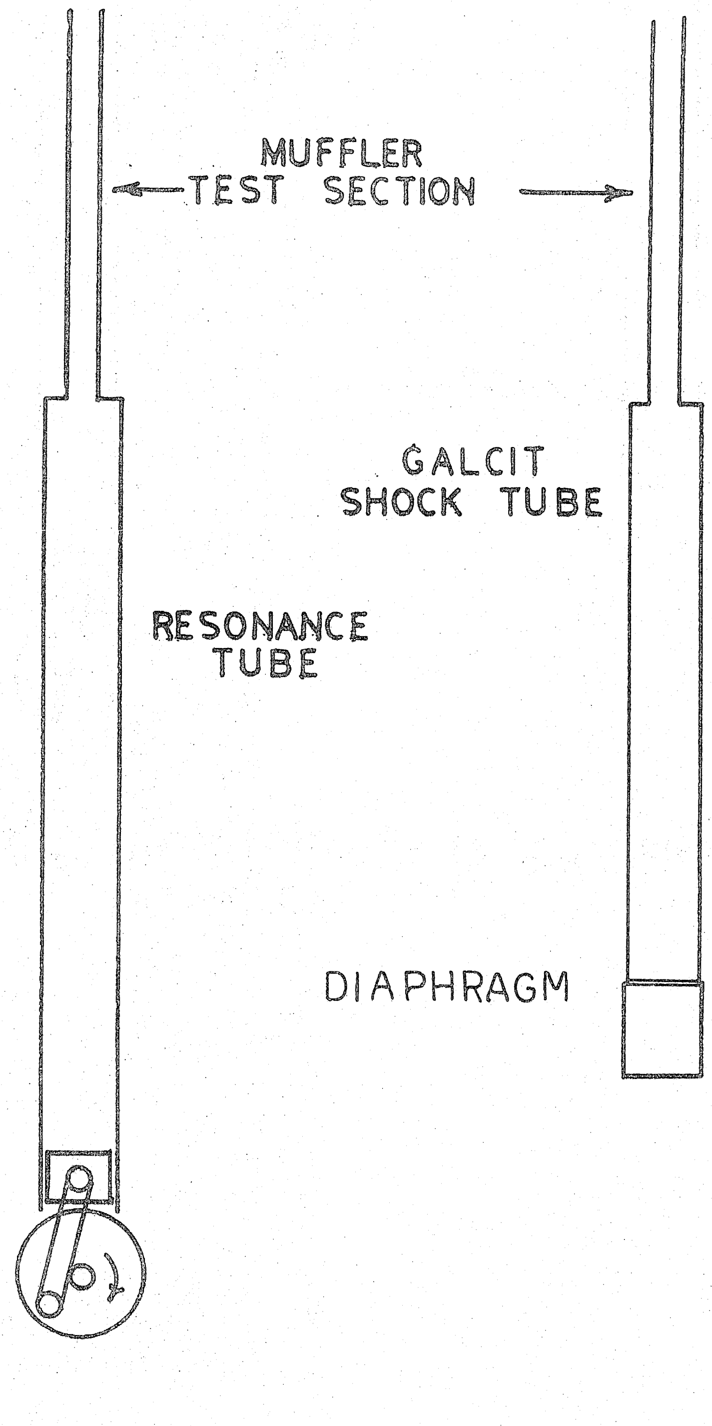

FIGURE 6 THE GEOMETRY OF EXPERIMENTAL FACILITIES

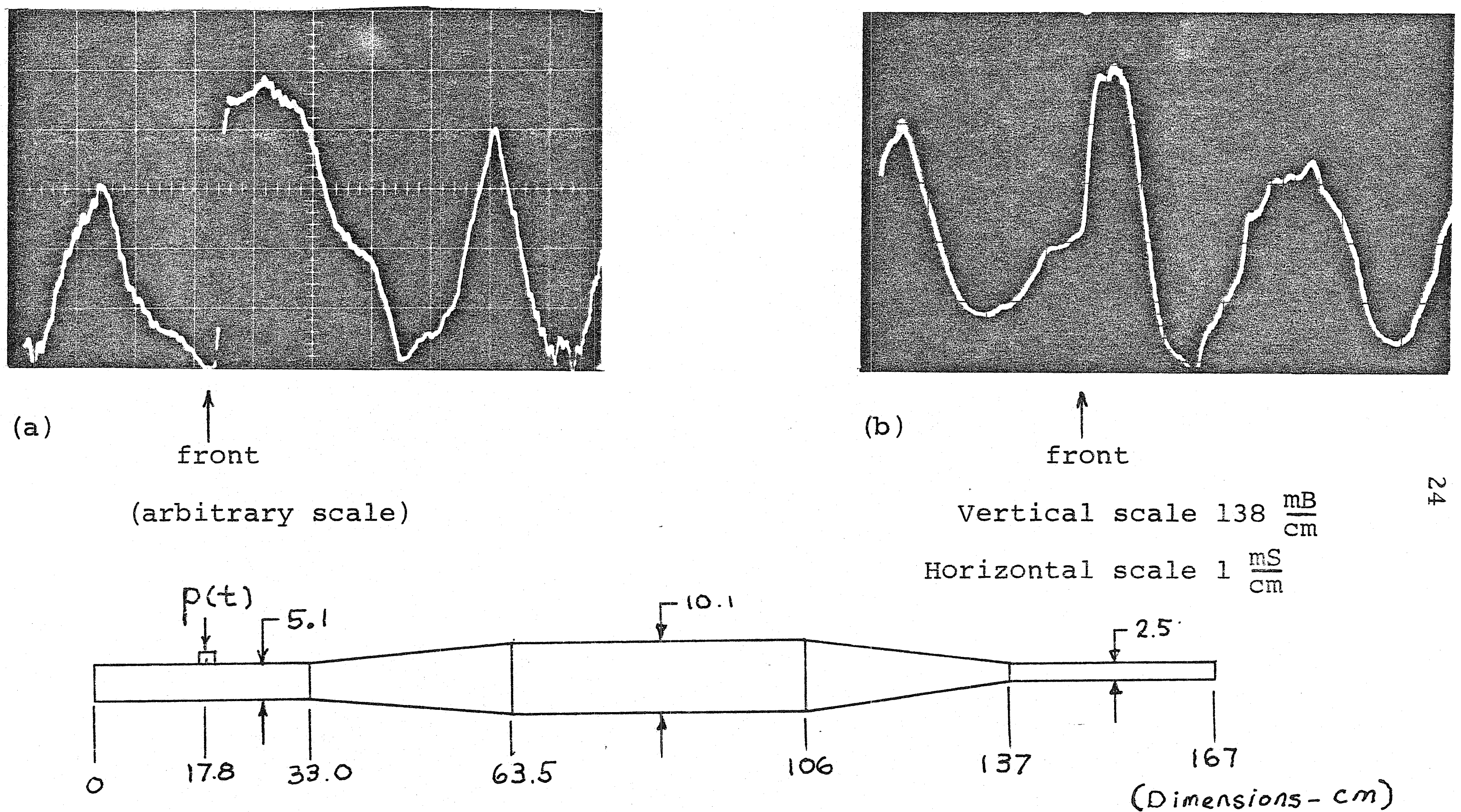
(a)

front

(arbitrary scale)

(b)

front

Vertical scale 138 $\frac{\text{mB}}{\text{cm}}$

Horizontal scale 1 $\frac{\text{mS}}{\text{cm}}$

FIGURE 7 COMPARISON OF RESONANCE TUBE, A, AND MOTORCYCLE ENGINE, B, PRESSURE WAVE FORMS

This difference may be attributed to the relatively large volume of the resonance tube compared to the volume of the engine cylinder.

1.2.3 Acoustical Analyses of Test Mufflers

The muffler systems used in these experiments are sketched in figure 8. They are composed of elements which were described earlier and shown in figure 1. Probably the most common and basic muffler is the expansion chamber. The muffler is formed by terminating the ends of the main chamber with discontinuous area changes to the inlet and outlet pipes. A simple modification is the partial extension of the inlet or outlet pipes into the chamber, which often results in improved performance. Perforated tubes or tubes with orifices in the wall are used by enclosing the perforated section of the tube in a chamber.

These mufflers have been investigated for the case where the excitation has infinitesimal amplitude and sinusoidal form using acoustic theory. Probably the most comprehensive and complete treatment of acoustical muffler design was produced by Davis (1954), though many other examples exist.

Conventional acoustical analysis is usually developed in the frequency domain, and results are also presented in that way. Experimentally, the muffler is excited with a plane sinusoidal wave, and many times an anechoic termination is used in the tailpipe. Plane reflected and transmitted waves, whose amplitudes and phases are computed using the conservation of mass and momentum equations in their linearized form, are assumed at the muffler elements. The attenuation is the difference in the average sound power in the

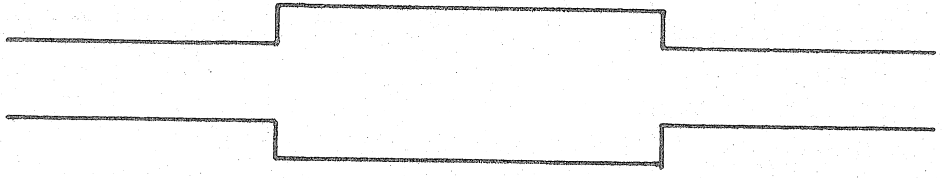

EXPANSION CHAMBER

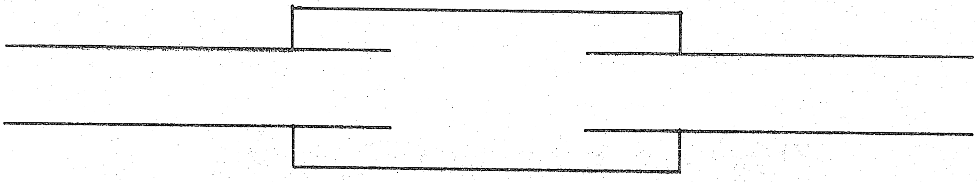

WITH EXTENSIONS

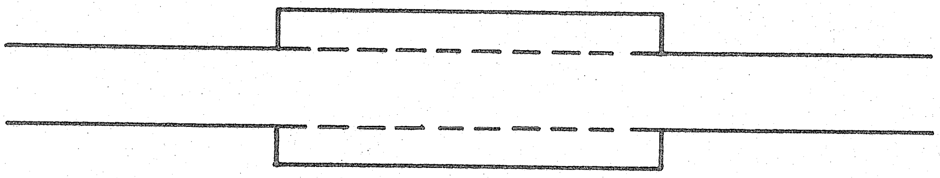

ENCLOSED PERFORATIONS

FIGURE 8 MUFFLER SYSTEMS

incident and transmitted waves. The plane wave assumption becomes invalid when the wave length of the disturbance is of the same order as a cross-sectional dimension of the muffler. Thus, the attenuation is known only over a range of frequencies. A portion of this paper is simply a reinterpretation of well-known effects in acoustics, which are usually expressed and observed in the frequency domain.

In this work the theory is constructed in the X-T plane and pressure measurements are made in the time domain. The unit step-function replaces the sinusoidal excitation used in conventional acoustical analysis. A reflected and transmitted wave is created when the incident wave arrives at a muffler element. The assumption is made that eventually the reflected and transmitted waves will become plane at a large distance from the junction, even though the waves are three-dimensional near the junction (Section 1.1). Thus the interaction of a shock wave with a muffler element is computed by using the one-dimensional nonsteady weak wave relations across the incident, reflected, and transmitted waves and the steady conservation equation across the junction. The attenuation is simply the ratio of the magnitudes of the incident and transmitted waves.

II. EXPERIMENT

2.1 The Experimental Facilities

2.1.1 The Resonance Tube

The resonance tube was designed to study finite amplitude wave phenomena (Sturtevant, 1974). The resonance tube is shown in figure 9; important dimensions are internal diameter, 76 mm; wall thickness, 6.4 mm; and length, 3.9 m. The piston mechanism is taken from a J. A. Prestwick, four cycle, single cylinder motorcycle engine (80 mm bore and 100 mm stroke). The cylinder head of the motorcycle engine has been removed and the resonance tube is mounted in its place. The original hemispherical piston has been replaced by a flat-top piston. The crankshaft of the motorcycle engine has been connected to a 15 HP variable speed (0-100 Hz) DC electric motor. The entire mechanical system, electric motor, piston mechanism, and resonance tube is frame mounted to a one-ton concrete bed, which is dynamically isolated from the laboratory floor by air springs.

For these experiments, the resonance tube is used as a source of repetitive shock waves. The shock waves are driven through the simulated exhaust port and into the muffler systems. In these experiments, the diameter of the inlet pipe is 3.81 cm. The motion in the resonance tube is affected by the reflective and dissipative properties of the muffler system, which causes the incident shock strength to vary from Mach number 1.11 to 1.16.

2.1.2 GALCIT Six-Inch Shock Tube

The GALCIT six-inch shock tube (Smith, 1967) was used for the single pulse experiments discussed in this paper. Though designed

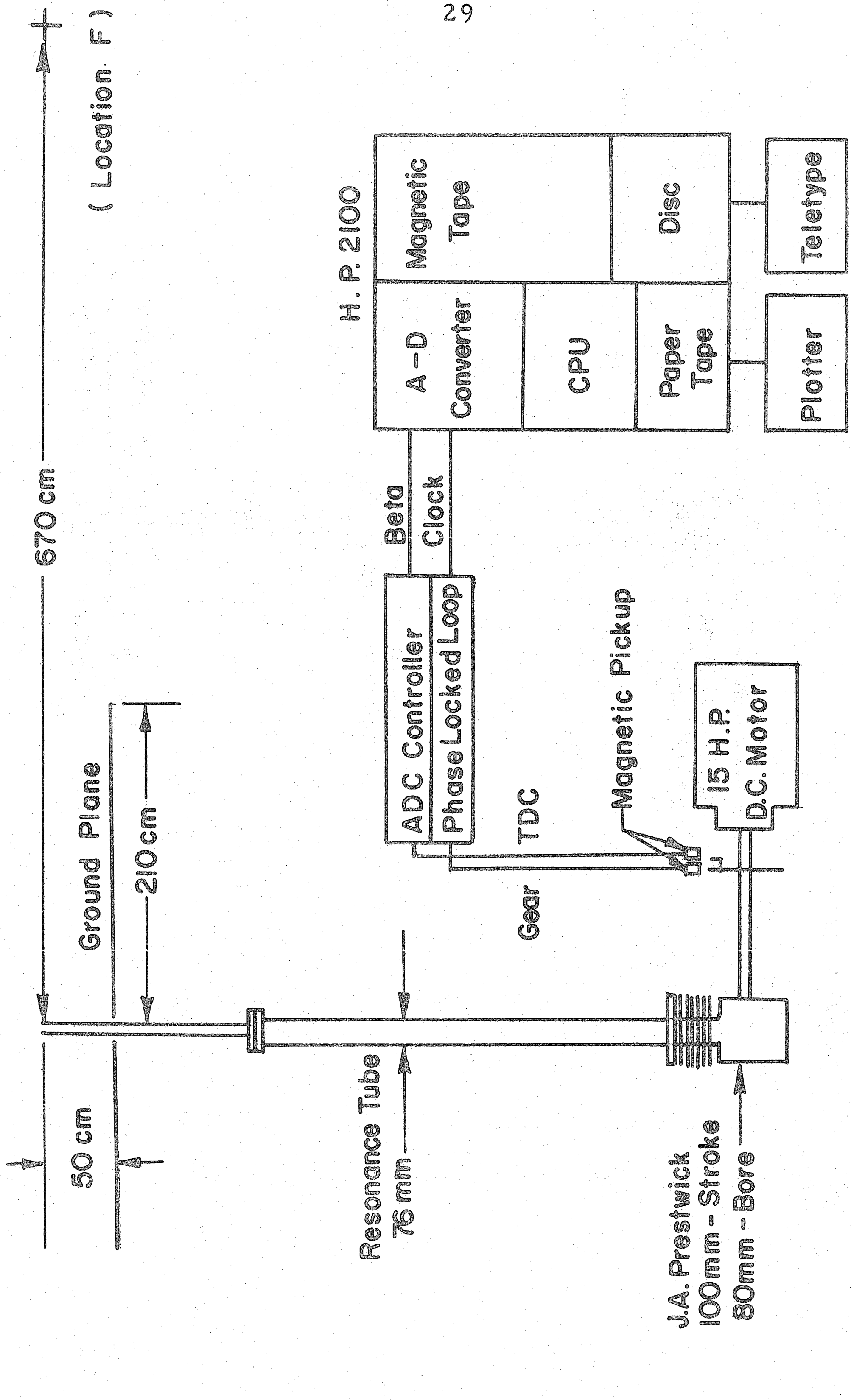
670 cm
(Location F)
50 cm
Ground Plane
210 cm
Resonance Tube
76 mm
J.A. Prestwick
100mm - Stroke
80mm - Bore
Gear
TDC
Magnetic Pickup
15 H.P.
D.C. Motor
ADC Controller
Phase Locked Loop
Beta
Clock
H. P. 2100
A - D
Converter
CPU
Paper
Tape
Magnetic
Tape
Disc
Teletype
Plotter

FIGURE 9

for the production of strong shock waves, it was found that the shock tube performed quite well in generating the much weaker shocks desired for this study ($M_s < 1.6$). The basic shock tube dimensions are driver section length, 1.83 m, and diameter, 16.5 cm; and test section length, 11 m, and diameter, 15.2 cm, as shown in figure 10. The entire tube is type 321 stainless steel with wall thickness 1.27 cm and honed inner surface. The diaphragm, held by a hydraulic clamp system, is cut by a set of crossed knife blades as the driver gas pressure increases.

The shock tube is a facility for conducting experiments under well-defined conditions. It should be noted that since the muffler test section is open to the room, the initial conditions are the ambient atmospheric conditions. The inlet pipe used in the single pulse experiments is 3.81 cm, permitting the use of the same muffler system in both single and repetitive pulse experiments.

The test shock enters the test section when the shock in the main tube reaches the origin (Fig. 10). At this point, the test shock is amplified and passed into the test section where the interaction with muffler systems is studied. In the test section, the incident shock Mach number can be varied from 1.11 to 1.55, which corresponds to a pressure increase of 0.27 to 1.74 Bar. The diaphragms, 1/4 mil mylar, 3, 6, 10, and 20 mil 1100 aluminum alloy, provided five test Mach numbers with nitrogen gas in the driver section and room air in the test section. Also a cookie cutter (1.64 meters long) was employed, reducing the test shock Mach number to 1.07 with a test time of 9 msec. It was found that to obtain reproducible test shocks at low

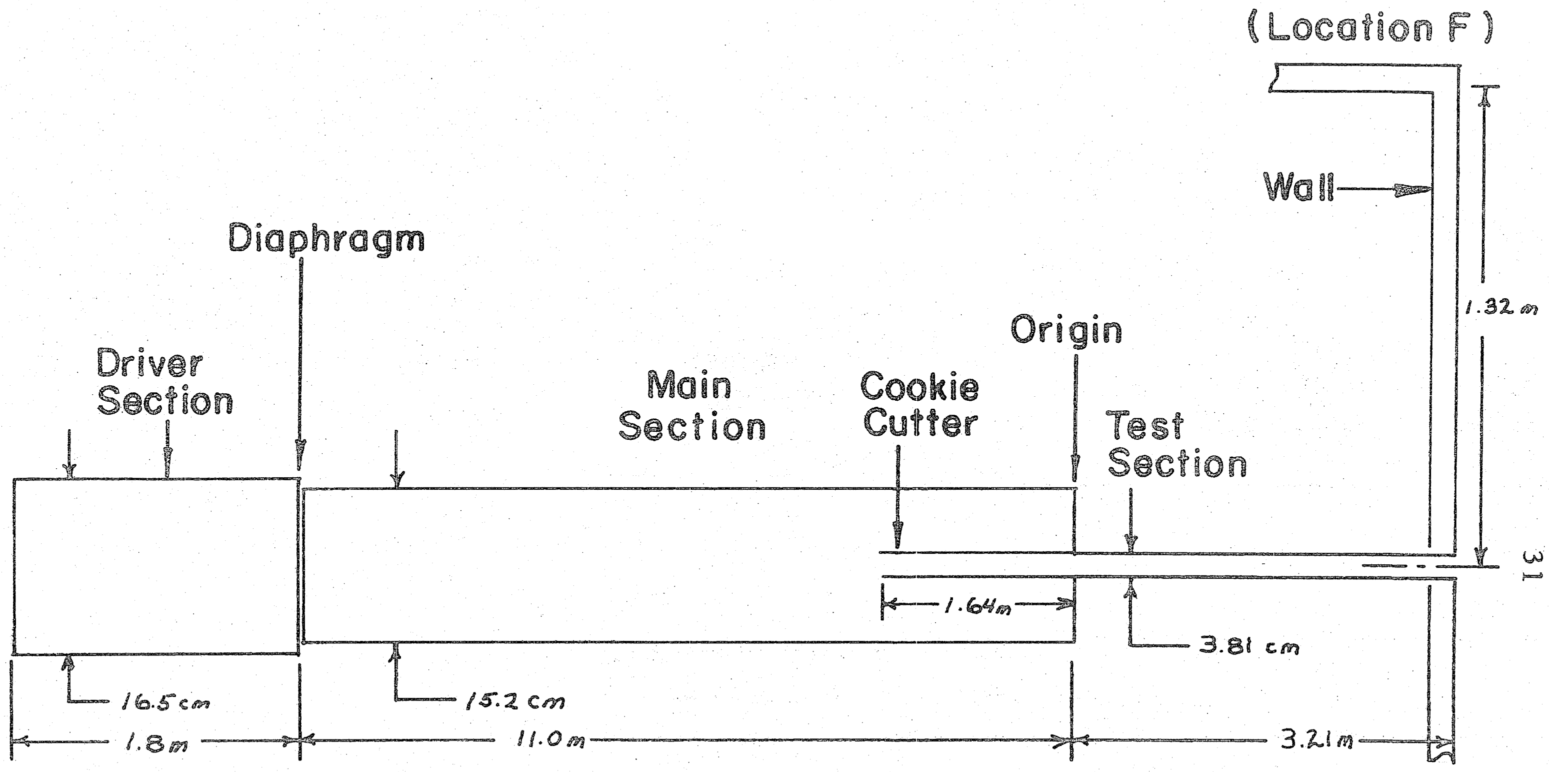

FIGURE 10 GALCIT SIX INCH SHOCK TUBE

Mach number, the knife blades had to be kept extremely sharp. Neglecting to periodically sharpen the blades resulted in nonreproducible diaphragm performance.

2.2 Muffler Description and Instrument Location

The muffler systems used in both the single and repetitive pulse experiments are attached to the inlet pipe as shown in figure 6. With a constant area pipe (1.52 m length) attached to the test section origin, the test shock strength is constant in the muffler test section (Fig. 6). This is shown in figure 11 for the single pulse and repetitive pulse experiments.

The perforated tube has been constructed from a section of 2024 seamless aluminum tubing (38.1 mm diameter and 1.59 mm wall thickness, Fig. 12). The orifices, which are 6.35 mm diameter drilled holes, are located such that the porosity, the open area in the wall per unit wall area, is approximately 1/6. The perforated tube is "thin walled"; that is, the wall thickness is small compared to the orifice diameter. A total of 144 holes were drilled. The number of open holes in a given experiment was selected by taping portions of the tube with air conditioning duct tape.

The expansion chambers were constructed from 2024 alloy aluminum. Three expansion chamber diameters were used with area ratios 2.77, 4.69, and 9.00. These three expansion chambers will be denoted as expansion chamber A, B, and C, respectively (Fig. 13).

Internal pressure histories have been recorded at locations shown in figures 12 and 13, and external pressure histories have been recorded at locations shown in figures 9 and 10. Internal measurements

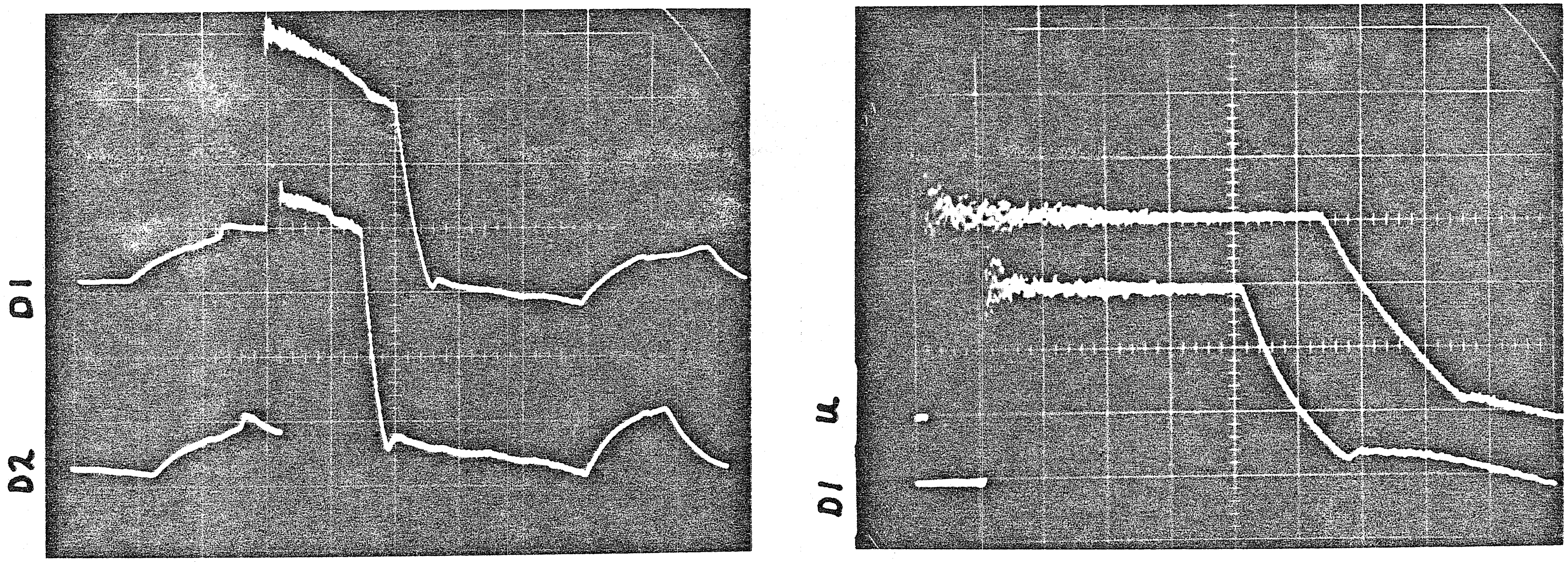

A

B

	A			B		
BEAM	SENSITIVITY	VERTICAL	HORIZONTAL	SENSITIVITY	VERTICAL	HORIZONTAL
upper	$68.9\ \frac{mB}{V}$	$2\ \frac{V}{cm}$	$2\ \frac{mS}{cm}$	$68.9\ \frac{mB}{V}$	$2\ \frac{V}{cm}$	$2\ \frac{mS}{cm}$
lower	$2.27\ \frac{mB}{V}$	$50\ \frac{MV}{cm}$	$2\ \frac{mS}{cm}$	$68.9\ \frac{mB}{V}$	$2\ \frac{V}{cm}$	$2\ \frac{mS}{cm}$

FIGURE 11 PRESSURE TRACES: RESONANCE TUBE, LOCATIONS D1 AND D2;
(B) SHOCK TUBE, LOCATIONS U AND D1

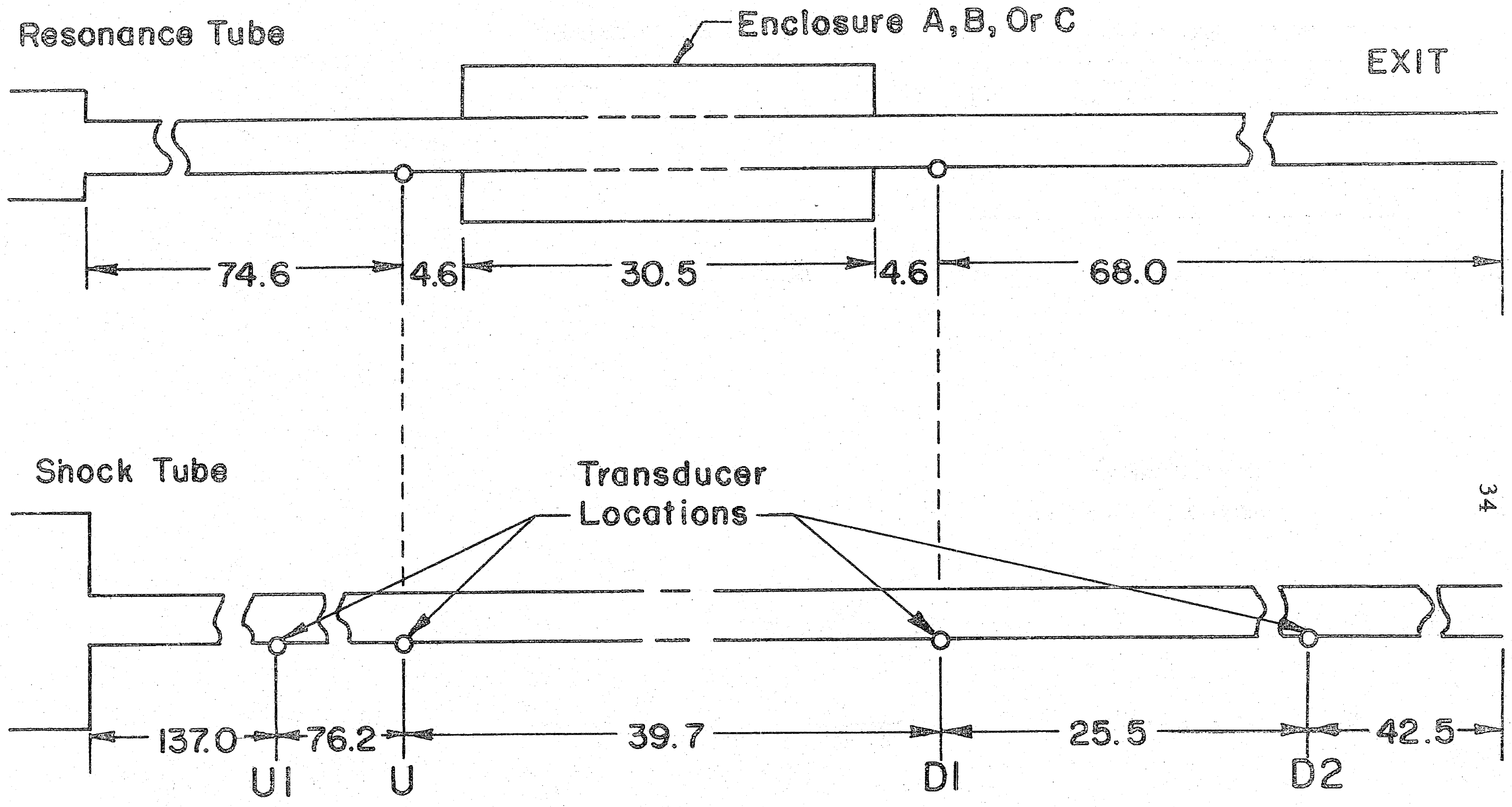

All Dimensions Cm.

FIGURE 12 PERFORATION SYSTEMS

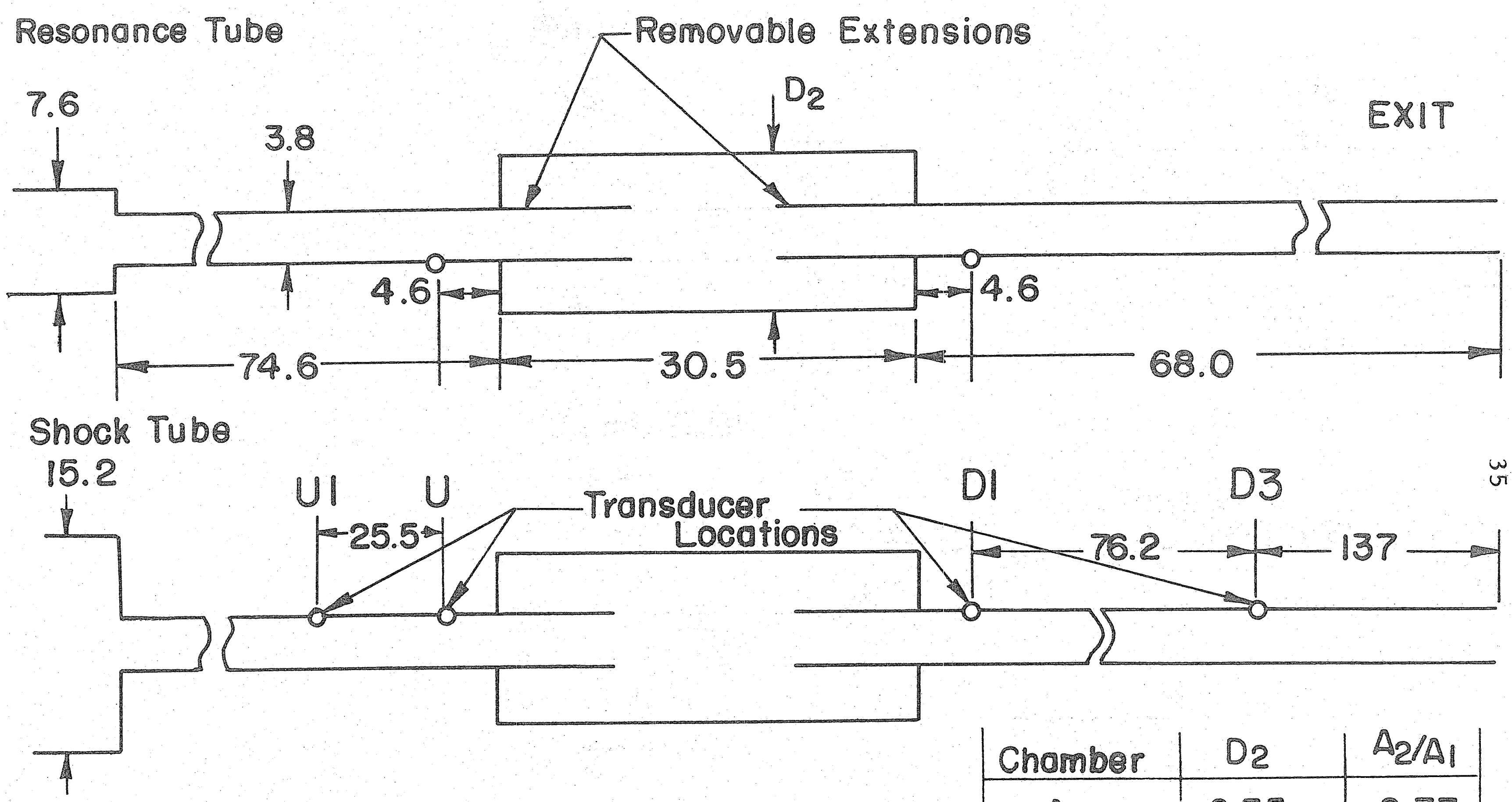

Dimensions In Cm.

Chamber	D_2	A_2/A_1
A	6.35	2.77
B	8.25	4.69
C	11.4	9.00

FIGURE 13 EXPANSION CHAMBER SYSTEMS

were made with flush-mounted pressure transducers, and external measurements were made with microphones oriented normal to the direction of propagation.

2.3 Data Acquisition and Handling

2.3.1 Repetitive Pulse Excitation

The experiments involving the resonance tube used a data acquisition system built around a Hewlett-Packard 2100 minicomputer, known locally as the Solo System. The data are recorded and processed in real time by the Solo System. Programs written in Fortran IV language are used to control both acquisition and data processing.

Solo is comprised of a central processor unit, CPU, and the peripheral devices shown in figure 9. The CPU has a 32K work storage capacity and does computational operations using a 16-bit word in cycle times of less than 1 μsec.

Solo is a disc-operating system. Most user and system programs are disc-resident programs and are loaded into core by system or user commands. The teletype gives the user rapid access to disc-resident programs. The disc also serves as a rapid-access storage device which vastly increases the effective storage capacity of Solo.

The Preston GM Series analog to digital converter, ADC, performs conversions at up to 500 kHz from up to 16 channels of analog voltage data. The resolution is 14 bits or 0.61 mv over a range of ±10 volts. In these experiments, the ADC is programmed to perform one conversion for every CLOCK pulse on the condition that BETA is high. This feature of the ADC, with the use of sufficient interfacing, provides a convenient means to synchronize the data acquisition rate to the frequency of the resonance tube.

Two basic operations were required of the interfacing. Both interface devices use input signals from magnetic pickups mounted on the crank mechanism of the resonance tube. The input signals are known as TDC and GEAR and have a frequency of 1 and 256 times the crank frequency.

The ADC controller uses the TDC signal and generates a digital signal BETA. The TDC signal nominally occurs at top-dead center of the piston motion (actually 10° before top-dead center). BETA is normally low, but goes high at the beginning of the run coincidentally with the TDC pulse after the run button is pushed. BETA stays high for four cycles, after which it returns to the low state. BETA, an input to the ADC, enables or disables the possibility of data conversion.

The phase-locked loop, PLL, uses the GEAR signal as input and generates a synchronous digital signal, CLOCK. During one cycle of the TDC signal, 256 cycles of the GEAR signal occur. The frequency of the GEAR signal is the fundamental CLOCK frequency. The PLL is used as a frequency multiplier. The frequency of the synchronous output from the PLL, CLOCK, is eight times that of the GEAR frequency. Thus, 2048 cycles of the CLOCK signal occur in each cycle of the TDC signal. CLOCK, an input to the ADC, causes data conversions when BETA has enabled the ADC. The timing of the interfacing circuits is shown schematically in figure 14, and the wiring diagrams are in figures 15 and 16.

14

INTERFACING TIMING DIAGRAM

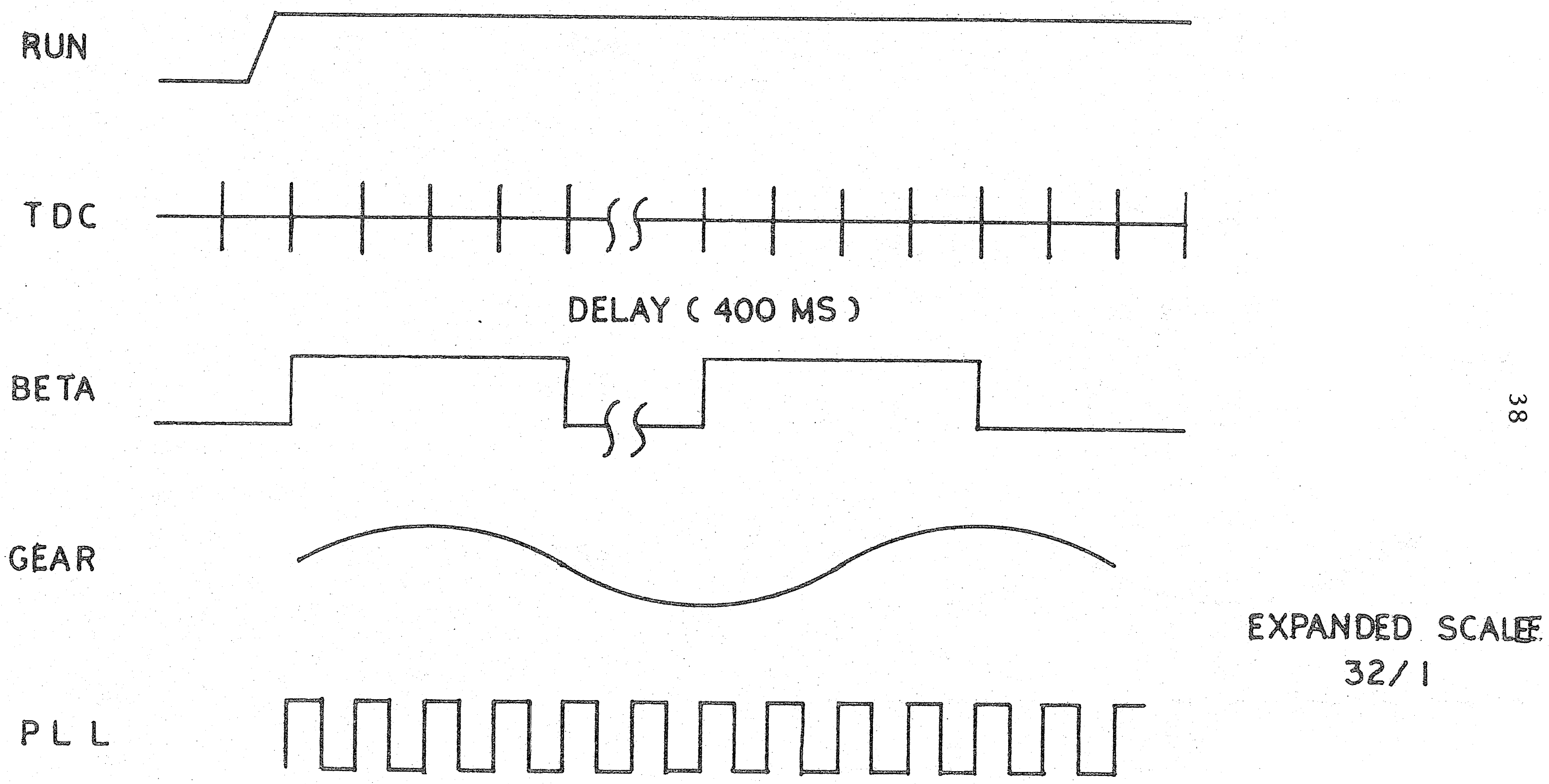

FIGURE 14

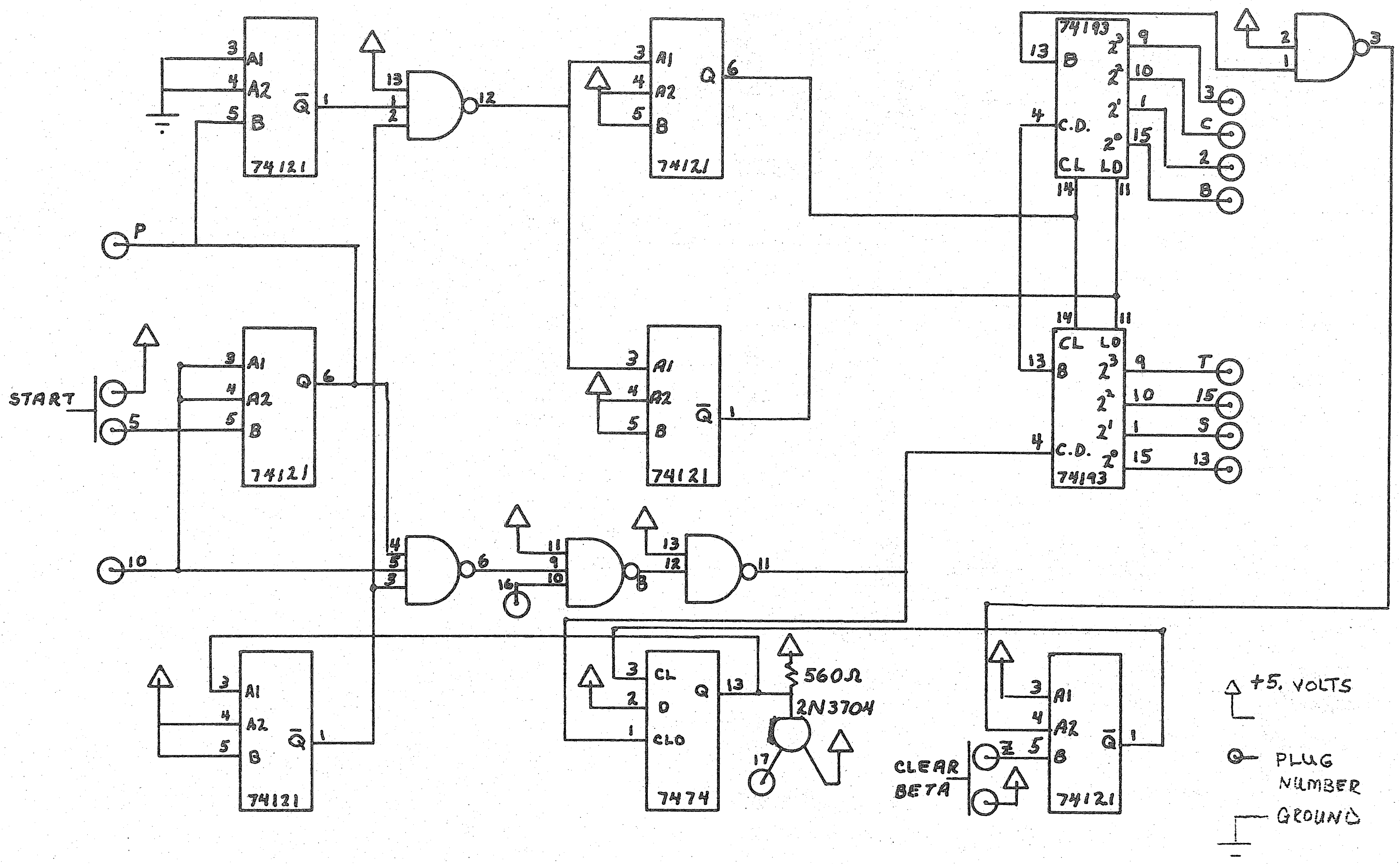

FIGURE 15 ADC CONTROLLER

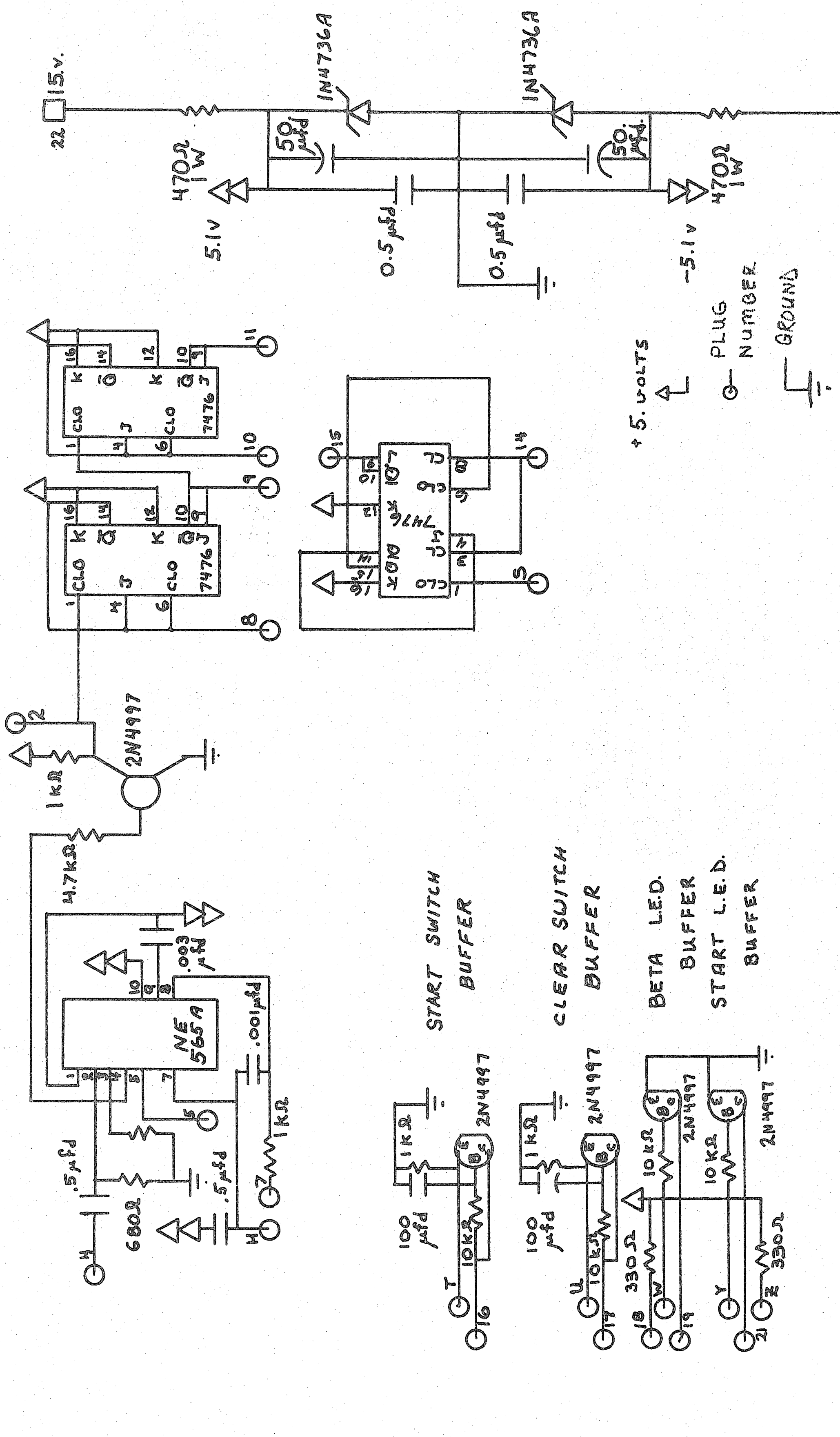

FIGURE 16 PHASE LOCK LOOP

The ADC is programmed in the multiplex mode, where two channels are recorded. In the multiplex mode, each clock pulse digitizes one channel and advances the ADC to the next channel so that the data are recorded alternately from the two channels. The data are acquired at the CLOCK rate, ensuring 2048 points in each cycle. The period of the data acquisition is four cycles; each record contains 8192 points. Two records are recorded in each experiment. The first record is transferred from core to disc during the delay; then the second record is taken and transferred to the disc. After the data are stored on the disc, each record is transferred to the core where its data are sorted to form two new records. The four smaller records, two for each channel, are stored on the disc. Thus, each final sorted record represents data taken over a period of four cycles at a rate of 1024 points per cycle. The length of each record is typically 4 cycles/ 40 Hz = 100 Ms and the data rate is typically 1024 x 40 Hz = 40 kHz.

The data acquisition and processing programs are shown schematically in figure 17. Permanent records from the data acquisition program are plots of average wave forms, raw data written on magnetic tape, and a listing of run identification parameters from the teletype. The first data processing program produces a raw wave form plot of each cycle in the record, from which wave amplitude data are obtained, as shown in figure 18. The second data processing program uses a fast Fourier transform, FFT, routine to calculate the spectrum of the raw data. Acoustic intensity spectra, $(p^2/\rho a)$ in db re 1 μwatt, are plotted logarithmically against frequency for permanent record. The plotted spectrum is the average of the two records taken

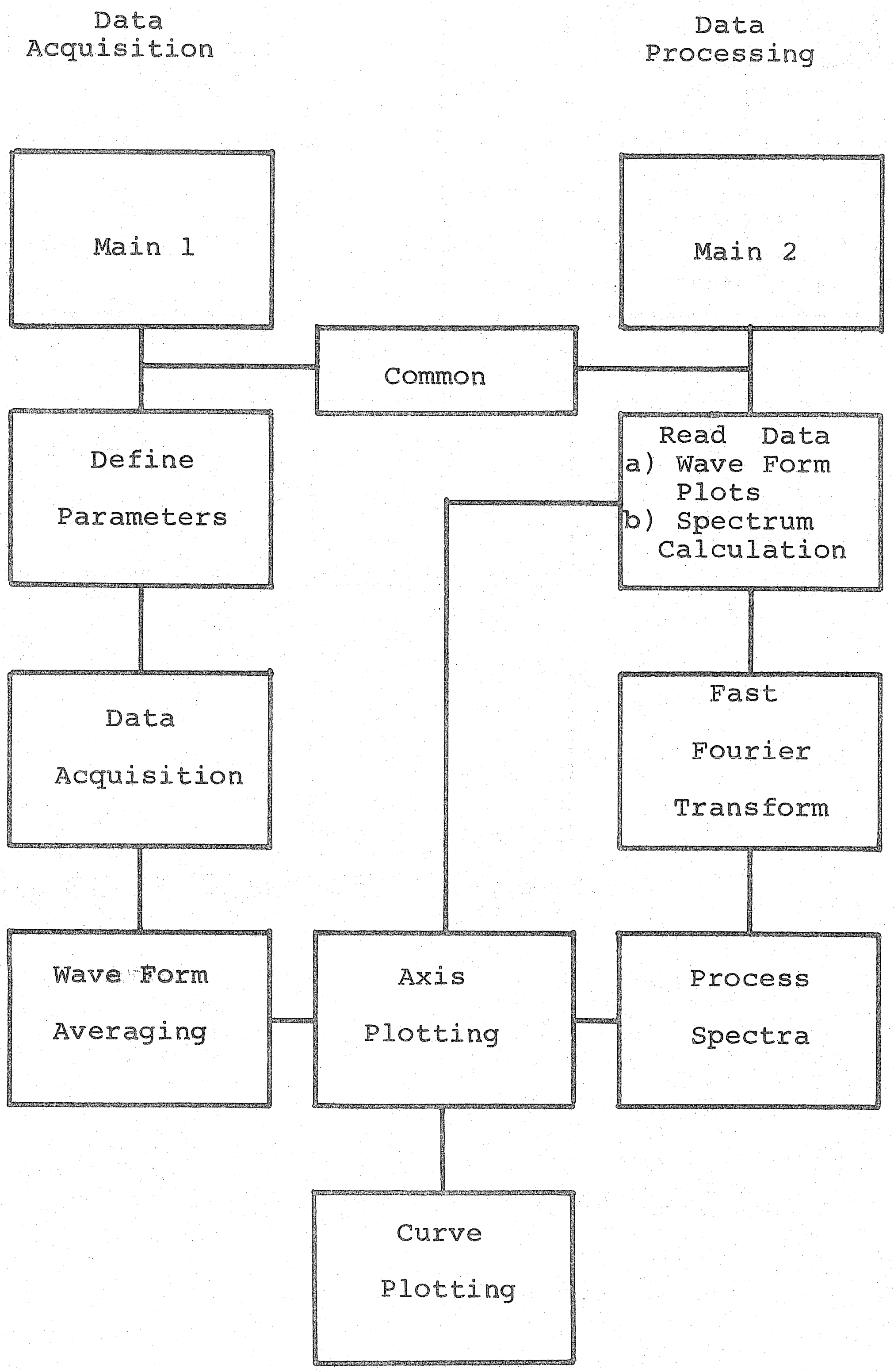

FIGURE 17 COMPUTER PROGRAMS

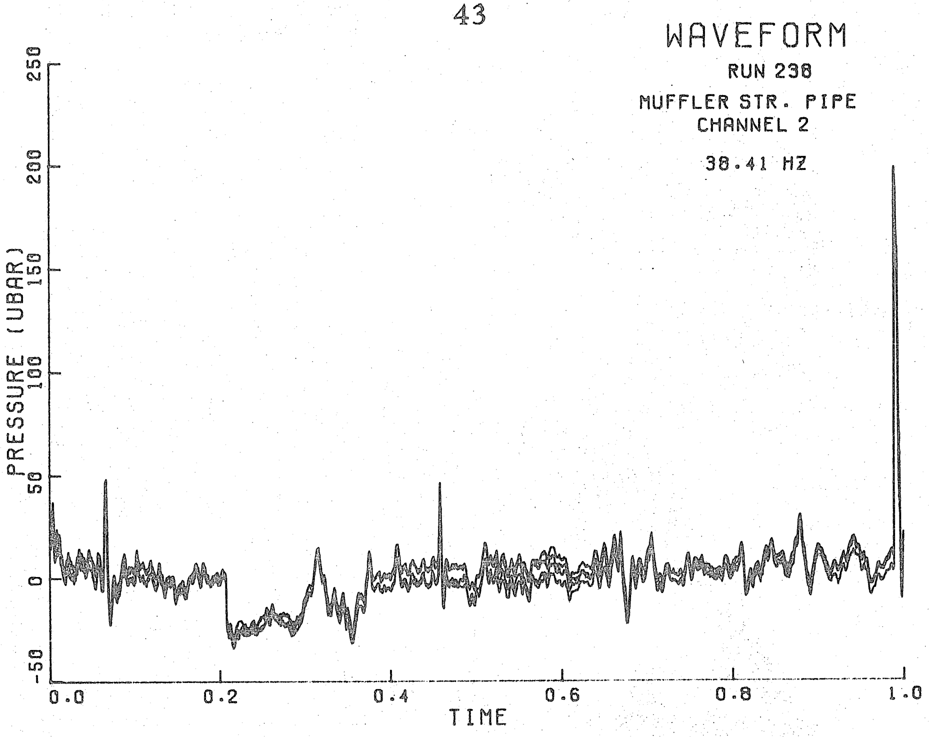

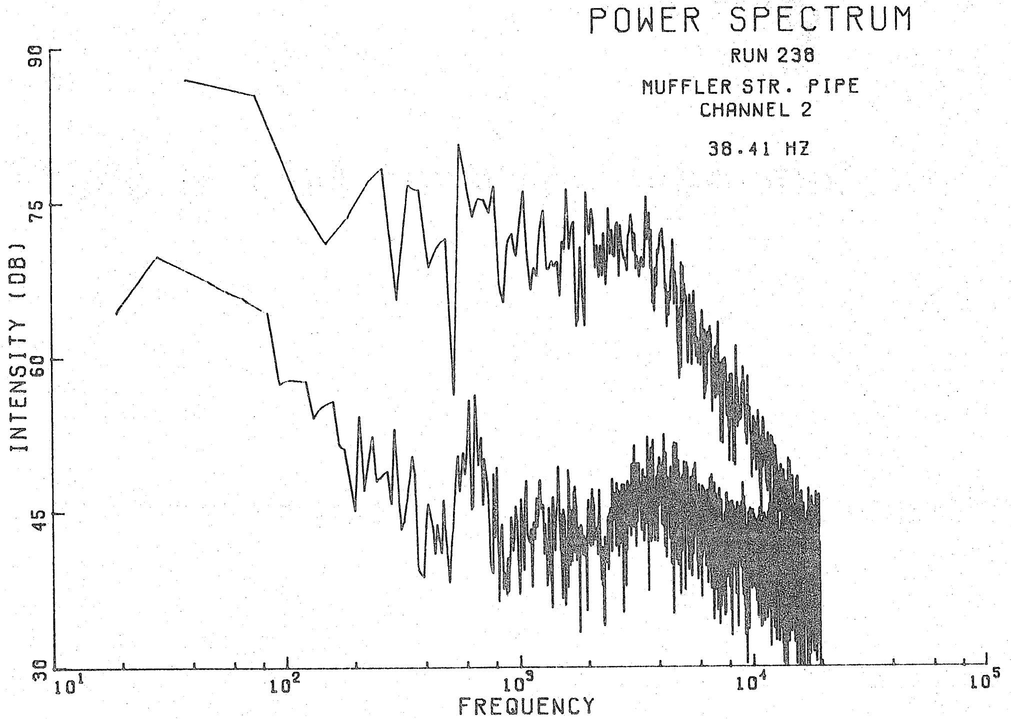

FIGURE 18 WAVE FORM AND SPECTRUM

in the experiment. A final program segment calculates the sound pressure level of the spectrum in unweighted or A-weighted decibels.

2.3.1.1 Periodic Signals and the FFT

When the FFT alogrithm is applied to a data set obtained by sampling a periodic signal at a frequency synchronous with the periodic signal, the components of FFT are the Fourier series coefficients of the periodic signal. However, whereas the theoretical Fourier series contains an infinite number of coefficients, the FFT generates a finite number of components. The manner in which the Fourier series coefficients above the Nyquist frequency (1/2 the sampling frequency) combine with the coefficients below the Nyquist frequency to form FFT components, is called aliasing.

It is useful to express the data set, used in the FFT calculation, as the product of three functions:

$p(t)$ - the periodic signal, whose fundamental frequency is ω_f,

$\text{Rect}\,(-\frac{x}{2}, \frac{x}{2})$ - Rectangle function of the sampling period, which is an integer multiple of the fundamental period, $x = \frac{2\pi}{\omega_o}$, and $\omega_f = M\omega_o$,

$\sum_{J=-\infty}^{\infty} \delta(t - J\frac{x}{N})$ - Dirac comb function of the sampling rate, $\omega_s = \frac{2\pi N}{x} = N\omega_o$.

The Fourier transform of their product, divided by the sampling period, is

$$P_f(\omega) = \int_{-\infty}^{\infty} \frac{p(t)}{x} \, \text{Rect}\left(-\frac{x}{2}, \frac{x}{2}\right) \sum_{J=-\infty}^{\infty} \delta\left(t - \frac{J}{N}x\right) e^{-i\omega t} \, dt \qquad (1)$$

The convolution theorem gives

$$P_f(\omega) = \frac{1}{2\pi X} \int_{-\infty}^{\infty} \sum_{k=-\infty}^{\infty} a_k\, \delta(\nu - k\omega_f) \cdot \sum_{J=-\infty}^{\infty} R(\nu - \omega - J\omega_s)\, d\nu \qquad (2)$$

where the integrand is the product of two Fourier transforms:

(1) F.T. $(\text{Rect}\,(-\frac{x}{2}, \frac{x}{2}) \cdot \quad \delta(t - J\frac{x}{N}))$, which by the convolution theorem equals, $\frac{1}{2\pi} \int_{-\infty}^{\infty} \sum_{J=-\infty}^{\infty} \delta(f - J\omega_s) R(\omega - f)\, df$

or $\frac{1}{2\pi} \sum_{J=-\infty}^{\infty} R(\omega - J\omega_s)$, and

(2) F.T. $(p(t)) = 2\pi \sum_{k=-\infty}^{\infty} a_k\, \delta(\nu - k\omega_f)$, (Papoulis, 1962),

where the a_k are the coefficients of the Fourier series of $p(t)$.

Interchanging the orders of integration and summation and then integrating gives

$$P_f(\omega) = \frac{1}{2\pi X} \sum_{J=-\infty}^{\infty} \sum_{k=-\infty}^{\infty} a_k\, R(k\omega_f - \omega - J\omega_s) \qquad (3)$$

but since $\omega_s = N\omega_o$ and $\omega_f = M\omega_o$

$$P_f(\omega) = \frac{1}{2\pi X} \sum_{J=-\infty}^{\infty} \sum_{k=-\infty}^{\infty} a_k\, R\left(\left(kM - \frac{\omega}{\omega_o} - JN\right)\omega_o\right) \qquad (4)$$

The discrete version of this continuous function is

$$P_f(I\omega_o) = \frac{1}{2\pi X} \sum_{J=-\infty}^{\infty} \sum_{k=-\infty}^{\infty} a_k\, R((kM - I - JN)\,\omega_o) \qquad (5)$$

where the index, I, is the number of the Fourier component.

The Fourier transform of the Rectangle function, $\text{Rect}\,(-\frac{x}{2}, \frac{x}{2})$, is denoted $R(\omega)$, or

$$R(\omega) = \text{F.T.}\left(\text{Rect}\left(\frac{-x}{2}, \frac{x}{2}\right)\right) = \frac{2\sin\left(\frac{\omega x}{2}\right)}{\omega} \qquad (6)$$

Since x equals $\frac{2\pi}{\omega_o}$, equation 6 can be written

$$R(\omega) = \frac{2 \sin \frac{\omega}{\omega_o}\pi}{\omega} \tag{7}$$

The discrete version of equation 7 is

$$R(L\omega_o) = \frac{2 \sin L\pi}{L\omega_o} = \begin{cases} \frac{2\pi}{\omega_o} & , \quad L = 0 \\ 0 & , \quad L \neq 0 \end{cases} \tag{8}$$

and, therefore, in equation 5 $R((kM - I - JN)\omega_o)$ is only non-zero when k equals $\frac{I + JN}{M}$. Equation 5 is reduced by observing that $R((kM - I - JN)\omega_o$) is non-zero only when $k = \frac{I + JN}{M}$,

$$P_f(I\omega_o) = \frac{1}{2\pi} \sum_{J=-\infty}^{\infty} a_{\left(\frac{I+JN}{M}\right)} = \frac{2}{2\pi} \sum_{J=0}^{\infty} a_{\left(\frac{I+JN}{M}\right)} \tag{9}$$

or

$$P_f\left(\frac{I}{M}\omega_f\right) = \frac{2}{2\pi} \sum_{J=0}^{\infty} a_{\left(\frac{I+JN}{M}\right)} \tag{10}$$

The spectral components of the FFT occur at two distinct types of frequencies: (1) harmonics of the periodic signal, and (2) between harmonics (aharmonics); in fact, at harmonics they are equal to a sum of the Fourier series coefficients, and at aharmonics they are zero. Since harmonic components of the FFT are not merely Fourier series coefficients, but an infinite sum of them, there is aliasing, which causes high frequency spectrum to contribute to low frequency spectrum. As a result of sampling data for M cycles of the periodic signal, there are (M - 1) aharmonic components of the FFT spectrum between each harmonic component. Further, the aharmonic spectrum have zero amplitude.

In particular, for our case, M was 4 and N was 4096, and substitution into equation 10 gives

$$P_f(k\omega_f) = \frac{2}{2\pi}\sum_{J=0}^{\infty} a_{(k+J\frac{N}{M})} \tag{11}$$

where k is equal to I/M. For example, the case of k equals one gives

$$P_f(1\omega_f) = \frac{2}{2\pi}\left(a_1 + a_{1+1024} + a_{1+2048}\cdots\right) \tag{12}$$

The component of the FFT at the fundamental frequency of the periodic signal, ω_f, has an error of order a_{1025}/a_1. This is a "small" problem if the signal has very little power above the sampling frequency, and therefore can usually be "improved" by either increasing the sampling frequency or filtering the data before it is recorded. It should be emphasized that these are only improvements, and that exactness cannot be obtained in physical systems.

For these experiments the sampling frequency was 40 kHz. The spectral content of the pressure signals at the Nyquist frequency, 20 kHz, was generally about 50 db down from the overall RMS level. Hence, it is felt that the sampling rate was sufficiently rapid to avoid significant problems from aliasing.

Some checks have been made to estimate the accuracy of the FFT. The most straightforward method is to compute the spectrum of a known function (in our case, we used a cosine function). The computed amplitude of the spectrum at the fundamental frequency was only one part in 10,000 different from the input amplitude. The amplitudes of all the other harmonics were at least four orders of magnitude lower than the amplitude of the fundamental. For these experiments, a second check is made. The RMS pressure level can be computed not only from the raw data, but also from the spectra. In practice this comparison is probably more useful or realistic. Typically, the RMS values from the raw data are within 0.5% of RMS values computed from the spectra.

In summary, since the data are sampled "exactly" synchronously with the periodic motions, and the data records are an integer number of cycles in length, it is not necessary to apply window functions to the FFT. Because of the synchronization, certain of the Fourier coefficients are harmonics of the periodic motion; since there are four cycles in each record, every fourth point in the spectrum is the amplitude of a harmonic of the periodic motion. The three points between each harmonic are aharmonics, and they are regarded as components of the continuous or background spectrum unrelated to the harmonic components of the periodic motion. The continuous components could be caused by: imperfect synchronization (e.g., by backlash in mechanical drive), electronic noise in the instrumentation, round off error in the FFT, ambient acoustic disturbances, or aperiodic aerodynamic noise. The harmonic and continuous components of the spectrum are plotted separately in figure 18. The plots are a spectral indication of the signal to noise ratio.

2.3.2 Single-Pulse Excitation

Experiments were performed in the shock tube specifically to make accurate measurements of the transmission and reflection coefficients of various muffler elements. The pressure data were observed on a Model 565 Tektronix 2-channel dual-beam oscilloscope and recorded on polaroid film for the experiments in which the radiated pressure history was not recorded. Data processing is done using a computer program written in Fortran IV language and run on Solo (Appendix B). The program calculates conditions in regions 1 through 4 and the exit. It uses input wave-amplitude data to calculate static and stagnation conditions in regions 2 through 4, mass flow in regions 3 and 4, and the discharge coefficient.

Detailed time-series data is required to compute the radiated SPL. Hence, the Solo system was used to acquire and digitize the data for the experiments in which the radiated pressure histories were required. The ADC was programmed to begin converting when a sensor upstream of the test section indicated the arrival of the shock. At this time a 4500 word record was taken from the three internal pressure transducers at the maximum clock rate, 400 kHz, or 133 kHz per channel. A second record, 3600 or 2400 words from the transducer measuring external radiated noise , is taken in the signal channel mode at 400 kHz. For the case of perforations, 6 msec was sufficient; but for expansion chambers, 9 msec was required to wait for the radiated noise to decay. The second record begins almost immediately (one msec) after completion of the first record.

The pressure histories are plotted and processed after the shock tube is fired. The incident shock strength and radiated SPL are computed. The sound level is taken as the root mean square pressure level during the time in which the data was recorded

$$SPL = \frac{1}{T}\int_0^T p^2(t)\,dt = \frac{1}{N}\sum_{i=1}^{N} p^2(t_i)$$

Since atmospheric conditions existed in the test section before each run, the values of the temperature and pressure in the laboratory were measured and used in data-processing programs.

2.4 Transducer Calibration

Model 606A Kistler and Model 113A21 PCB pressure transducers were calibrated from 0.3 to 1.6 Bar. The calibration was done in the GALCIT six-inch shock tube, using standard shock tube methods. The transducers were flush mounted in the side wall of the shock tube, 50 cm apart. The time interval between the shock arrival at each transducer was measured on a 0.1 μsec Hewlett-Packard Timer-Counter-DVM. The shock Mach number is computed using the shock speed and the initial conditions in the test gas. The measured pressure change across the shock is compared with the value computed from the shock Mach number. For Mach numbers near one, the measured pressure change on the PCB transducer was used in place of the value obtained from timing measurements. The pressure signals are recorded on oscillograms.

The calibration data are presented in figure 19. The calibration error is computed as the standard deviation of the data and is listed in figure 19 with the sensitivity and background noise level. The Kistler transducer's signals were filtered with a 20 kHz low pass filter, giving a rise time of 25 μsec. The PCB signals were not filtered, giving a rise time of 2 μsec.

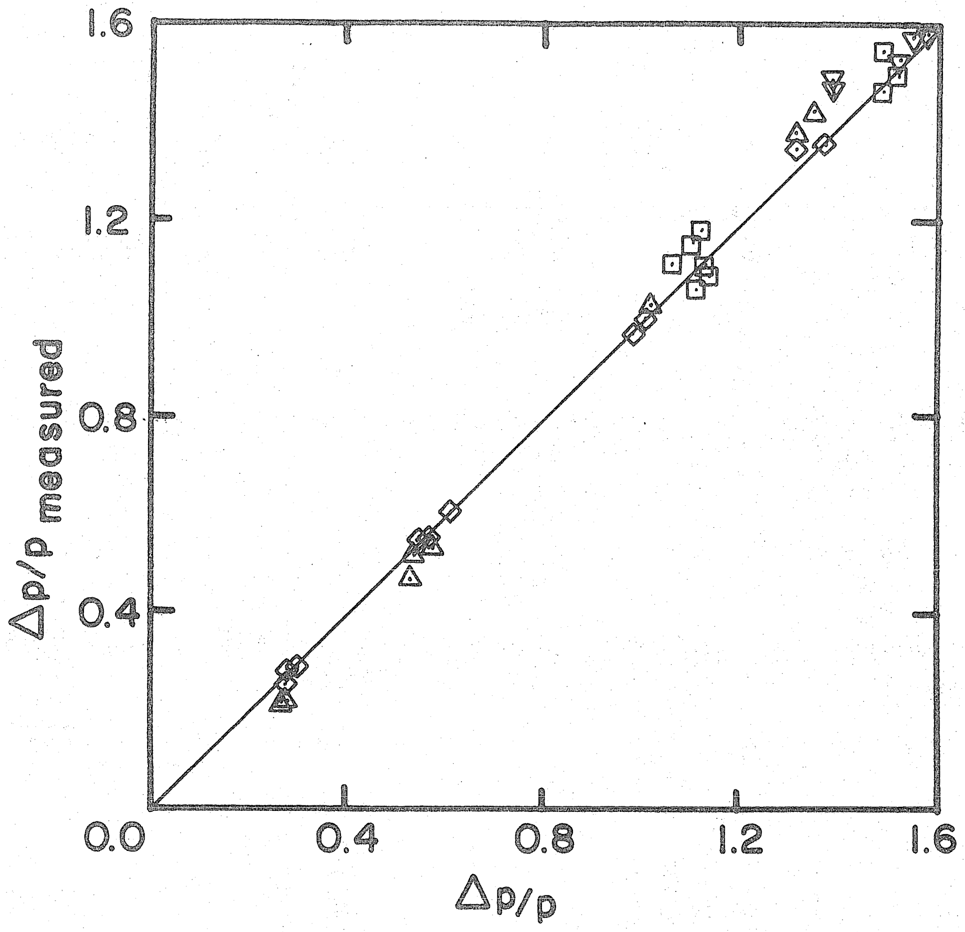

SYMBOL	VERTICAL ($\Delta P/P$)	HORIZONTAL ($\Delta P/P$)
▽	2459	113A21
△	2459	M_s
◇	2307	113A21
⊡	2307	M_s

TRANSDUCER (#)	SENSITIVITY (mV/Bar)	ERROR (%)	RANGE (Bar)	NOISE LEVEL (μBar)
113A21	454.	–	0.0–1.6	200.
	CHARGE (pCb/psi)			(mV)
2459	3.21	4.6	0.0–0.4	40.
	3.78		0.4–1.0	
	4.06		1.0–1.6	
2307	4.53	3.2	0.0–1.6	40.

FIGURE 19 TRANSDUCER CALIBRATION

III. ANALYSIS

3.1 Introduction

The interaction of a weak shock wave with a muffler element is analyzed by assuming that reflected and transmitted waves are plane at a sufficient distance from the element. The one-dimensional nonsteady equations for weak waves are expanded in terms of the Mach number or pressure perturbation. The one-dimensional steady equations are expanded in terms of the Mach number. Solutions are obtained for the acoustic parameters, the reflection and transmission coefficients for the geometries discussed in section 1.1. The solutions represent the asymptotic value of the wave strengths (i.e., at a large distance from the element).

The solution for the discontinuous change in area geometry is found from the equations written to second order. At first order the solution is linear, dependent only on the area ratio. The second order terms cause the solution to depend on the area ratio and the incident shock amplitude.

The solution for the perforated tube is unique, as the smallest perforation looks as if it were an open end (the reflection and transmission coefficients are minus one and zero, respectively), when the incident shock strength is infinitesimal. Thus, perforations are extremely good at attenuating low-amplitude shocks. By including only the largest second order term, it may be seen that accounting for the jet Mach number at the perforations causes the solution to depend on the area ratio and the incident shock amplitude in a nonlinear manner. The solution of the equations complete to second order is obtained numerically.

At second-order the nonsteady wave relation is

$$\pm \Delta M = \frac{\Delta p}{\gamma p} - \left(\frac{\gamma+1}{4}\right)\left(\frac{\Delta p}{\gamma p}\right)^2 \qquad (1)$$

or

$$\pm \frac{\Delta p}{\gamma p} = \Delta M + \left(\frac{\gamma+1}{4}\right) \Delta M^2 \qquad (2)$$

M

(P) is the pressure, (M) is the local Mach number, and the plus and minus sign denotes right-going and left-going waves. The relation is valid for compression and expansions, since both processes are isentropic at second order.

3.2 Perforated Tubes

A weak shock traveling in a tube interacts with a section of perforated tube. A wave is reflected and a modified incident shock is transmitted. The reflection and modification results from the mass flow through the perforate.

An X-T diagram of the wave interaction in the tube depicts the trajectories of the incident, reflected, and transmitted waves which form boundaries between the fluid at rest, region 1, and the disturbed regions, 2, 3, and 4, as shown in figure 20. The ratio of the total perforated area, A_e, to the tube cross-sectional area, A, is the perforation area ratio, B.

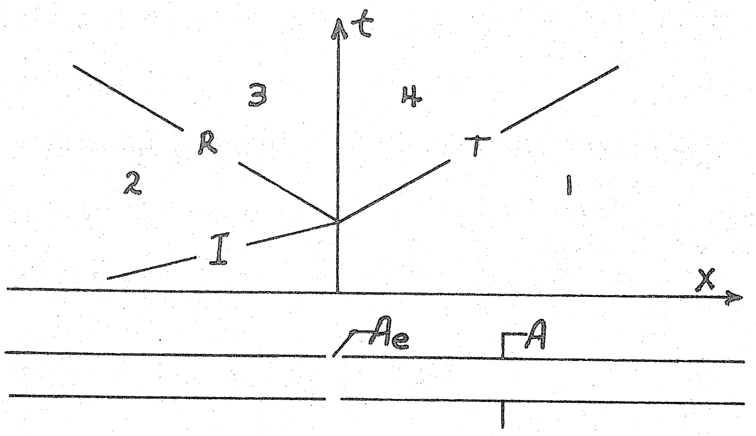

WAVE DIAGRAM FOR PERFORATIONS

Figure 20

The nonsteady isentropic wave relation (Eq. 1) is used to relate the conditions across the incident, reflected, and transmitted waves. The relations governing the flow conditions between regions 3 and 4 and through the perforate are derived from the equations for steady isentropic flow. Continuity of mass requires

$$\rho_e U_e A_e = (\rho_3 U_3 - \rho_4 U_4) A \qquad (3)$$

where the velocity and density are (U) and (ρ) respectively, and the subscript (e) denotes the conditions of the jet of fluid issuing from the perforations. Assuming that the fluid in region 3 expands isentropically through the perforations to the ambient pressure.

$$p_3 \left(1 + \frac{\gamma-1}{2} M_3^2\right)^{\frac{\gamma}{\gamma-1}} = p_1 \left(1 + \frac{\gamma-1}{2} M_e^2\right)^{\frac{\gamma}{\gamma-1}} \qquad (4)$$

where M_e is the jet Mach number of the flow through the perforations. Similarly, the relation between regions 3 and 4 is

$$P_3 \left(1 + \frac{\gamma-1}{2} M_3^2 \right)^{\frac{\gamma}{\gamma-1}} = P_4 \left(1 + \frac{\gamma-1}{2} M_4^2 \right)^{\frac{\gamma}{\gamma-1}} \tag{5}$$

Expanding the steady equations in terms of the Mach number, the pressure and the area ratio, equation 3 becomes,

$$\beta M_e = M_3 - M_4 + O(M^3) \quad , \ \beta = A_e/A \tag{6}$$

and equation 4,

$$\frac{P_3}{P_1} = \frac{1 + \frac{\gamma}{2} M_e^2 + O(M^4)}{1 + \frac{\gamma}{2} M_3^2 + O(M^4)} \tag{7}$$

or

$$\frac{P_3}{P_1} - 1 = \frac{\gamma}{2} (M_e^2 - M_3^2) + O(M^4) \tag{8}$$

and similarly, equation 5,

$$\frac{P_3}{P_4} = \frac{1 + \frac{\gamma}{2} M_4^2 + O(M^4)}{1 + \frac{\gamma}{2} M_3^2 + O(M^4)} \tag{9}$$

or

$$\frac{P_3}{P_4} - 1 = \frac{\gamma}{2} (M_4^2 - M_3^2) + O(M^4) \tag{10}$$

Keeping only up to second order terms, equations 6, 8, and 10

$$\beta M_e = M_3 - M_4 \tag{11}$$

$$\frac{P_3 - P_1}{\gamma P_1} = \frac{1}{2}\left(M_e^2 - M_3^2\right) \tag{12}$$

and

$$\frac{P_3 - P_4}{\gamma P_1} = \frac{1}{2}\left(M_4^2 - M_3^2\right) \tag{13}$$

The exit Mach number can be eliminated from equation 12,

$$\frac{P_3 - P_1}{\gamma P_1} = \frac{1}{2}\left(\left(\frac{M_3 - M_4}{\beta}\right)^2 - M_3^2\right) \tag{14}$$

Using the nonsteady wave relation, equation 1, which gives the change in Mach number in terms of the change in pressure, to relate conditions across the incident, transmitted, and reflected waves, equations 13 and 14 reduce to

$$(c - a - b) - \frac{1}{2}\left((a-b)^2 - c^2\right) + O(a^3) = 0 \tag{15}$$

$$(a+b) + \frac{1}{2}\left((a-b)^2 - \left(\frac{a-b-c}{\beta}\right)^2\right) + O(a^3) = 0 \tag{16}$$

where (a), (b) and (c) are the normalized wave amplitudes, $(P_2 - P_1)/\gamma P_1$, $(P_3 - P_2)/\gamma P_1$, and $(P_4 - P_1)/\gamma P_1$, respectively.

The lowest order solution is obtained by assuming the incident shock amplitude is small (i.e., a, b, and c are all small compared to one). If the second-order terms are dropped in equations 15 and 16, we obtain

$$c - a - b = 0 \tag{17}$$

and

$$a + b = 0 \tag{18}$$

The solution of equations 17 and 18 is

$$T = c/a = 0, \tag{19a}$$

$$R = b/a = -1, \tag{19b}$$

where (R) and (T) are the reflection and transmission coefficients, respectively.

It can be argued that the largest local Mach number always occurs through the perforations. Retaining only the term M_e^2 in equation 12, equations 15 and 16 reduce to

$$c - a - b = 0 \tag{20}$$

and

$$(a+b) - \frac{1}{2\beta^2}(a-b-c)^2 = 0 \tag{21}$$

The solution of these equations is

$$R = T-1 = \frac{K^2}{2} - K\sqrt{1+\frac{K^2}{4}} \tag{22}$$

where

$$K = \sqrt{\frac{\beta^2}{2a}} = \frac{A_e}{A}\sqrt{\frac{\gamma p_1}{2(p_2-p_1)}} \tag{23}$$

This result shows the basic nonlinearity of the shock-wave interaction in a perforated tube. The parameter, K, is not only a function of area ratio but varies inversely with the square root of the amplitude.

There are two simple limiting cases corresponding to large and small values of the parameter, K,:

For large K,

$$\text{Limit}_{k \to \infty} \left(\frac{k^2}{2} - k\sqrt{1 + \frac{k^2}{4}} \right) = -1$$

or

$$R = -1$$
$$T = 0 \quad , \tag{24}$$

which was obtained earlier for small amplitude incident shocks. For small K,

$$\text{Limit}_{k \to 0} \left(\frac{k^2}{2} - k\sqrt{1 + \frac{k^2}{4}} \right) = -k$$

or

$$R = -K$$
$$T = 1 - K. \tag{25}$$

For small values of the parameter the result is linear in the parameter.

The result for large values of the parameter emphasizes the significance of equations 19a and 19b, which show that even a small perforation looks like an open end when the incident shock has infinitesimal amplitude. Now equation 23 shows what combination of area ratio and amplitude is required for the small perforation to act like an open end.

This amazing result exhibits how remarkably well perforations attenuate small-amplitude shocks, and further, how they lose this ability when the amplitude is increased.

In order to truly account for second order effects, the solutions to equations 15 and 16 were obtained numerically. The specific equations used in the numerical computation were;

$$\beta^2\left(\frac{c^2}{2}+c\right)-(a-b-c)^2=0 \tag{26}$$

which is the sum of equations 15 and 16, and equation 16. The procedure for obtaining the numerical solution of these equations is presented in Appendix A. The results are complementary to the analytic solution obtained for low amplitudes. The numerical approximation to the solution is practically equal to the analytic value at low amplitudes, while at increased amplitude, substantial differences are noticed. These two predictions of the performance of perforations are compared with data in section 4. 1.

The complete one-dimensional inviscid steady and nonsteady equations for a perfect gas are utilized to process the data. These equations are presented in Appendix B. The data handling procedure serves as an independent assessment of the validity of the assumptions used in the analysis.

3.3 Discontinuous Area Changes

3.3.1 Individual Elements

The arrival of a shock wave at a change in cross-sectional area produces a system of diffraction waves which eventually coalesce to form the reflected wave and interact with the incident wave to form the transmitted wave. In the analysis, the diffracted waves are not discussed, except indirectly, as they establish the steady flow conditions through the junction which fixes the strength of the reflected and transmitted waves. The analysis assumes that the reflected and transmitted waves have reached their asymptotic strengths and that the fluid motions behind them are uniform.

An X-T diagram, figure 21, shows the waves of interest.

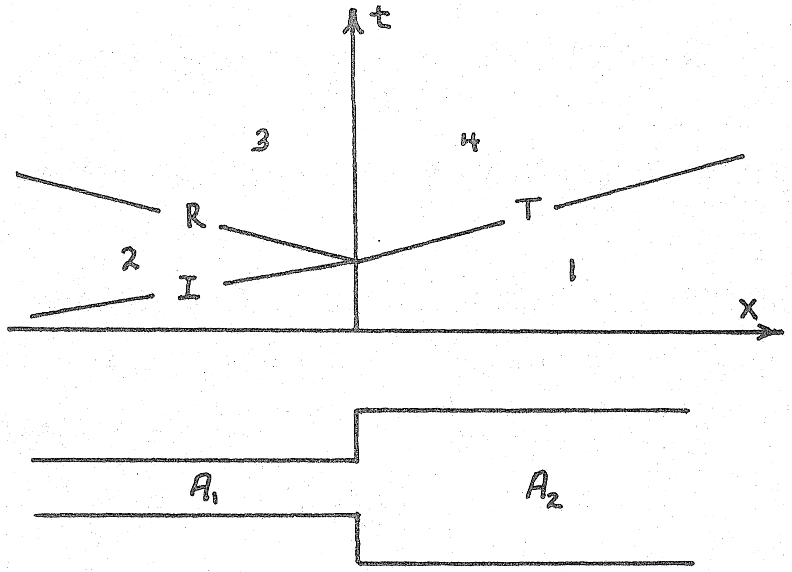

WAVE DIAGRAM FOR AREA EXPANSION
Figure 21

Equation 1 relates the conditions in the four regions indicated on the X-T diagram.

The relations governing the flow conditions between regions 3 and 4 are derived from steady isentropic equations. Continuity of mass requires:

$$\rho_3 u_3 A_1 = \rho_4 u_4 A_2 \tag{27}$$

or in terms of the Mach numbers and area ratio ($\beta = A_2/A_1$),

$$M_3 = \beta M_4 + O(M^3) \tag{28}$$

The pressures and Mach numbers in regions 3 and 4 obey the relation derived in section 3.2, equation 13. Rewriting equation 28,

$$(M_3 - M_2) + M_2 = \beta M_4 \tag{29}$$

and using equation 1, one can derive the following relation,

$$(a - b - \beta c) + \frac{\gamma+1}{4}(-a^2 + b^2 + \beta c^2) = 0 \tag{30}$$

where (a), (b), and (c) were defined in section 3.2.

Substitution of equation 28 into equation 13 gives

$$\frac{P_3 - P_4}{\gamma P_1} = \frac{1}{2} M_4^2 (\beta^2 - 1) \tag{31}$$

which by using equation 1 can be written

$$(c - a - b) + \frac{1}{2}(1 - \beta^2)\left(c - \frac{\gamma+1}{4} c^2\right)^2 = 0 \tag{32}$$

Retention of second order terms in equation 32 gives

$$(c - a - b) + \frac{1}{2}(1 - \beta^2) c^2 = 0 \tag{33}$$

In terms of the acoustic parameters, equations 30 and 33 become

$$(1 - R - \beta T) - \frac{\gamma+1}{4} a (1 - R^2 - \beta T^2) = 0 \tag{34}$$

and

$$(T - 1 - R) + \frac{1}{2} a (1 - \beta^2) T^2 = 0 \tag{35}$$

The small amplitude solution is obtained by setting (a) equal to zero,

$$R = \frac{1 - \beta}{1 + \beta} \tag{36a}$$

$$T = \frac{2}{1+\beta} \tag{36b}$$

The small-amplitude solution is denoted, (T_o) and (R_o), and substituted into the second order terms in equations 34 and 35 to obtain the next order solution.

$$R = R_0 \left(1 + a\beta T_0 \right) \tag{37a}$$

$$T = T_0 \left(1 - a R_0 \right) \tag{37b}$$

The sensitivity to amplitude is readily shown by observing,

$$\frac{\partial R}{\partial a} = \beta R_0 T_0 \tag{38a}$$

$$\frac{\partial T}{\partial a} = -R_0 T_0 \tag{38b}$$

Figure 22 is a table showing the direction of the change in magnitude of the acoustic parameters when the incident shock amplitude increases. The small-amplitude solution is compared with experiments in section 4.2.

	$\beta = 0$	$0 < \beta < 1$ CONTRACTION	$1 < \beta < \infty$ EXPANSION	$\beta \to \infty$
$\lvert T \rvert$	CONSTANT $T = 2$	DECREASE	INCREASE	CONSTANT $T = 0$
$\lvert R \rvert$	CONSTANT $R = 1$	INCREASE	INCREASE	CONSTANT $R = -1$

Figure 22 AMPLITUDE DEPENDENCE

3.3.2 The Expansion Chamber

The standard expansion chamber muffler consists of an area expansion followed by an area contraction, as shown in figure 23. The incident shock is weakened at the upstream junction ($T = 2/1+\beta$, Eqn. 36b), and amplified at the downstream junction ($T = 2/(1+1/\beta)$). Thus, the transmission coefficient of the first transmitted wave is

$$T_1 = \frac{4\beta}{(1+\beta)^2} \tag{39}$$

The second transmitted wave experiences an additional reflection at each end of the chamber ($R = (1 - 1/\beta) / (1 + 1/\beta)$, Eqn. 36a),

$$T_2 = \frac{4\beta}{(1+\beta)^2} \left(\frac{\beta-1}{\beta+1}\right)^2 \tag{40}$$

It follows that,

$$T_i = \beta \left(\frac{2}{1+\beta}\right)^2 \left(\frac{\beta-1}{\beta+1}\right)^{2(i-1)} \tag{41}$$

After the initial reflection, when the shock enters the chamber ($R = (1-\beta)/(1+\beta)$), the expression for the subsequent reflected waves is,

$$R_i = \beta \left(\frac{2}{1+\beta}\right)^2 \left(\frac{\beta-1}{\beta+1}\right)^{2i-3} \qquad i > 1 \tag{42}$$

Interestingly, the series for the transmitted waves sums to one, as the total amplitude of the transmitted waves is equal to that of the incident shock. Except for the first reflected wave, which is an expansion, all of the rest are compressions. The total amplitude of the compressions is the negative of the amplitude of the expansion.

After sufficient time, the reflected series of waves will coalesce because of nonlinear effects. Thus, the reflected disturbance

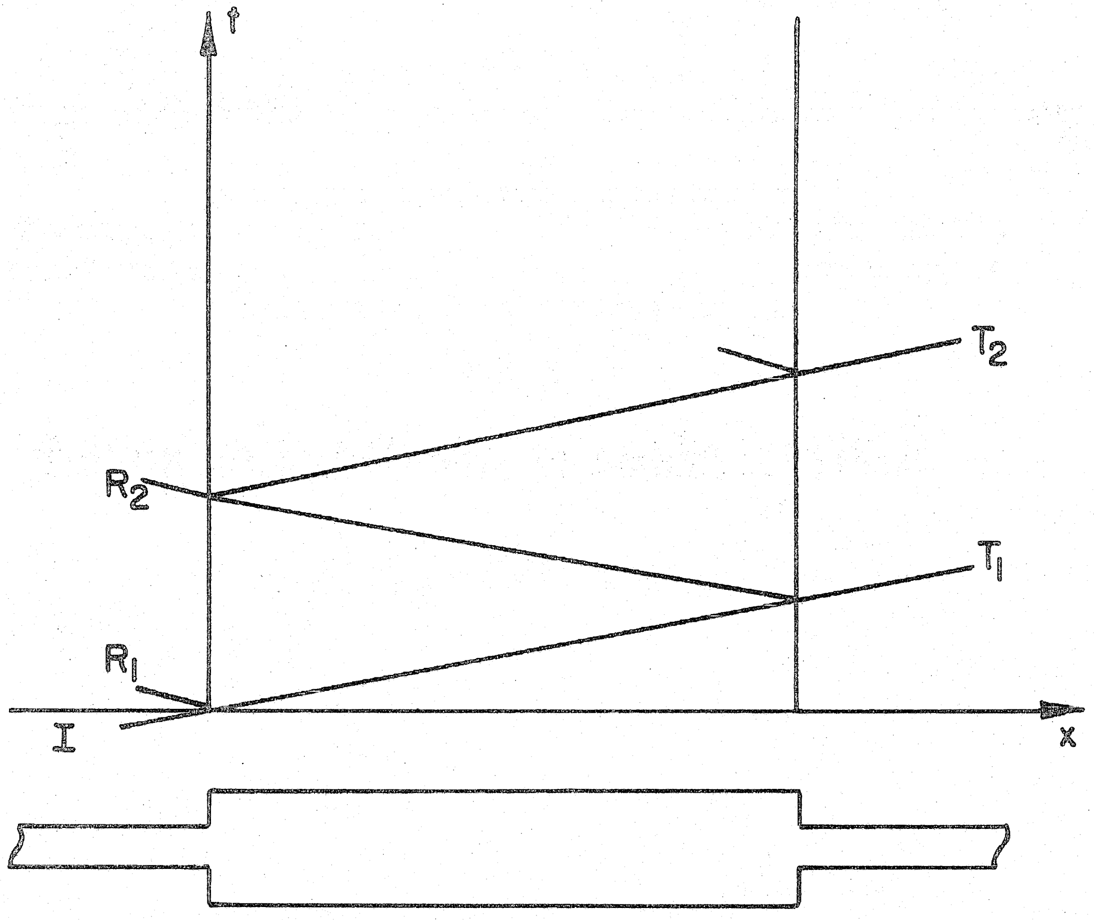

FIGURE 23 EXPANSION CHAMBER SYSTEM

tends to cancel itself. Similarly, the transmitted series of shocks will coalesce. Asymptotically, the strength of the shock front will be equal to the strength of the incident shock.

An energy balance is useful when discussing muffler performance. The transmitted energy is obtained by summing the squares of the transmission coefficients,

$$E_T = \sum_{i=1}^{\infty} \left(\beta \left(\frac{2}{1+\beta} \right)^2 \left(\frac{\beta-1}{\beta+1} \right)^{2(i-1)} \right)^2$$

or

$$E_T = \frac{2\beta}{1+\beta^2} \tag{43}$$

which is equal to unity for constant area (B = 1), and less than one for all other area ratios. The reflected energy is obtained by summing the squares of the reflection coefficients,

$$E_R = \left(\frac{1-\beta}{1+\beta} \right)^2 + \sum_{i=2}^{\infty} \left(\beta \left(\frac{2}{1+\beta} \right)^2 \left(\frac{\beta-1}{\beta+1} \right)^{2i-3} \right)^2$$

or

$$E_R = \frac{(\beta-1)^2}{1+\beta^2} \tag{44}$$

It is clear that the energy in the reflected and transmitted waves should equal the input energy, since we have not accounted for any dissipation.

$$E_{INPUT} = 1$$

$$E_{OUTPUT} = E_R + E_T = \frac{(\beta-1)^2}{1+\beta^2} + \frac{2\beta}{1+\beta^2} = 1 \tag{45}$$

The function of an expansion chamber is to reflect a portion of the energy in the incident shock back upstream, while permitting the remainder to be transmitted.

3.4 Extensions

3.4.1 Outlet or Inlet Extensions

When the inlet to an area expansion is extended beyond the junction, the incident wave produces a series of waves propagating in the upstream and downstream tubes (figure 24). Each transmitted wave is weaker than the transmitted wave produced when the inlet is not extended. The first transmitted wave is weaker because some energy is diffracted around the extension into the annulus.

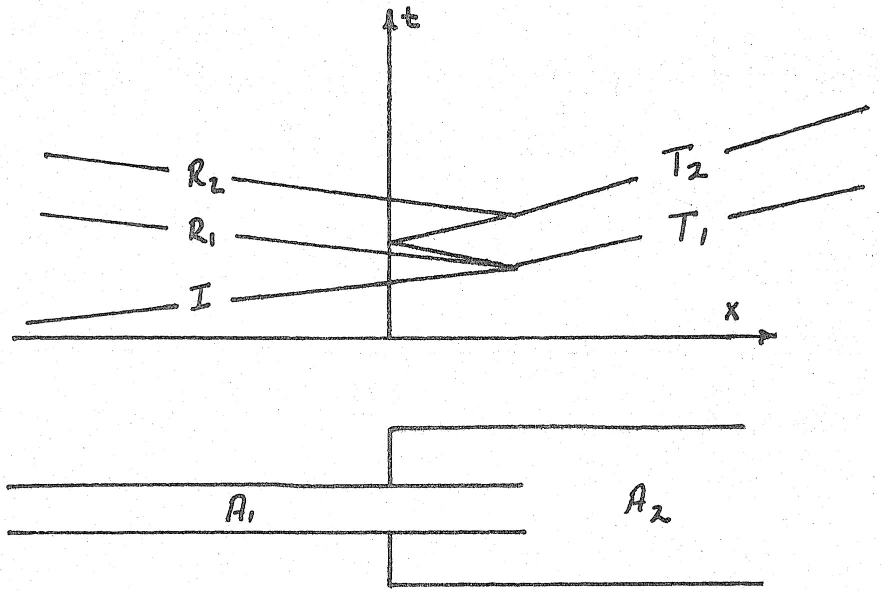

WAVE DIAGRAM FOR AREA EXPANSION WITH INLET EXTENSION

Figure 24

If we interpret equations 36a and b as stating that the reflection and transmission coefficients depend on the ratio of the area occupied by the transmitted wave to the area occupied by the reflected wave, this formula can be modified to account for the additional wave in the annulus. The area ratio of the junction is modified to the ratio of the sum of the annulus and the downstream tube areas to the inlet pipe area,

$$\beta_1^* = \frac{A_2 + (A_2 - A_1)}{A_1} = 2\beta - 1 \tag{46}$$

where β_1^* is the effective area ratio. Note that the effective area ratio is always larger than the area ratio of the junction. This approach is reasonable at lowest order, so equation 7 should only be used in equations 36a and 36b.

$$T_1 = \frac{1}{\beta} \tag{47a}$$

$$R_1 = \frac{1-\beta}{\beta} \tag{47b}$$

When the wave in the annulus arrives at the end of the inlet after reflecting from the end of the annulus, a second wave in transmitted. Using the effective area ratio approach,

$$\beta_2^* = \frac{A_2 + A_1}{A_2 - A_1} = \frac{\beta + 1}{\beta - 1} \tag{48}$$

is the effective area ratio for this interaction. The second transmitted wave is given by,

$$T_2 = T_1 \cdot \frac{2}{1 + \beta_2^*} \qquad \frac{\beta - 1}{\beta} \tag{49}$$

or

$$T_i = R_i = (\beta - 1)\left(\frac{-1}{\beta}\right)^i \qquad i > 1 \tag{50}$$

The transmitted energy for the case of an extended inlet area expansion can be compared to the case without the extension. For the area expansion, there is only one transmitted wave ($T = 2/1 + \beta$ or $E_T = 4/(1 + \beta)^2$). For the extension, the transmitted energy is

$$E_{T*} = \left(\frac{1}{\beta}\right)^2 + \sum_{i=2}^{\infty}\left((\beta - 1)\left(\frac{-1}{\beta}\right)^i\right)^2 = \frac{2}{\beta(\beta+1)} \tag{51}$$

Further, note that the ratio of the transmitted energy for these two cases is

$$\frac{E_{T*}}{E_T} = \frac{1+\beta}{2\beta} = \begin{cases} \text{Less than one} & \beta > 1 \\ \text{Equal to one} & \beta = 1 \end{cases}$$

Therefore, the extended inlet area expansion is a better reflector and a worse transmitter of energy than the standard area expansion.

Now consider figure 25, in which the outlet to an area contraction is extended into the upstream tube. Again, the incident wave produces a series of waves in the upstream and downstream tubes. Each transmitted wave is weaker than the single transmitted wave produced when the outlet is not extended. Using the same approach as was used for the extended inlet, we can formulate equations for the transmission and reflection coefficients.

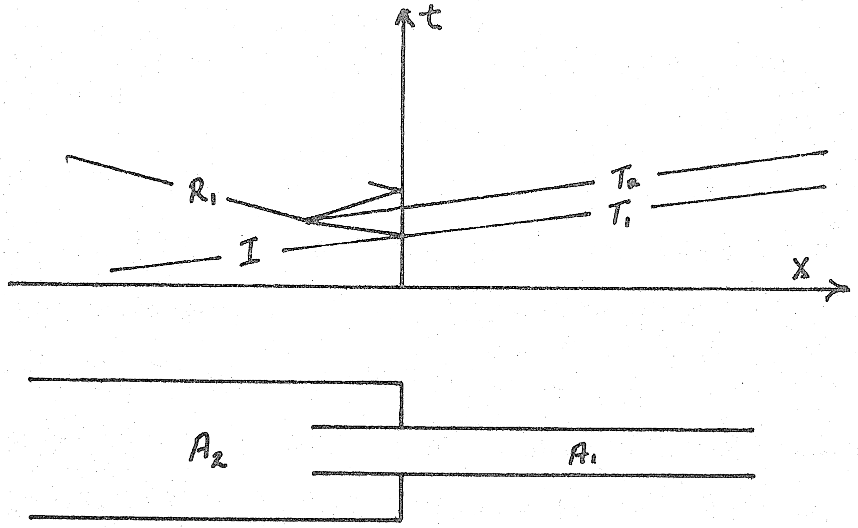

WAVE DIAGRAM
FOR AREA CONTRACTION WITH OUTLET EXTENSION

Figure 25

The first wave transmitted is not affected by the junction, as it is cut from the incident wave by the extended outlet and passed into the downstream tube unamplified. Thus, the transmission coefficient of the first wave in the downstream tube is unity.

The remainder of the incident wave in the annulus generates the series of pairs of waves which propagate away from the junction in the upstream and downstream tubes. The first pair of waves is generated when the wave in the annulus arrives at the end of the extension after reflecting from the closed end. The effective area ratio formulation of this interaction gives,

$$\beta^* = \frac{A_2 + A_1}{A_2 - A_1} = \frac{\beta + 1}{\beta - 1} \tag{52}$$

so that the strength of the waves which propagate away from the junction in the upstream and downstream tubes is,

$$T_2 = R_1 = \frac{2}{1+\beta^*} = \frac{\beta-1}{\beta} \tag{53}$$

or

$$T_{i+1} = R_i = -(\beta-1)\left(\frac{-1}{\beta}\right)^i \tag{54}$$

The transmitted energy for the case of an extended outlet area area contraction can be compared to the case without the extension. For the area contraction, there is only one transmitted wave ($T = 2/(1+1/\beta)$ or $E_T = (2\beta/1+\beta)^2$). For the extension, the transmitted energy is

$$E_{T*} = 1^2 + \sum_{i=2}^{\infty}\left(-(\beta-1)\left(\frac{-1}{\beta}\right)^i\right)^2 = \frac{2\beta}{\beta+1} \tag{55}$$

Further, note that the ratio of the transmitted energy for these two cases is

$$\frac{E_{T*}}{E_T} = \frac{\beta+1}{2\beta} = \begin{cases} \text{Less than one} & \beta > 1 \\ \text{Equal to one} & \beta = 1 \end{cases}$$

Therefore, the extended outlet area contraction is a better reflector and a worse transmitter of energy than the standard area contraction.

3.4.2 Expansion Chamber with Inlet Extension

The extension of the inlet pipe into the expansion chamber results in an improvement of performance. The geometry and X-T diagram is shown in figure 26.

Some introduction is in order here. For this geometry, there is an infinite series of an infinite series, etc., of

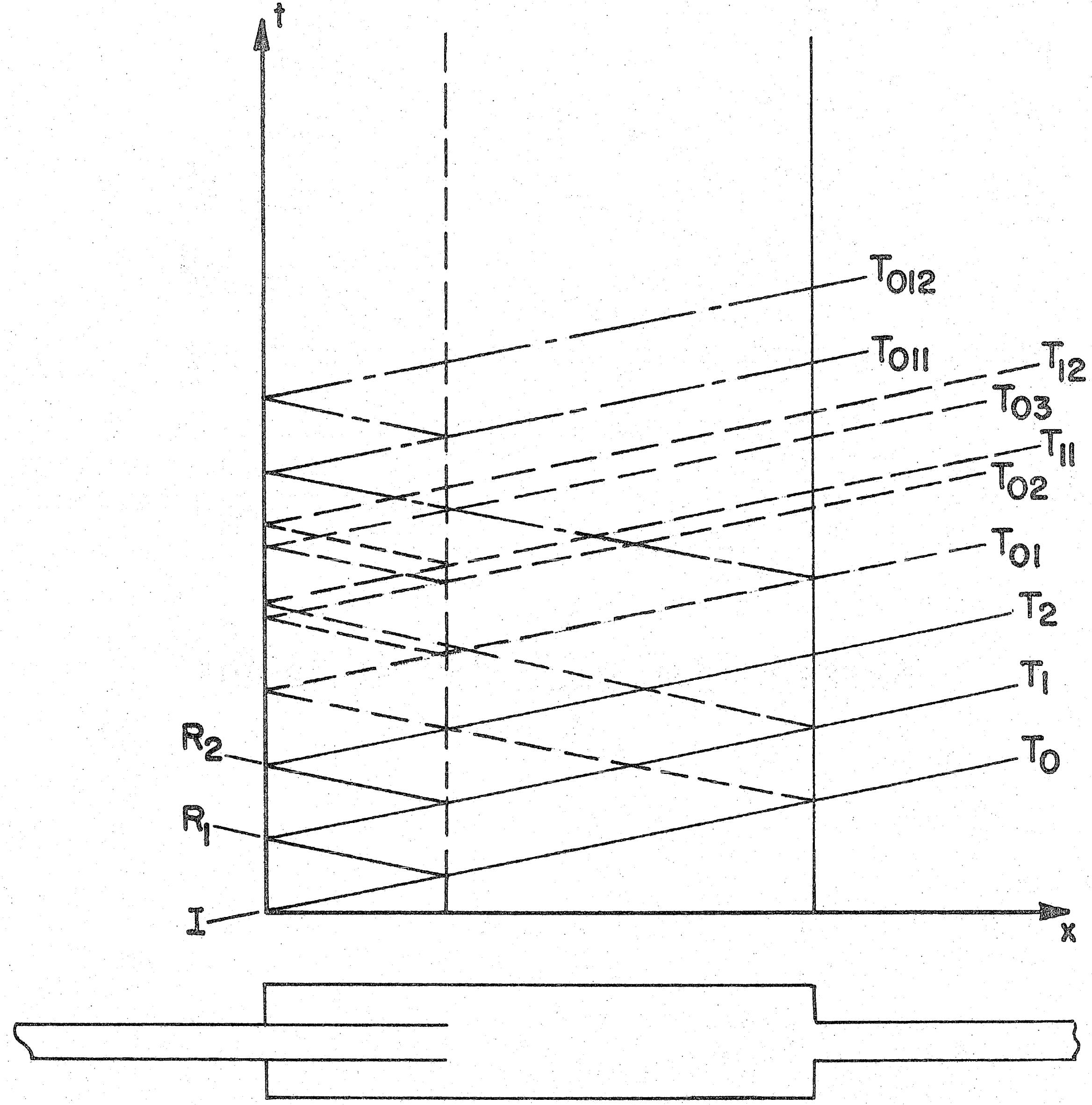

FIGURE 26 EXTENDED INLET SYSTEM

transmitted waves, and the selection of the numbering scheme is rather crucial. The numbering scheme can be important in two ways, by (1) minimizing the amount of computation and (2) insuring that account has been taken of all the waves. Further, we will only compute the transmitted waves.

The transmitted waves with one subscript, T_i, are obtained by using the equations for an extended inlet junction followed by an area contraction

$$T_1 = \frac{1}{\beta}\left(\frac{2}{1+\beta}\right)$$

$$T_i = (\beta-1)\left(\frac{-1}{\beta}\right)^i \left(\frac{2\beta}{1+\beta}\right) \qquad i>1 \qquad (56)$$

The transmitted waves with two subscripts, T_{ij}, are obtained by noting that they have been eeflected from the area contraction once (and only once). Each wave which reflects from the downstream contraction to the left acts as the input wave to an extended outlet area contraction (Eqn. 54 gives the reflected waves to the right).

$$\left.\begin{array}{l} T_{ij} = \frac{1}{\beta} \\ \\ T_{ij} = (\beta-1)\left(\frac{-1}{\beta}\right)^i \end{array}\right\} \left(\frac{\beta-1}{\beta+1}\right)\left(\frac{\beta-1}{\beta}\right)\left(\frac{-1}{\beta}\right)^j\left(\frac{2\beta}{\beta+1}\right) \begin{array}{r} j\geq 1 \\ \\ \\ i>1,\ j\geq 1 \end{array} \qquad (57)$$

The last term is the standard area contraction.

At this point, note that the number of subscripts, minus one, is equal to the number of reflections from the downstream contraction that a given transmitted wave has encountered. Also, the form of equation 57 can be reduced to

$$T_{ij} = T_i \left(\frac{\beta-1}{\beta+1}\right) T_{j+1} \left(\frac{2\beta}{\beta+1}\right) \tag{58}$$

It follows that the transmitted wave with three subscripts can be written as

$$T_{ijk} = T_i \left(\frac{\beta-1}{\beta+1}\right)^2 T_{j+k+2} \left(\frac{2\beta}{1+\beta}\right) \tag{59}$$

For the case of the transmitted waves with α subscripts

$$T_{ijk\cdots\cdots} = T_i \left(\frac{\beta-1}{\beta+1}\right)^{\alpha-1} T_{j+k\cdots\cdots\alpha-1} \left(\frac{2\beta}{\beta+1}\right) \tag{60}$$

Now to compute the total transmitted energy the sum of the squares of the amplitudes of all the transmitted waves is computed. One point here is that we will assume that none of the transmitted waves ever overtakes another. The sum of the squares of the series with one subscript is

$$E_{T_1} = \frac{1}{\beta^2} \left(\frac{2\beta}{\beta+1}\right)^3$$

for two subscripts $E_{T_2} = E_{T_1} \cdot \left(\frac{\beta-1}{\beta+1}\right)^3$

for three subscripts $E_{T_3} = E_{T_1} \cdot \left(\frac{\beta-1}{\beta+1}\right)^6$

leaving the entire transmitted energy as the sum of the above,

$$E_T = \frac{4\beta}{1+3\beta^2} \tag{61}$$

3.4.3 Expansion Chamber with Outlet Extension

The extension of the outlet pipe into the expansion chamber results in the same improvement of performance as does the inlet extension. The geometry is shown in figure 27, where the X-T diagram identifies the numbering scheme.

The transmitted waves with one subscript, T_i, are obtained by using the equations for an area expansion followed by an extended outlet junction.

$$T_0 = \frac{2}{1+\beta}$$

$$T_i = \frac{2}{1+\beta}(1-\beta)\left(\frac{-1}{\beta}\right)^i \qquad i \geq 1 \tag{62}$$

The transmitted waves with two subscripts, T_{ij}, are obtained by noting that they have reflected from the upstream junction once (and only once). For each wave with one subscript, which is transmitted, a wave with the same strength is transmitted back into the chamber. This wave reflects from the upstream junction and then acts as a new input wave to the extended outlet junction.

$$T_{ij} = T_i\left(\frac{\beta-1}{\beta+1}\right)\left(\frac{\beta+1}{2}\right)T_j \qquad i \geq 1\ ,\ j \geq 0 \tag{63}$$

Again, the number of subscripts, minus one, is equal to the number of reflections from the upstream junction that a given transmitted wave has encountered. For the case of (α) reflections, the result is

$$T_{ij\ldots\ldots p} = \left(\frac{\beta-1}{2}\right)^{\alpha} T_i\, T_j \,\ldots\ldots T_p \tag{64}$$

(where all indices except (p) range from one to infinity and p ranges from zero to infinity).

Now to compute the total transmitted energy, the sum of the squares of the transmission coefficients is computed. The result is

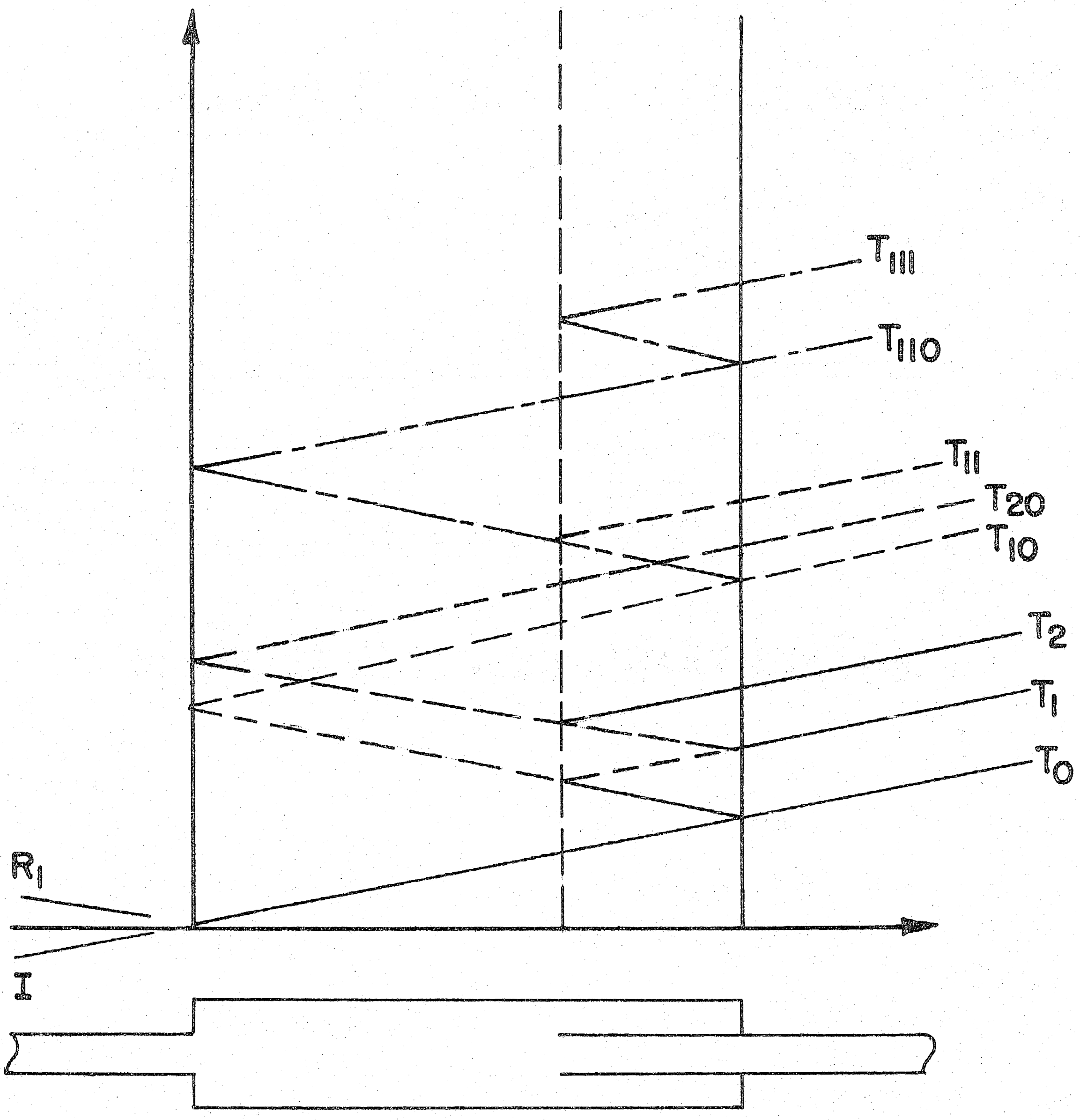

FIGURE 27 EXTENDED OUTLET SYSTEM

identical to the result for the extended inlet,

$$E_{T_1} = \frac{1}{\beta^2} \left(\frac{2\beta}{1+\beta} \right)^3$$

$$E_{T_N} = E_{T_1} \cdot \left(\frac{\beta-1}{\beta+1} \right)^{3(N-1)}$$

or the total transmitted energy is

$$E_T = \frac{4\beta}{1+3\beta^2} \tag{65}$$

3.5 Sound Radiation from Open Pipes

To connect the waves in the tailpipe to the radiated noise, we consider the arrival of a plane weak shock at the open end of a circular tailpipe. We will show that each shock which reaches the end of the tailpipe radiates a narrow pulse to the free field. The pulse width is a function of tailpipe diameter and viewing angle ($\Delta t = 0(D/a)$), where (D) is the diameter and (a) is the speed of sound. The pulse amplitude varies inversely with distance from the source. With this relation between the wave in the tailpipe and the pulse in the free field, the radiated noise or the sound pressure level, SPL, produced by an acoustic shock can be calculated.

In general, a series of waves are transmitted into the tailpipe from the muffler. If the spacing between the waves in the tailpipe is such that each produces a radiated pulse independent of the others, the total SPL can be estimated.

3.5.1 Radiated Waveforms

The sound radiation produced by the reflection of a weak shock from the open end of a pipe can be modeled as if it were created by a distribution of sources in the exit plane. The distribution of source strengths is obtained by calculating the volume flux induced during the reflection process. Since the pressure field is related to the time rate of change of the volume flux, the essential quantity is the velocity in the exit plane. The tailpipe exit is flush with a flat baffle of infinite dimension.

The velocity potential for a point source at the origin in free space, emitting a volume flux, f(t), is

$$\phi_p = \frac{1}{4\pi r} f(at - r) \tag{66}$$

When there is a ground plane or baffle, the velocity potential for a point source is constructed by the method of images. When the source is located in the ground plane, so is its image. The volume flux of the source and its image are equal and add to give twice the volume flux due to the source in free space. The combination gives

$$\phi_p = \frac{1}{4\pi r} 2 f(at - r) \tag{67}$$

The contribution from each source in the exit plane of the tube is summed by integration,

$$\phi(r, \theta, t) = \frac{-1}{2\pi} \int_S \frac{f(at - \tilde{r})}{\tilde{r}} \, dS \tag{68}$$

where the geometry is shown in figure 28. The pressure is related to the velocity potential ($p = -\rho \phi_t$), or

$$p(r, \theta, t) = \frac{\rho}{2\pi} \frac{\partial}{\partial t} \int_S \frac{f(at - \tilde{r})}{\tilde{r}} \, dS \tag{69}$$

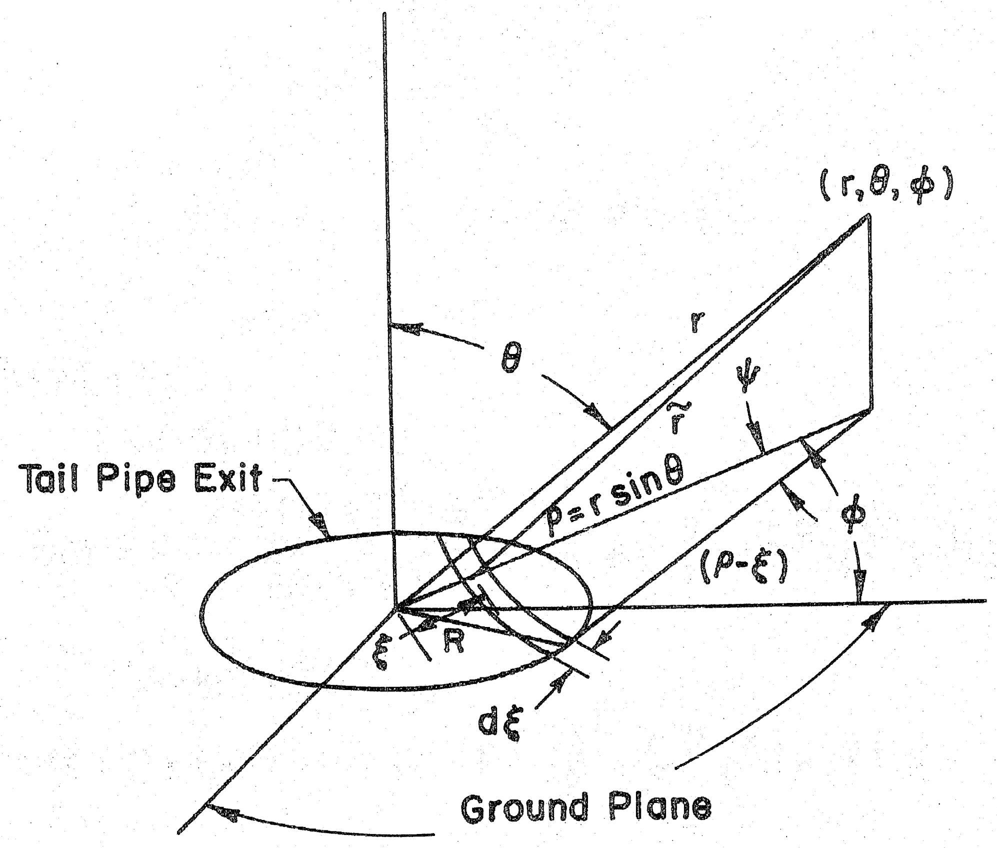

Geometry:

Law Of Cosines

$$\cos\psi = \frac{\rho^2+(\rho-\xi)^2-R^2}{2\rho(\rho-\xi)} \quad \text{Or} \quad \psi \simeq \frac{1}{\rho}\sqrt{R^2-\xi^2}+O\left(\frac{R}{\rho}\right)^3$$

Element Of Area

$$dS = 2\psi(\rho-\xi)\,d\xi \quad \text{Or} \quad dS \simeq \frac{2}{\rho}\sqrt{R^2-\xi^2}\,(\rho-\xi)\,d\xi$$

FIGURE 28

The calculation will be done in two parts. Initially, we will fix the source strength by using the velocity behind the incident shock,

$$f(t) = \frac{\Delta p}{\rho a} H(t) \tag{70}$$

where H(t) is the Heaviside function. Later, in an approximate manner, we will account for the additional details of the velocity history during the reflection process.

Substitution of equation 70 into 69 gives

$$p(r,\theta,t) = \frac{\Delta p}{2\pi} \int_S \frac{\delta\left(\frac{at}{R} - \frac{\tilde{r}}{R}\right)}{\frac{\tilde{r}}{R}} \frac{dS}{R^2} \tag{71}$$

The use of the geometry shown in figure 28 gives

$$p(r,\theta,t) = \frac{\Delta p}{2\pi} \int_{-1 \text{ or } \left(\frac{-\rho}{R}\right) \text{ if } \rho < R}^{1} \frac{\delta\left(\frac{at}{R} - \sqrt{\left(\frac{r}{R}\right)^2 + \eta^2 - 2\eta\frac{r}{R}\sin\theta}\right) 2\psi(\eta)\left(\eta - \rho/R\right)}{\sqrt{\left(\frac{r}{R}\right)^2 + \eta^2 - 2\eta\frac{r}{R}\sin\theta}} d\eta \tag{72}$$

where the variable of integration, $\eta = \xi/R$. When an integral contains a delta function, the argument of the delta function must be at most a linear function of the variable of integration to use the standard rules for integration of delta functions. Therefore, the following transformation is useful,

$$\tau = \frac{\tilde{r}(\eta)}{R} \quad , \quad d\tau = \frac{d\tilde{r}(\eta)}{d\eta} \cdot \frac{d\eta}{R} \tag{73}$$

where

$$\frac{\tilde{r}(\eta)}{R} = \sqrt{\left(\frac{r}{R}\right)^2 + \eta^2 - 2\eta\frac{r}{R}\sin\theta}$$

and

$$\frac{1}{R}\frac{d\tilde{r}(\eta)}{d\eta} = \frac{\eta - \frac{r}{R}\sin\theta}{\tau}$$

Substitution of the change of variables gives,

$$p(r,\theta,t) = \frac{\Delta p}{\pi} \int_{\tau(-1) \text{ or } \tau(\frac{-\rho}{R})}^{\tau(1)} \delta\left(\frac{at}{R} - \tau\right) \psi(\eta(\tau))\, d\tau \tag{74}$$

which can be integrated using the standard rules for integration of delta functions,

$$p(r,\theta,t) = \Delta p \, \frac{\psi(\eta(\frac{at}{R}))}{\pi} \tag{75}$$

where

$$\eta\left(\frac{at}{R}\right) = \frac{r}{R}\left(\sin\theta - \sqrt{\sin^2\theta - \left(1 - \left(\frac{at}{R}\frac{R}{r}\right)^2\right)}\right)$$

and

$$\cos\psi(\eta) = \frac{(\rho/R)^2 + (\rho/R - \eta)^2 - 1}{2\,\rho/R\,(\rho/R - \eta)}$$

This result is quite interesting in that it shows that the pressure at any time is proportional to the angular range of integration, Ψ, at that instant in time (Fig. 28). Further, there are special cases where the the time dependence of Ψ is quite simple.

For example, on the axis where the angular range of integration is 2π, we find that the pressure is

$$p = \Delta p \quad , \quad r < at < r\sqrt{1 + (R/r)^2}$$

The information that the wall of the tube has stopped has not reached this part of the sound field. This lack of decay only exists in the area directly above the exit plane, $\rho \leq R$. Also the duration of the pulse becomes increasingly small as the pulse propagates away from the source.

Another simple case is on the ground plane ($\rho = r$ and $\theta = \pi/2$), where

$$\eta = \frac{r}{R}\left(1 - \frac{at}{R}\right)$$

and

$$\psi \simeq \frac{R}{r}\sqrt{1-\eta^2} + o\left(R/\rho\right)^3$$

Substitution into equation 75 gives

$$p\left(r, \frac{\pi}{2}, t\right) = \Delta p \frac{R}{\pi r}\sqrt{1 - \left(\frac{r-at}{R}\right)^2} \quad , \; r-R < at < r+R \qquad (76)$$

It is interesting to note that there is a striking degree of directionality in the peak pressure, as shown by

$$P_{max} = \begin{cases} \Delta p & \rho < R \\ \frac{1}{2}\Delta p & \rho = R \\ \frac{R}{\pi r}\Delta p & \rho < R \end{cases}$$

In the region near the axis the information about the end of the tube is not communicated to the wave front. As the point of observation exceeds the tube radius, the maximum pressure decays quickly to a value depending on the distance of travel, R/r.

For the approximate analysis, we calculate the pressure pulse only on the ground plane but go on to account for the additional source strength due to the reflection. The fluid in the exit plane accelerates to the velocity behind the shock, upon its arrival, in a very short time. Diffracted waves created by the shock at the exit act to double the velocity. This process is at best axisymmetric, though we will assume that the velocity doubles and the pressure decays to zero in a uniform manner. The time scale of this event is the order of the tubes characteristic time, D/a, and has been calculated by Rudinger (1957) for acoustic shocks.

Rudinger uses the acoustics approximation and takes a step function input wave. The spectrum of the reflected wave, $P_R(\omega)$, is related to the spectrum of the incident wave, $P_i(\omega)$, by the impedance of the open end,

$$P_R(\omega) = P_i(\omega)\, e^{-2\gamma} \tag{77}$$

where ω is the frequency and γ is related to the impedance, z, by

$$z = \rho a \tanh(\gamma) \tag{78}$$

The impedance of the open end of a tube is a function of the ratio of the wave length of the sound to the tube diameter. To calculate the impedance, the slug of fluid in the open end is modeled as a rigid circular piston in an infinite baffle. The pressure field is calculated for sinusoidal vibrations of the piston. The mean pressure acting on the surface of the piston is evaluated. The impedance is the ratio of the R.M.S. pressure to the excitation velocity (Morse and Ingard, 1968).

$$z = \rho a \tanh(\gamma) = \rho a(\alpha - i\chi) \tag{79}$$

where

$$\alpha(W) = 1 - \frac{2}{W} J_1(W)$$

$$\chi(W) = \frac{4}{\pi} \int_0^{\frac{\pi}{2}} \sin(W \cos x) \sin^2 x \, dx$$

and $W = \frac{D}{a} \omega$, the nondimensional frequency.

Then the exit pressure is calculated by integrating over all frequencies,

$$p - p_0 = p_1 - p_0 + \int_{-\infty}^{\infty} p_i(w) e^{-2\gamma(w)} e^{-iwt} dw \qquad (80)$$

where $p_i(\omega)$ is the spectrum of the incident wave. For this work, the velocity is the desired quantity and can be obtained in a similar manner.

$$u - u_0 = \frac{p_1 - p_0}{\rho a} - \frac{1}{\rho a} \int_{-\infty}^{\infty} p_i(w) e^{-2\gamma(w)} e^{-iwt} dw \qquad (81)$$

Rudinger has computed the Fourier integral for the case where the input wave is a step-function. His results show that the pressure changes instantaneously to p_1 at $t = 0$, and decays practically exponentially to p_o in a time, $t \cong 3\frac{D}{a}$. For this analysis, the velocity is taken as $\Delta p/\rho a$ at $t = 0$, and increases in the same manner as the pressure decreases, to twice $\Delta p/\rho a$ in a time, $t \cong 3\frac{D}{a}$,

$$u(t) = \frac{\Delta p}{\rho a} \left(2 - e^{-Bt}\right) H(t) \qquad (82)$$

where the effective velocity, $u(t)$, is uniform in the exit plane. The decay constant, B, is the inverse of the reflection time and is taken as $1.15\, a/D$, which is obtained by exponential fit to the numerical results of Rudinger.

The volume flux per unit area is

$$f(t) = \frac{\Delta p}{\rho a}\left(2 - e^{-Bt}\right) H(t) \tag{83}$$

The velocity potential is obtained in the same manner as equation 68, and the pressure in the same manner as equation 71. Then the pressure is

$$p(r,\theta,t) = \frac{\Delta p}{2\pi}\left(\int_S \frac{\left(2 - e^{-B(t-\tilde{r}/a)}\right)\delta\left(\frac{at}{R} - \frac{\tilde{r}}{R}\right)}{\frac{\tilde{r}}{R}} \frac{ds}{R^2} + \frac{BR}{a}\int_S \frac{e^{-B\left(t-\frac{\tilde{r}}{a}\right)} H\left(\frac{at}{R} - \frac{\tilde{r}}{R}\right)}{\frac{\tilde{r}}{R}} \frac{ds}{R^2}\right) \tag{84}$$

where the first and second integrals will be denoted by p_1 and p_2. The contribution from the first integral is produced by the shock, while the second integral accounts for the reflection process. Using the far-field approximation for the surface element of integration (Fig. 28), which is valid only near the ground plane, the first integral can be integrated. The result is essentially the same as equation 76.

$$P_1 = \Delta p \frac{R}{\pi r}\sqrt{1 - \left(\frac{r - at}{R}\right)^2} \tag{85}$$

The second integral is not so simple. For short times (or near the wave front), the integrand is nonzero only on a portion of the exit plane, because the Heaviside function is zero for $\tilde{r} >$ at. The area of integration is the overlap of a circle of radius at, centered at a point, r, with the exit of the tailpipe. Here we approximate the boundary of the region of integration due to the circle of radius, at, by a straight line. This approximation is exact to first order, but does have a second order correction (0 $(R/r)^2$).

Therefore, using the approximate geometry, as shown in figure 28, the second integral can be written

$$p_2 = \Delta p \, \frac{BR}{a\pi} \int_{-R}^{R} \frac{e^{-B\left(t - \frac{r-\xi}{a}\right)} H\left(\frac{at}{R} - \frac{r-\xi}{R}\right) \frac{\sqrt{R^2-\xi^2}}{R}}{\frac{r}{R}} \, \frac{d\xi}{R} \tag{86}$$

and further, the Heaviside function can be eliminated by adjusting the range of integration,

$$p_2 = \frac{B_0 R}{2\pi r} \Delta p \begin{cases} \displaystyle\int_{\eta_0}^{1} e^{-\frac{B_0}{2}(\eta-\eta_0)} \sqrt{1-\eta^2} \, d\eta \quad , \quad 1 > \eta_0 > -1 \\ \displaystyle\int_{-1}^{1} e^{-\frac{B_0}{2}(\eta-\eta_0)} \sqrt{1-\eta^2} \, d\eta \quad , \quad -1 > \eta_0 \end{cases} \tag{87}$$

where $\eta = \xi/R$, $\eta_0 = \frac{r-at}{R}$, and $B_0 = B\frac{2R}{a} = 1.15$.

The second integral, p_2, has been numerically computed as a function of time beginning when the wavefront arrives $(t = \frac{r-R}{a}$ or $\eta_0 = 1)$ and ending when the pressure has decayed to $1/20^{th}$ of the peak pressure. Values of the integrand times $B_o/2$, and the contribution from p_1 are plotted as a function of time in figure 28b, where the common term $\frac{\Delta p}{\pi} \frac{R}{r}$ is factored out (note, $p_{max} = \frac{1.41}{\pi} \Delta p \frac{R}{r}$).

3.5.2 Radiated Sound Pressure Level

The sound pressure level can be calculated for the case of repetitive arrival of shocks at the open end of a pipe if the period of

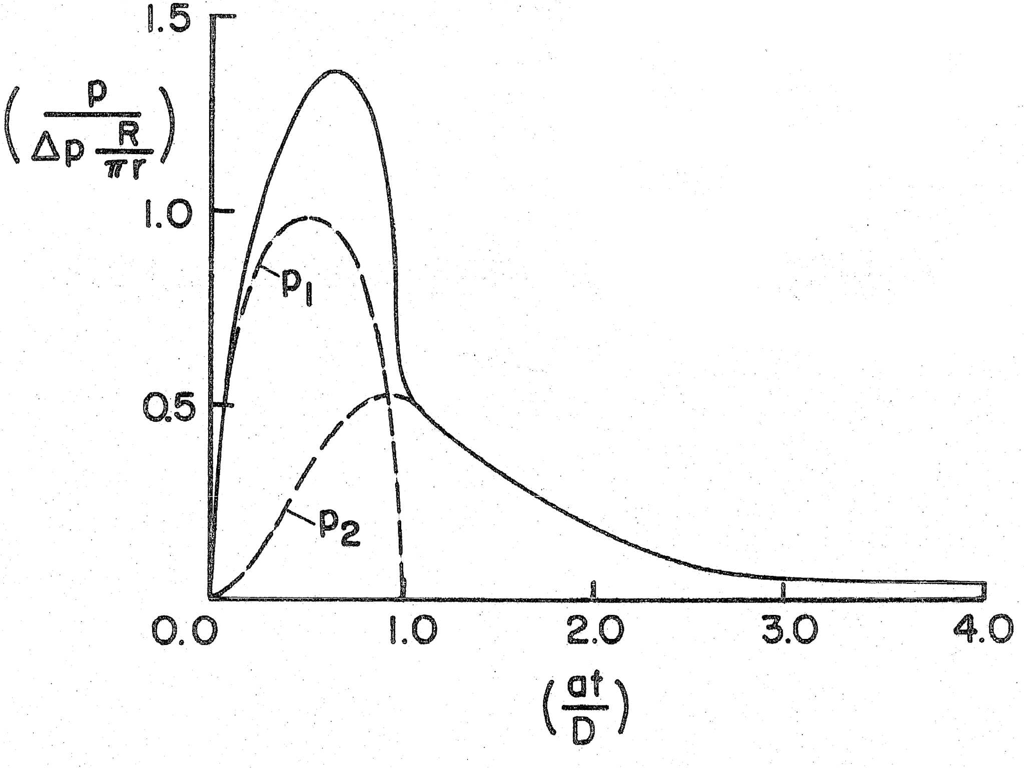

FIGURE 28a RADIATED PRESSURE HISTORY

longer than the characteristic time of the pipe, D/a. The SPL is defined as

$$SPL = \frac{1}{T}\int_0^T p^2(t)\,dt = \left(\Delta p \frac{R}{\pi r}\right)^2 \frac{R}{aT} K \qquad (88)$$

where k is a constant of order one obtained from the integration k = 2.91. The SPL is decibels (p_{ref} = .0002 μBar) is

$$SPL = 10 \, LOG_{10} \left(\left(\frac{\Delta p}{P_{ref.}} \frac{R}{\pi r}\right)^2 \frac{R}{aT} k \right) \qquad (89)$$

and the attenuation is defined as the difference between the local SPL and the SPL of the incident shock, or

$$ATT = 20 \, LOG_{10} \left(\frac{R}{\pi r} \sqrt{K \frac{R}{aT}} \right) \qquad (90)$$

If the shock is first attenuated in the tube before it reaches the open end, then the incident shock amplitude, Δp, is replaced by the transmitted shock amplitude, $T\Delta p$. For the case of perforations, the transmission coefficient was given in equation 22 as $T(\frac{Ae}{A}, \Delta p)$. The attenuation is

$$ATT = 20 \, LOG_{10} \left(\frac{R}{\pi r} \sqrt{K \frac{R}{aT}} \; T\left(\frac{Ae}{A}, \Delta p\right)\right) \qquad (91)$$

When each incident shock produces a series of waves, the transmitted energy function is used. For the case of an expansion chamber, the attenuation is

$$ATT = 10 \log_{10} \left(\left(\frac{R}{\pi r} \right)^2 k \frac{R}{a_T} E_T \right) \qquad (92)$$

where the transmitted energy, E_T, is given by equation 43. For the case of extensions, the transmitted energy is given by either equation 61 or 65.

IV. RESULTS - INTERNAL WAVES

4.1 Perforations

The interaction of a plane weak shock wave with a tube with perforations in the wall is discussed in this section. The shock wave is weakened as it passes perforations because fluid behind the shock is pumped through the perforations to the surroundings. As a direct result of the shock wave passing each perforation, waves are diffracted off the shock. The interaction with the diffracted expansion waves traveling across the shock front weakens the shock. The diffracted waves propagating upstream become one-dimensional and form the reflected wave.

The basic wave interaction, including the effects of incident shock strength and length of perforated tube, is discussed in the first section. The wave amplitudes and empirical data are presented, and their dependence on incident shock strength is discussed. An empirical relation for the discharge coefficient of the perforations is computed from the data and is used to fit the theory to the data. A comparison of the corrected theory with the data shows that use of the linear and quadratic expansions in the theory is valid.

Results from the resonance tube experiments are presented to illustrate the effect of a flow ahead of the shock. In the repetitive excitation case, the shock enters the test section during a portion of the cycle in which there is a strong flow into the tube. The discharge coefficient of the perforations is strongly controlled by the axial flow in the tube, causing results from experiments using repetitive excitation to differ from those using single pulses.

In application, perforations are usually enclosed from the surroundings. The effects of such an enclosure are presented, and a simple model describing these effects is given.

4.1.1 Wave Forms

The single pulse excitation experiments were performed as described in Section 2.3.2. The incident shock Mach numbers were 1.13, 1.16, 1.29, 1.47, and 1.55; and the perforate area ratios were 0.44, 0.89, 1.33, and 1.78. The incident and reflected waves were observed at location U, and the transmitted waves were observed at locations D1 and D2 (Fig. 12).

The pressure traces are shown in figures 29, 30 and 31. Three experiments are presented in each figure. The pictures across the top of each figure show the pressures observed at locations U and D2. The pictures across the bottom of each figure show the pressures observed at location D1 and D2. Table 2 identifies the upper and lower beams and their scales.

Figure 29 presents pressure traces of cases where the shock Mach number was 1.13 and area ratios were 0.44, 0.89, and 1.78. The amplitude of the reflected wave increases with the area ratio. The transmitted wave form, observed at locations D1 and D2, is a simple shock at the low area ratio. At area ratio 0.89, an expansion is seen behind the transmitted front at location D1; further downstream, the expansion has overtaken the shock. A small gradual compression is observed behind the expansion at location D1 and behind the wave front at location D2. At the largest area ratio,

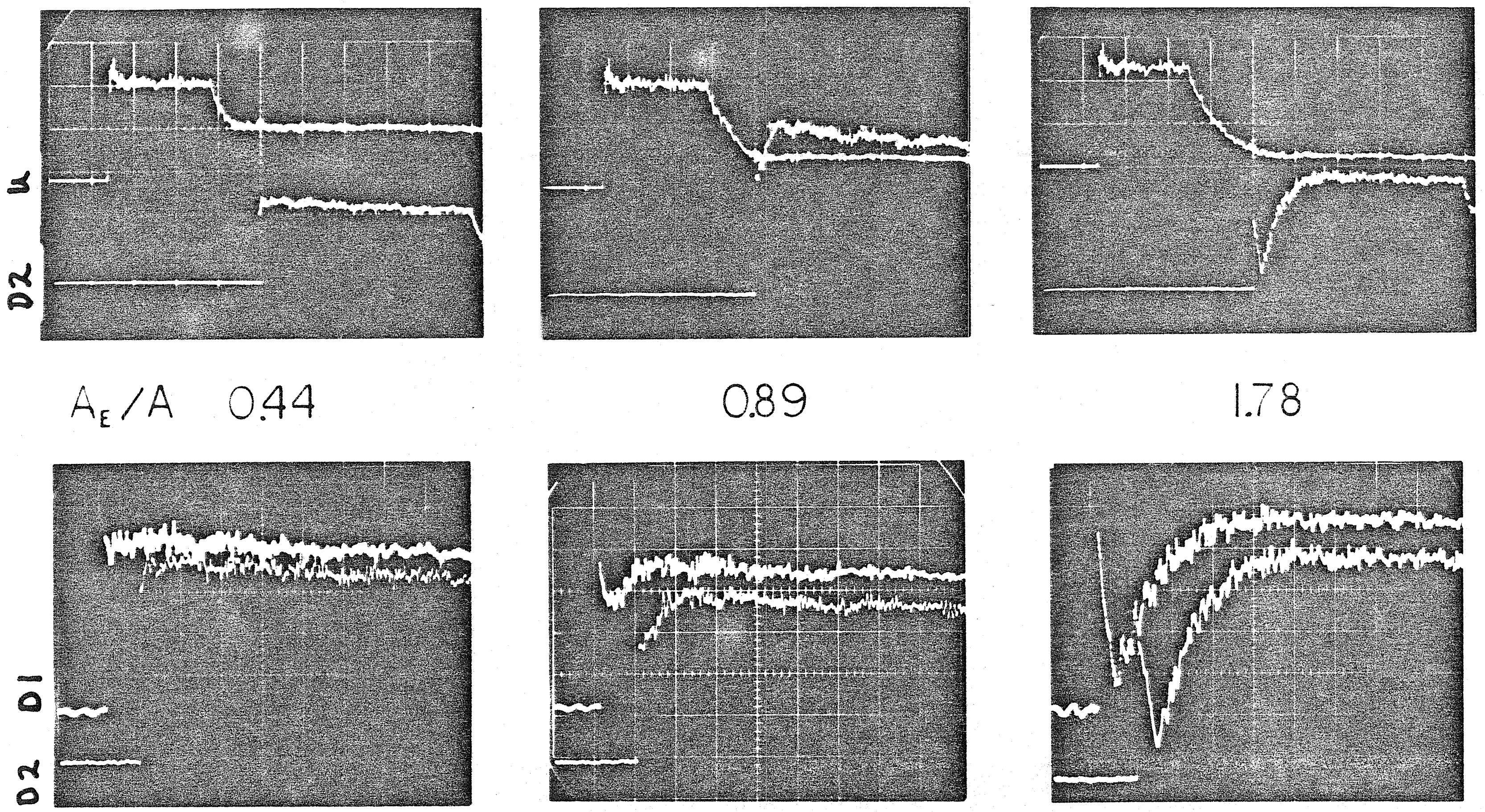

THE EFFECT OF PERFORATED AREA RATIO ON REFLECTED AND TRANSMITTED WAVES. (MACH NO. = 1.13)

FIGURE 29

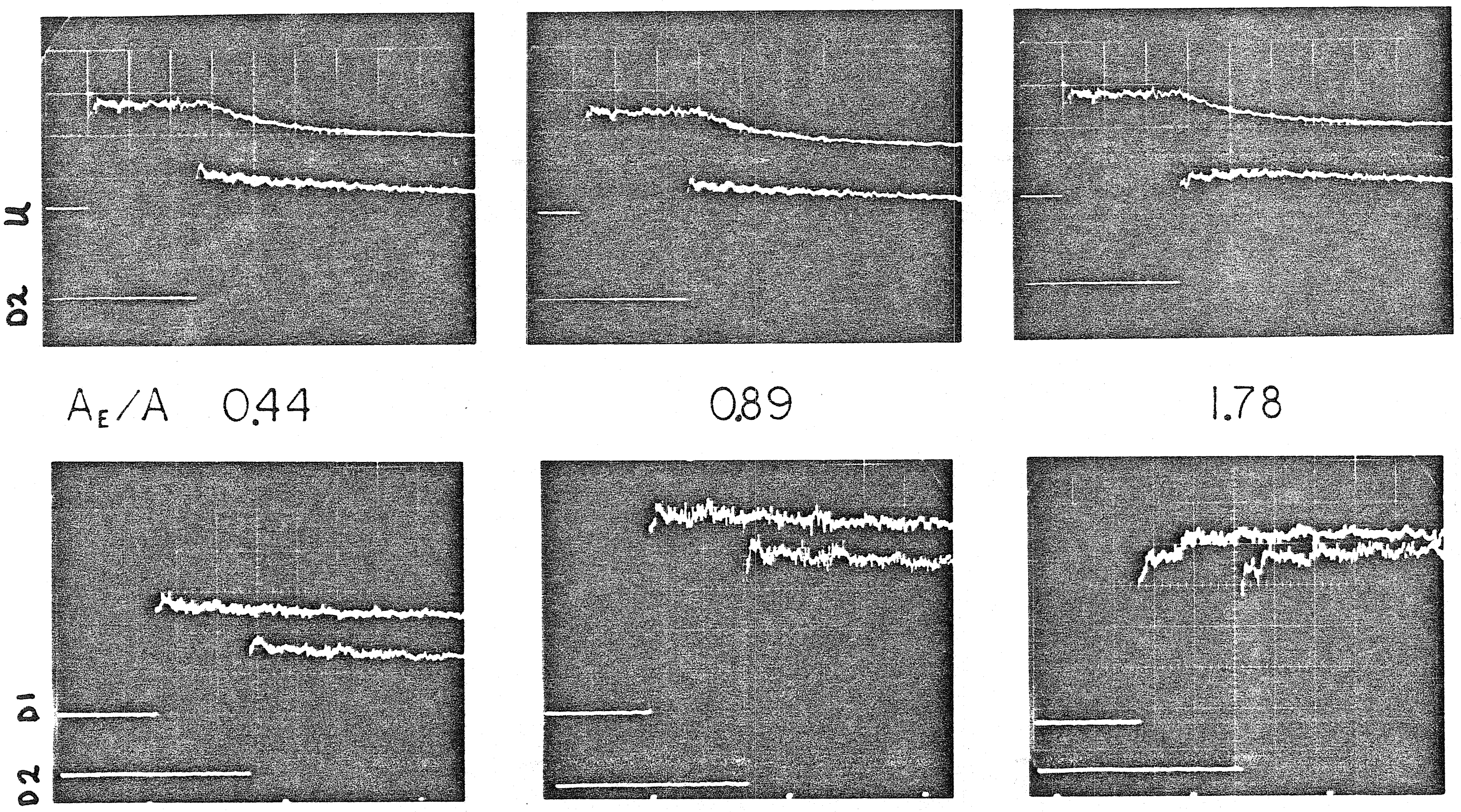

THE EFFECT OF PERFORATED AREA RATIO ON REFLECTED AND TRANSMITTED WAVES. (MACH NO. = 1.55)

FIGURE 30

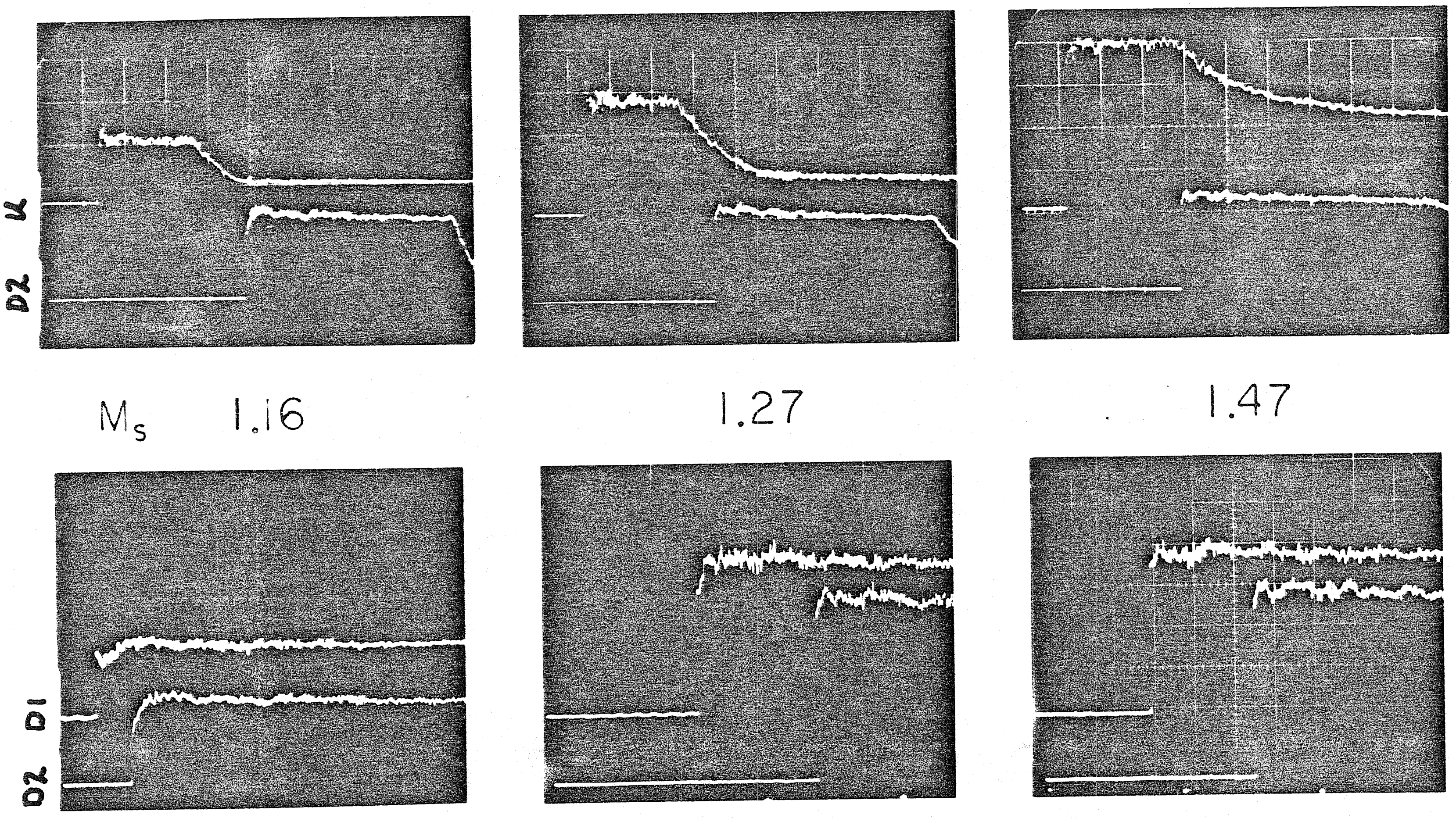

THE EFFECT OF INCIDENT SHOCK MACH NUMBER ON REFLECTED AND TRANSMITTED WAVES. (AREA RATIO = 0.89)

FIGURE 31

TABLE 2

			Figure 29			Figure 30			Figure 31		
			0.44	0.89	1.78	0.44	0.89	1.78	1.16	1.27	1.47
top row	upper beam	V	2.0	2.0	2.0	10.0	10.0	10.0	4.0	4.0	5.0
		H	500								
	lower beam	V	1.8	0.72	0.72	7.2	7.2	7.2	1.8	3.6	7.2
		H	500								
bottom row	upper beam	V	0.83	0.83	0.41	8.4	4.2	4.2	2.1	2.1	4.2
		H	200								
	lower beam	V	0.72	0.72	0.36	7.2	3.6	3.6	1.8	1.8	3.6
		H	200								

V Vertical Scale (psi/cm)
H Horizontal Scale (μs/cm)

the expansion behind the shock front is stronger as it lowers the pressure to p_1. The gradual compression is much stronger and raises the pressure to p_4, the final pressure.

At low incident shock Mach numbers, the reflected wave is an expansion. For small area ratios, the transmitted wave is a shock. For large area ratios, two important points should be emphasized: (1) the perforate area ratio is set by adjusting the length of the uniformly perforated section (a larger perforate area ratio is equivalent to a longer section of perforations), and (2) locations D1 and D2 are at fixed positions in the tube (Fig. 12); and, therefore, their position relative to the perforated section is decreased for increased perforate area ratio. For large area ratios, the transmitted wave form is more complex, including a shock, a sharp expansion, and a slower compression, and must propagate a large distance before attaining its final form. Thus, the transmitted shock continues to weaken after it has passed the perforated section and until the expansion has completely overtaken the shock front. At this point, the wave form is a shock followed by a gradual compression. Finally, after the compression has overtaken the shock, there is only a shock, changing the pressure from p_1 to p_4.

This complex transmitted wave form has also been observed by Szumowski (1972), although his comments do not include a careful discussion of the wave forms. For example, the distance that the transmitted wave must propagate to attain its asymptotic strength must scale not only with its local amplitude, but with the length of the perforated section (locations D1 and D2); the shocks observed are further from their asymptotic strength for larger area ratios.

A one-dimensional model gives a simple but adequate explanation of the gradual compression observed in the transmitted wave. When the incident shock enters the section of the tube with perforated walls, disturbances are created which propagate along the negative characteristics (Fig. 32). As the disturbances pass back through the perforations, they are in turn reflected along positive characteristics. Since the first order reflections, which propagate along C_-, are expansion waves, the second order reflections are compressive. For weak incident shocks, the second order reflections advance toward the transmitted shock very slowly. Further, the rise times for the second order waves would be O(2L/a) at least in the region immediately downstream of the perforations. For an area ratio of 1.78 with perforations of length 10.2 cm, the rise time, 2L/a, should be 560 μsec, which is in qualitative agreement with the observed rise time of 600 μsec (Fig. 29).

The occurrence of a sharp expansion immediately behind the leading shock does not follow from a similar one-dimensional argument as given above. The time scale of the expansion, O(100 μsec), is the order of the transverse travel time, D/a = 110 μsec, rather than the longitudinal travel time. Therefore, the expansion is possibly made up of transverse diffracted waves originating at the interaction of the shock with the individual perforations; however, a quantitative explanation is not complete.

Figure 30 presents pressure traces of experiments at incident shock Mach number 1.55 and area ratios 0.44, 0.89, and 1.78. The

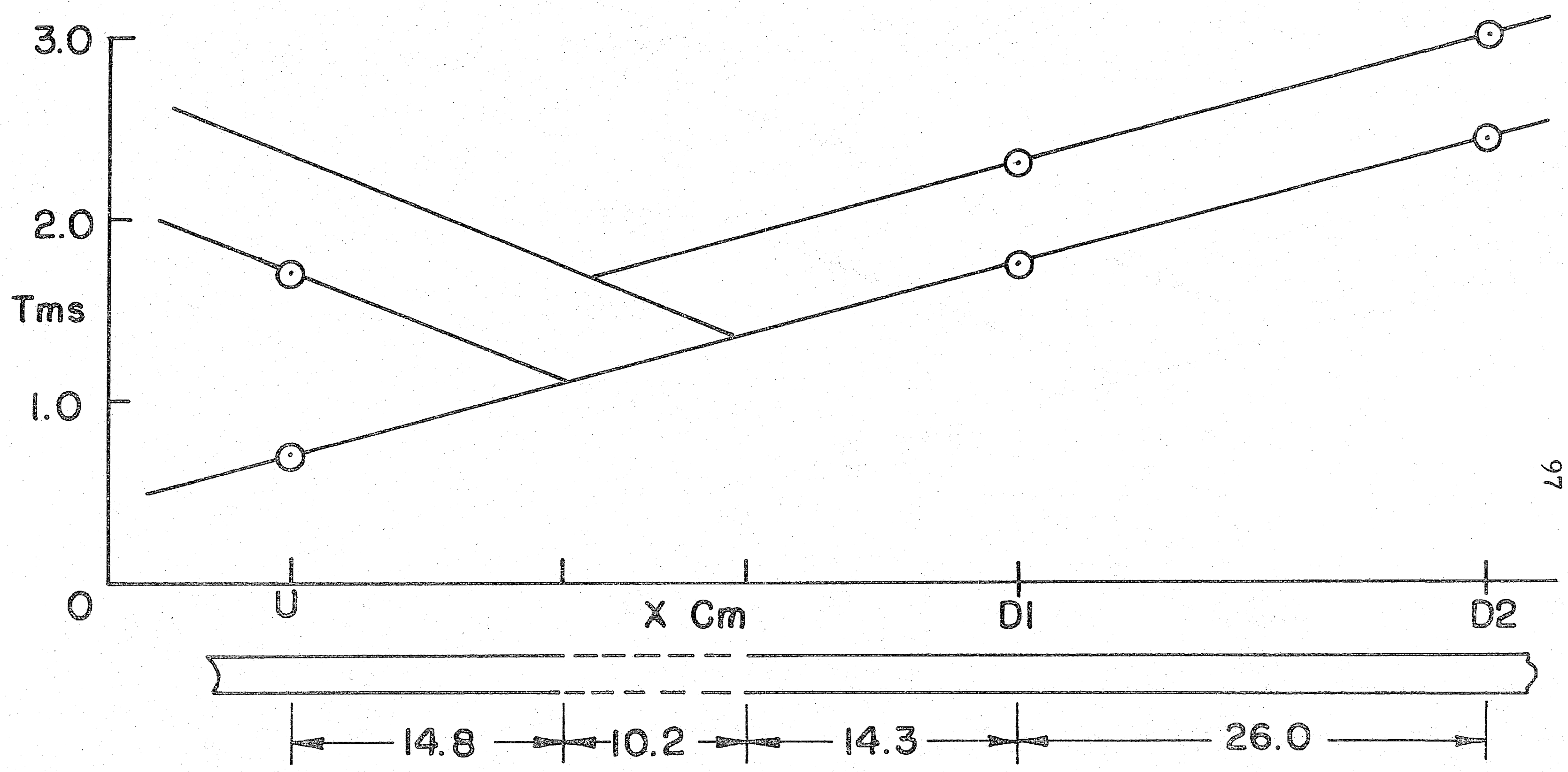

FIGURE 32 AN X-T DIAGRAM FOR THE PROPAGATION OF WEAK SHOCKS PAST LONG SECTIONS OF PERFORATIONS ($M_s = 1.13$; $A_E/A = 1.78$), SHOCK TUBE

transmitted wave is a simple shock except for the largest area ratio case where, at location D1, a slight compression is observed behind the shock front. When the shock reaches location D2, the compression has already overtaken the shock front, so that the wave is a simple shock.

Figure 31 presents pressure traces of experiments at incident shock Mach numbers 1.16, 1.27, and 1.47. The transmitted wave form D1 progresses from shock, expansion, and compression at low incident shock strengths, to a simple shock at high incident shock strength.

4.1.2 Wave Amplitudes

The strengths of the reflected and transmitted waves are normalized using the incident shock strength. In that way, reflection and transmission coefficients may be compared. For the more complex transmitted wave forms, the amplitude is taken to be the final pressure after the gradual compression. The transmission and reflection coefficients are plotted in figures 33a and 33b. The data are plotted against area ratio for each incident shock strength. The attenuation is increased with increasing area ratio. On the other hand, the attenuation is decreased with increasing incident shock strength. At low incident shock strengths, the reflection coefficient increases (negatively) with increasing area ratio but tends to remain constant at higher incident shock strengths.

The above data were processed using the program discussed in Appendix B. The flow conditions in regions two through four, and in the perforation (Fig. 20), are calculated. The discharge coefficient

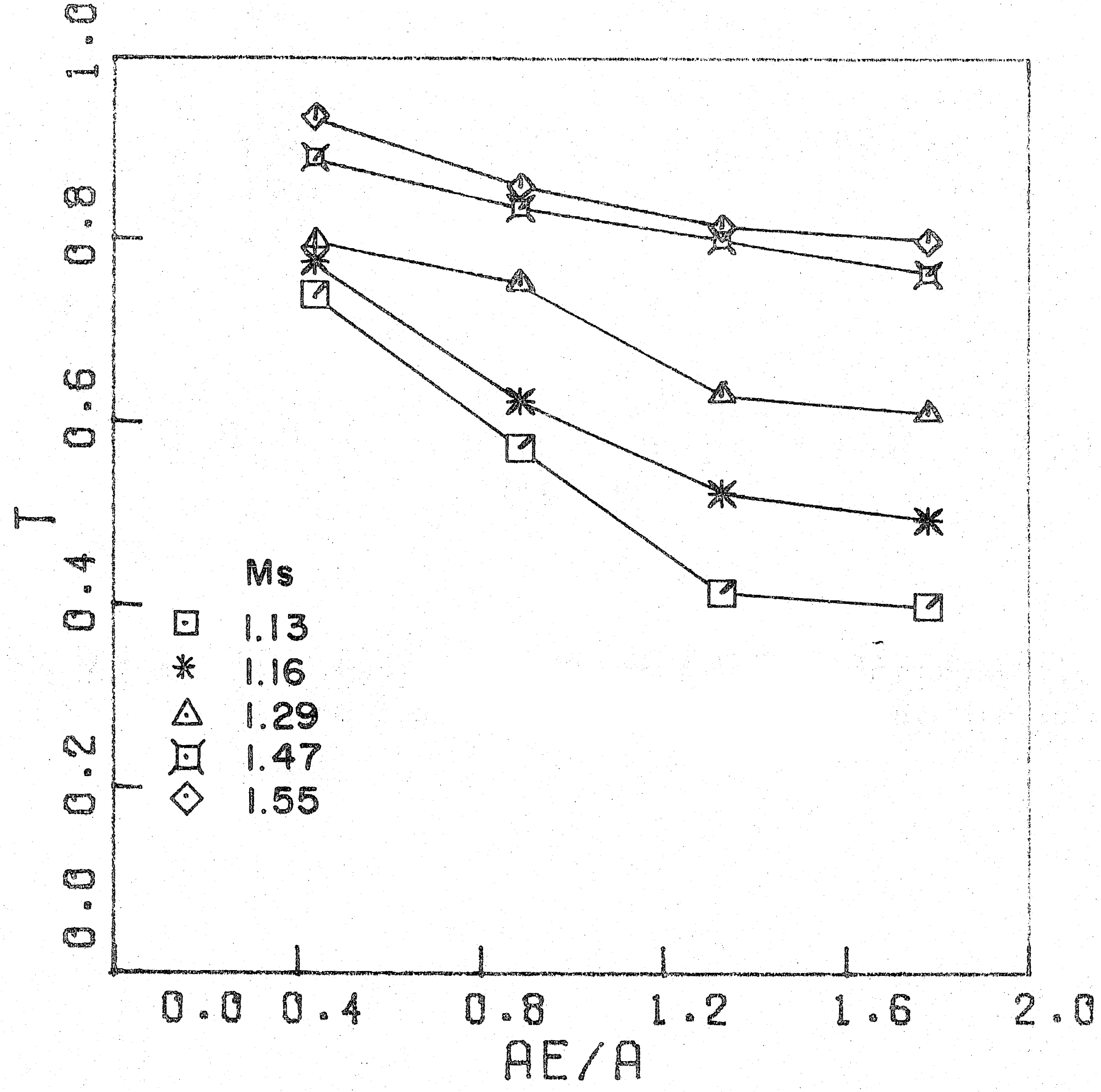

FIGURE 33a TRANSMISSION COEFFICIENTS OF PERFORATED TUBES FOR SHOCK MACH NUMBERS, SHOCK TUBE

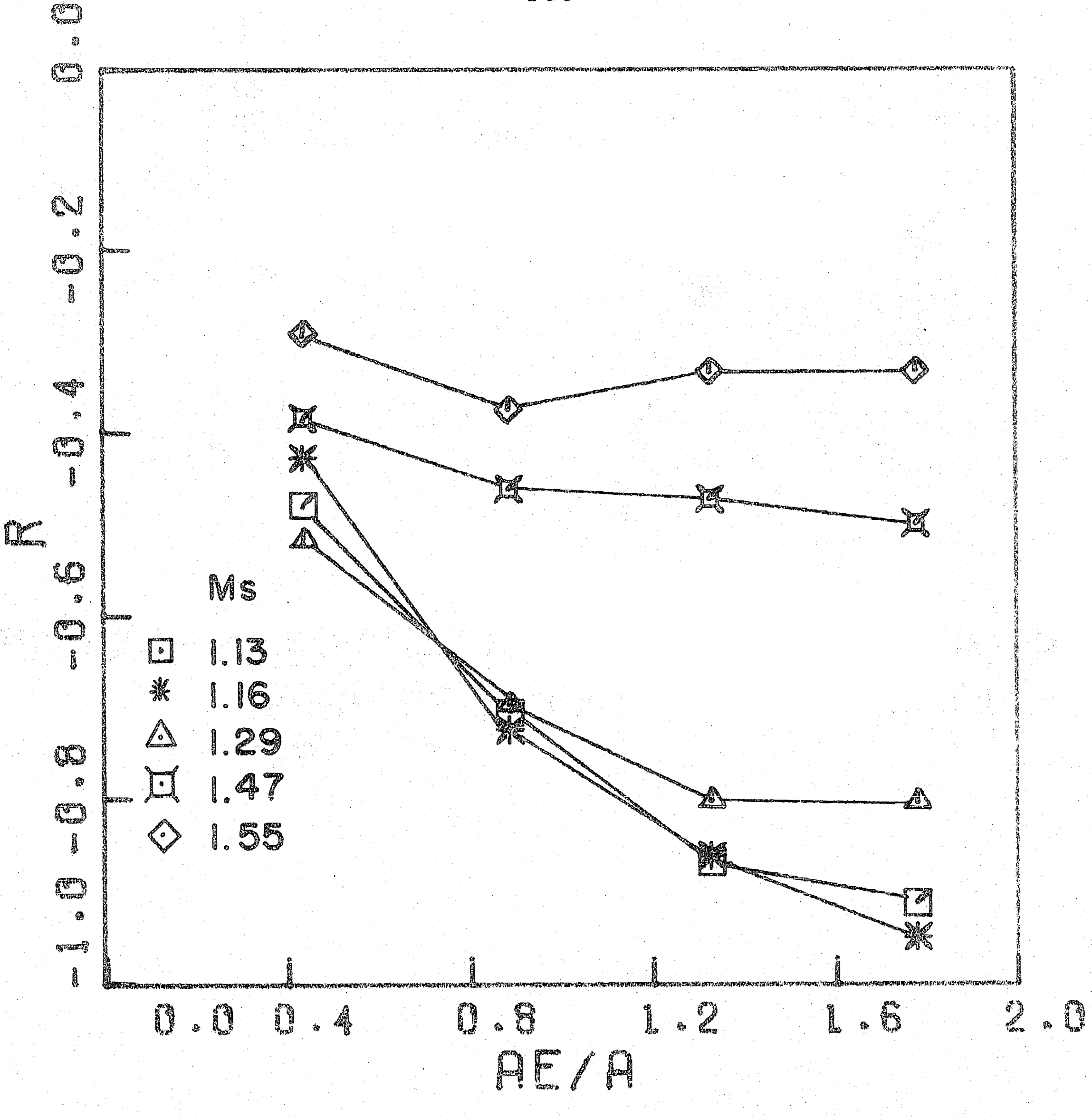

FIGURE 33b REFLECTION COEFFICIENTS OF PERFORATED TUBES FOR SHOCK MACH NUMBERS, SHOCK TUBE

of the perforations, which is the ratio of actual to ideal mass flow through the perforate, is computed as follows:*

1) The actual mass flow is $\dot{m}_a = A\,(\rho_3 U_3 - \rho_4 U_4)$, which is the defect in the mass flow between regions three and four.

2) The ideal mass flow is $\dot{m}_i = A_e \rho_e U_e$, where A_e is the total area of the perforate and the density and velocity are computed assuming the fluid expands isentropically from region three through the exit.

3) The discharge coefficient, σ, is the ratio, $\dot{m}_a / \dot{m}_i$.

The stagnation pressure is calculated in regions three and four. The stagnation pressure drop from region three to four is normalized by the stagnation pressure in region three and is presented in figure 34. At low incident shock strength, the stagnation pressure drop is almost zero; oddly enough it is a very small negative number. The stagnation pressure drop increases with incident shock strength to approximately 20% at the highest shock strength and largest area ratio (longest length of perforated tube).

The discharge coefficient is plotted in figure 35. Since they are significantly less than unity, the raw data failed to compare favorably with the theory that assumes the discharge coefficient is one. Assuming that the fluid passing through the perforation attains the calculated density and velocity, a second interpretation of the discharge coefficient can be made. The discharge coefficient represents the ratio of the cross-sectional area of each jet through the perforation to the physical area of the perforation.

---

*A simplified calculation reveals that the total mass flux into the boundary layer is negligible compared to the mass flux through the perforations.

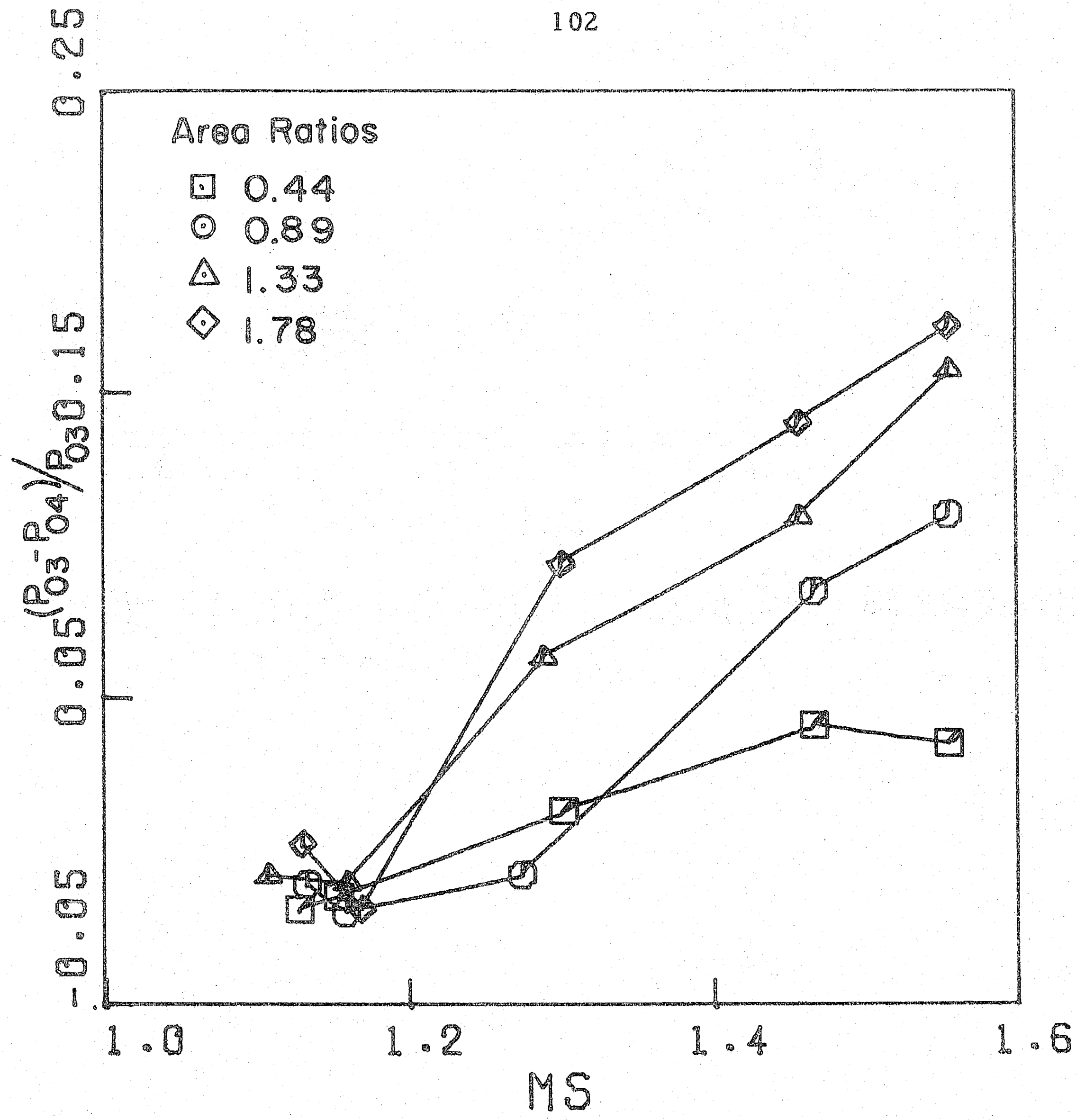

FIGURE 34 TOTAL PRESSURE LOSS ACROSS PERFORATED TUBES, SHOCK TUBE

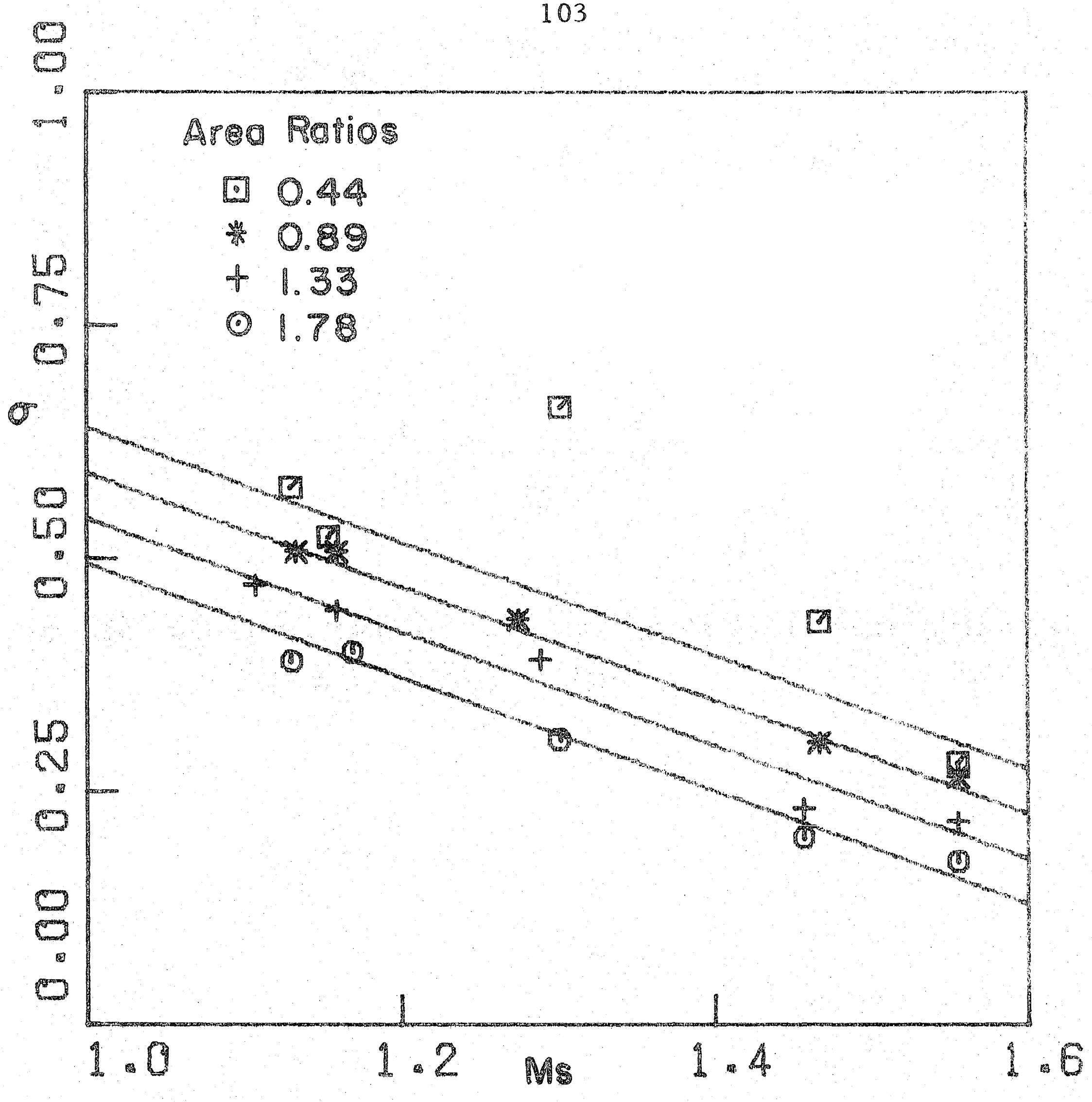

FIGURE 35 DISCHARGE COEFFICIENTS OF PERFORATED TUBES, SHOCK TUBE

Therefore, we make the rather strong assumption that the net effect of the axial flow in the tube is only to change the effective cross-sectional area of the jets.

The advantage of interpreting the discharge coefficient as an area ratio is that the theory is simple to correct. The area ratio is replaced by the product of the discharge coefficient with the area ratio. The functional dependence of the discharge coefficient is obtained by a numerical fit of the data presented in figure 35. The empirical relation, $\sigma\,(A_e/A,\ M_s) = .687 - .109\,A_e/A - .609\,(M_s - 1)$, agrees with a large portion of the data.

The area ratio used in the theories of Section 3.1 is corrected with the empirical relation discussed above. The corrected theory is checked by comparison with data in figures 36 through 40.

The first order theory, eqn. 22, agrees with the transmission coefficient data, except for $M_s = 1.16$, where observations are slightly underpredicted. However, the reflection coefficient is not predicted. Since only the transmission coefficient is confirmed by the data, the solution must be taken somewhat lightly. In particular, since, for low incident shock strength, the solution of the complete set of second order equations predicts both the transmission and reflection coefficient quite well, we must assume that all the second order terms are important. (Even though the reflection coefficient is not predicted by eqn. 22, it does provide a good estimate of the transmission coefficient, which is useful in computing the radiated noise (Section 5.2).)

The numerical solutions could not be obtained for shock Mach numbers 1.47 and 1.55, and the data processing programs revealed

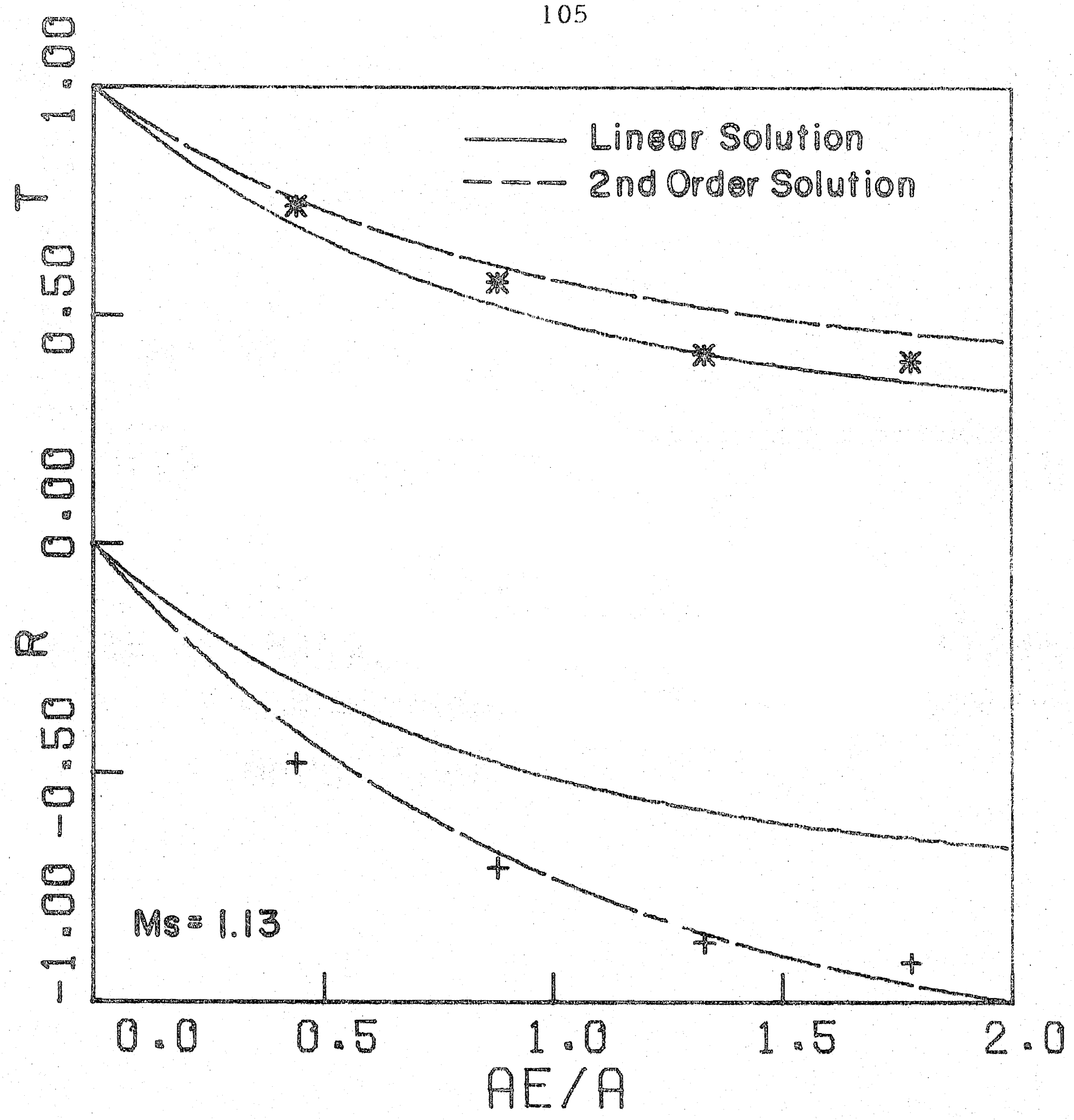

FIGURE 36 TRANSMISSION AND REFLECTION COEFFICIENTS FOR PERFORATED TUBES,DATA AND THEORY, SHOCK TUBE

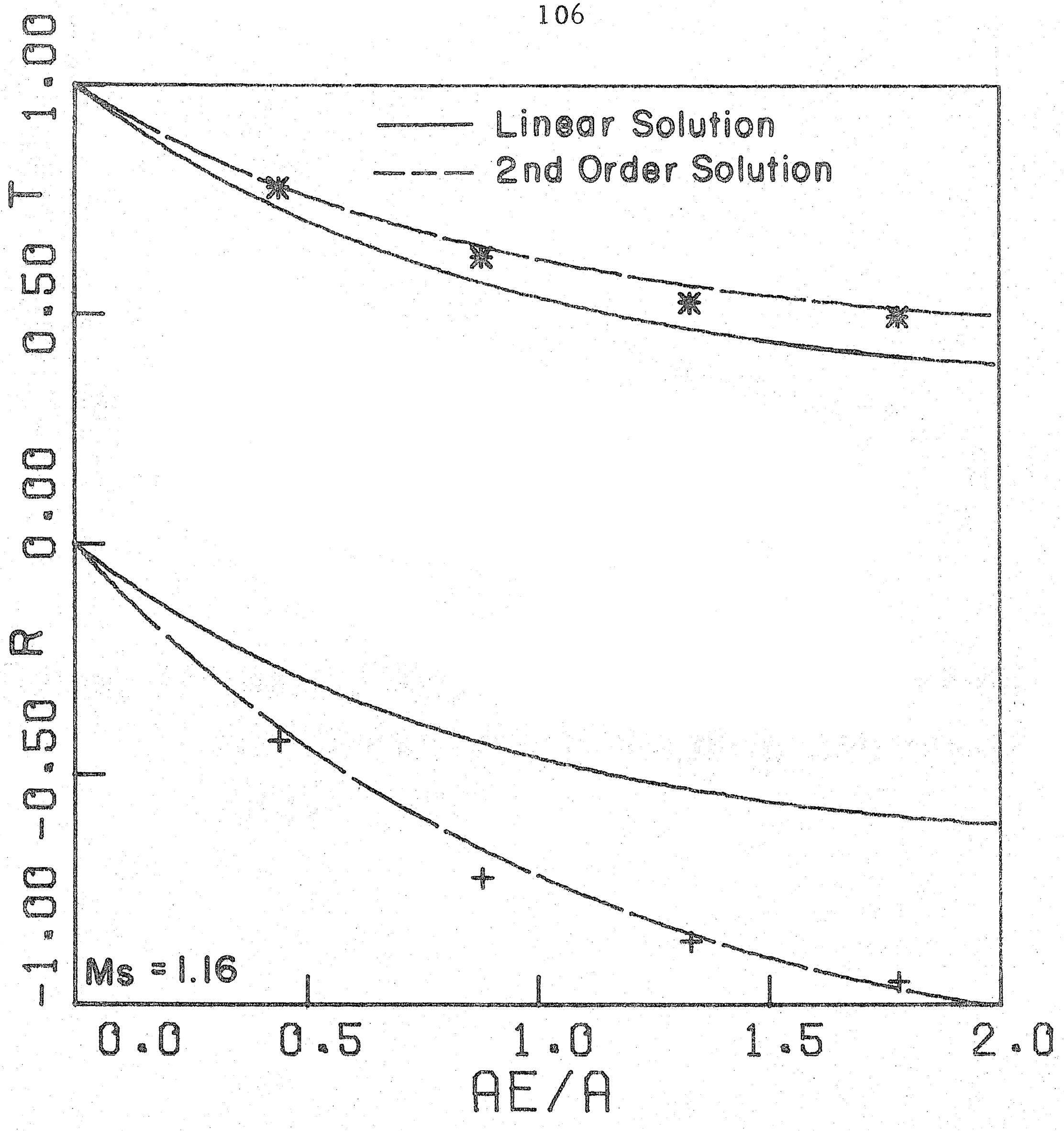

FIGURE 37 TRANSMISSION AND REFLECTION COEFFICIENTS FOR PERFORATED TUBES, DATA AND THEORY, SHOCK TUBE

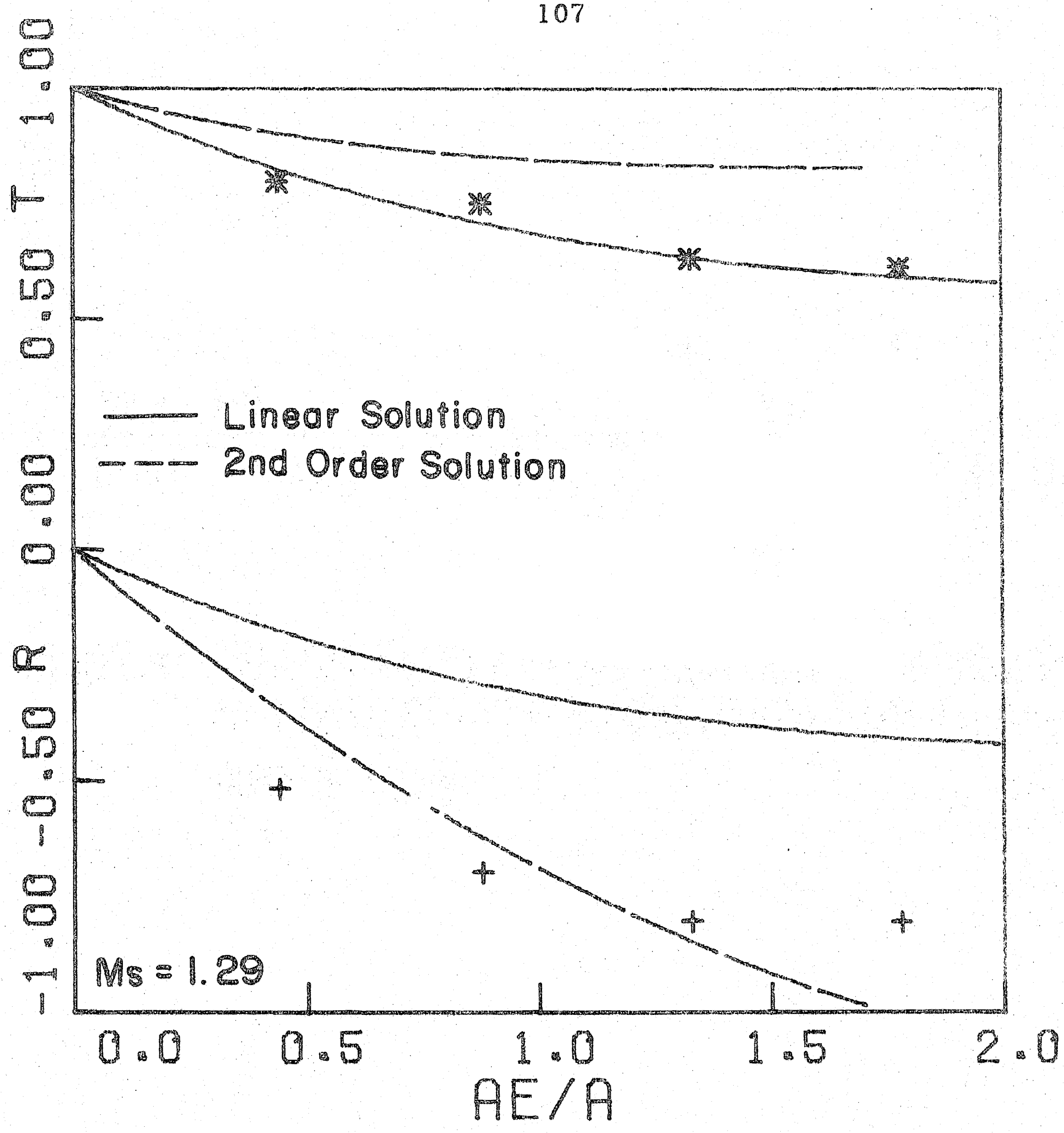

FIGURE 38 TRANSMISSION AND REFLECTION COEFFICIENTS FOR PERFORATED TUBES, DATA AND THEORY, SHOCK TUBE

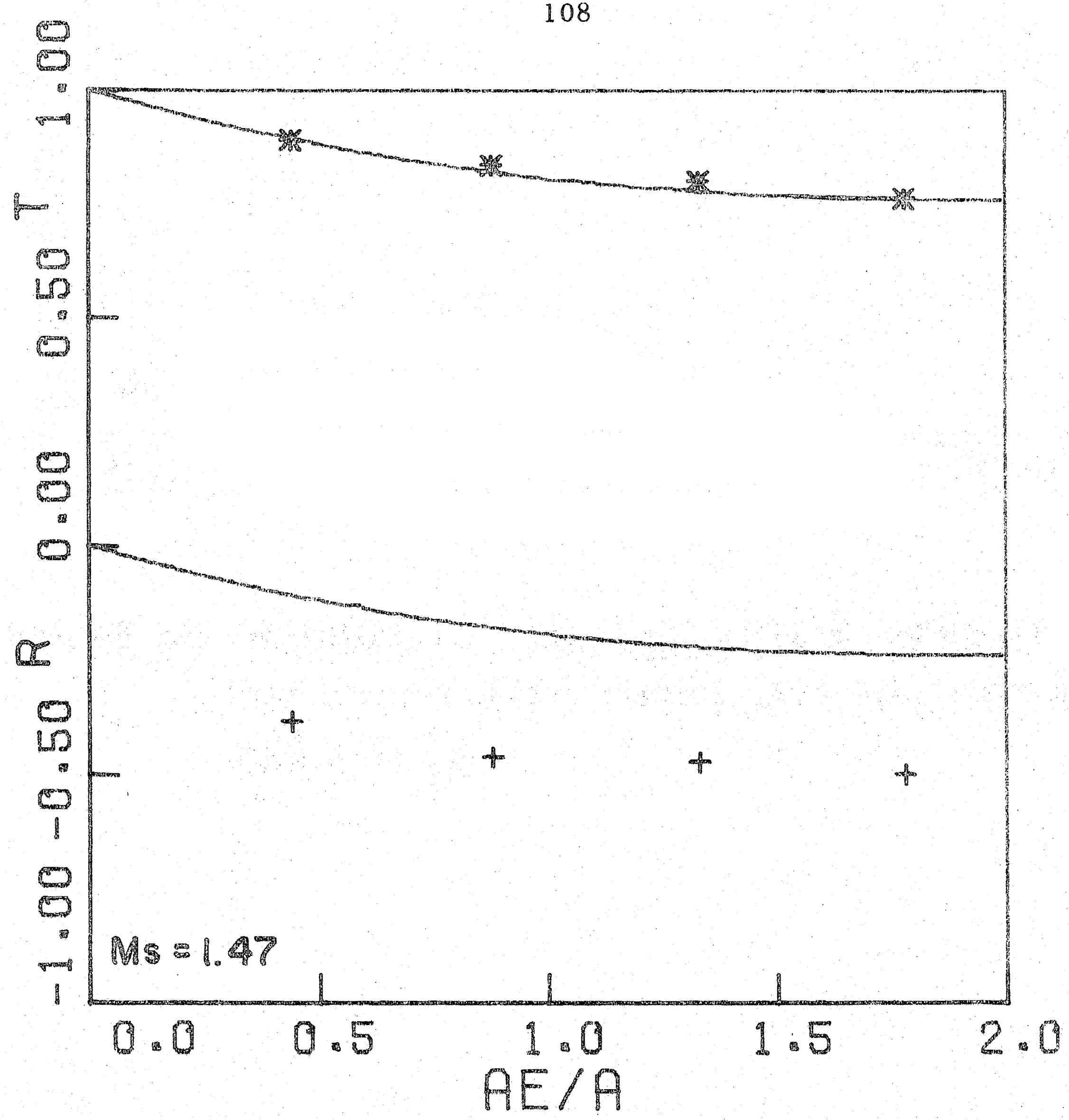

FIGURE 39 TRANSMISSION AND REFLECTION COEFFICIENTS FOR PERFORATED TUBES,DATA AND THEORY, SHOCK TUBE

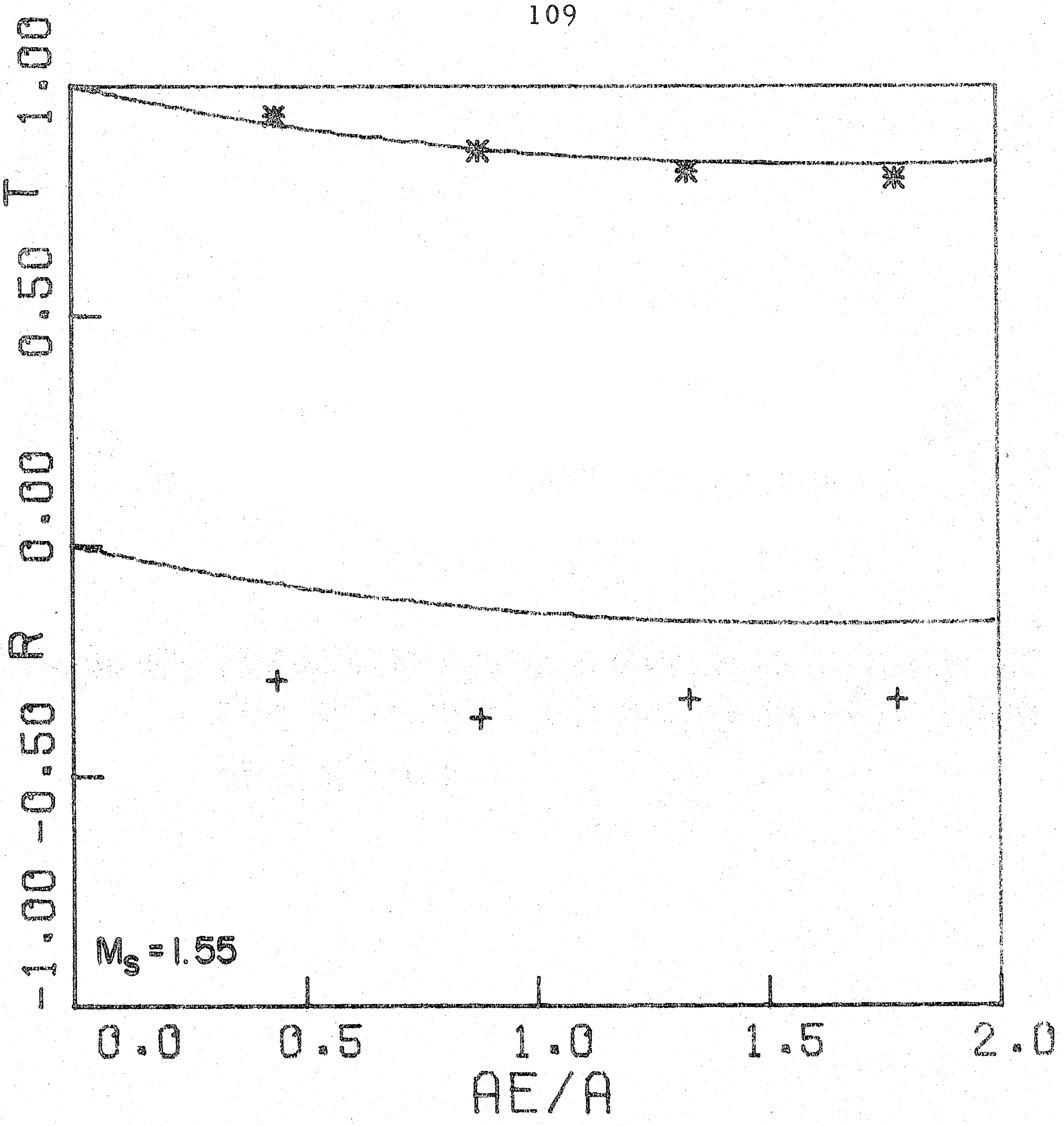

FIGURE 40 TRANSMISSION AND REFLECTION COEFFICIENTS FOR PERFORATED TUBES, DATA AND THEORY, SHOCK TUBE

that the flows in region three and through the perforations were near sonic ($M_s = 1.47$, $M_3 = 0.88$ and $M_e = 1.13$; $M_s = 1.55$, $M_3 = 0.92$ and $M_e = 1.24$). These equations are valid expansion for flows with small compressibility effects, as the equations are second order in the flow Mach number. Clearly these expansions are not sufficient if the flow is choked, which may cause the numerical solution to diverge for these two cases.

4.1.3 The Effect of an Initial Velocity in the Test Section

The effect of an initial velocity in front of the shock was studied in the resonance tube facility, as described in Section 2.1.1. The procedure used in the repetitive pulse experiments was described in Section 2.3.1. At a resonant frequency of 38.4 Hz, the test shock Mach number varied from 1.11 to 1.16, depending on the muffler system. Perforated tubes were used with and without expansion chamber enclosures. The perforate area ratio was varied from 0.22 to 4.0, and expansion chambers A, B, and C were used as enclosures. The incident and reflected waves were observed at location U, the transmitted waves were observed at location D1, and for finite enclosures, the radiated waves were observed at location F. The results from the infinite enclosure experiments are used to discuss the effects of an initial velocity. The additional effect of a finite enclosure is discussed in the next section.

Since the discharge coefficient of the perforations is controlled by the axial velocity in the tube, the predominant effect of an initial velocity in the tube is to change the discharge coefficient. If, after the waves have interacted with the perforations, the resultant axial velocity is small compared to the velocity through the perforations, the jets point in the radial direction. When the axial velocity is increased, the jets tilt from the radial direction toward the axis of the tube, thus decreasing the discharge coefficient.

The pressure wave forms for one fifth of a cycle of the periodic motion, in the case of infinite enclosures, are presented in figure 41. The traces in the top row are observed from location U; the traces in the bottom row are observed from location D1 (Fig. 12). Three experiments are presented, one in each column, corresponding to perforate area ratios of 0.44, 0.89, and 1.78.

The reflected wave from the perforated section of tube is an expansion wave whose amplitude increases with increasing area ratio. The transmitted wave is a shock for small area ratios; while for larger area ratios the sharp expansion and smooth compression are observed behind the shock front. The amplitude of the transmitted shock decreases with increasing area ratio. It is noted that the amplitude of the transmitted shock front is greater than the gradual compression; whereas in the single pulse experiments, the amplitude of the shock front was equal to or less than the final compression. Thus, wave forms in both the single and repetitive pulse experiments are similar, but quantitative differences do exist.

As before, the amplitude of the reflected and transmitted waves are normalized by the amplitude of the incident shock. In the case of the more complex transmitted wave forms, the amplitude is taken to be the pressure after the gradual compression. Figure 42 presents a comparison of the repetitive pulse data for infinite enclosures with

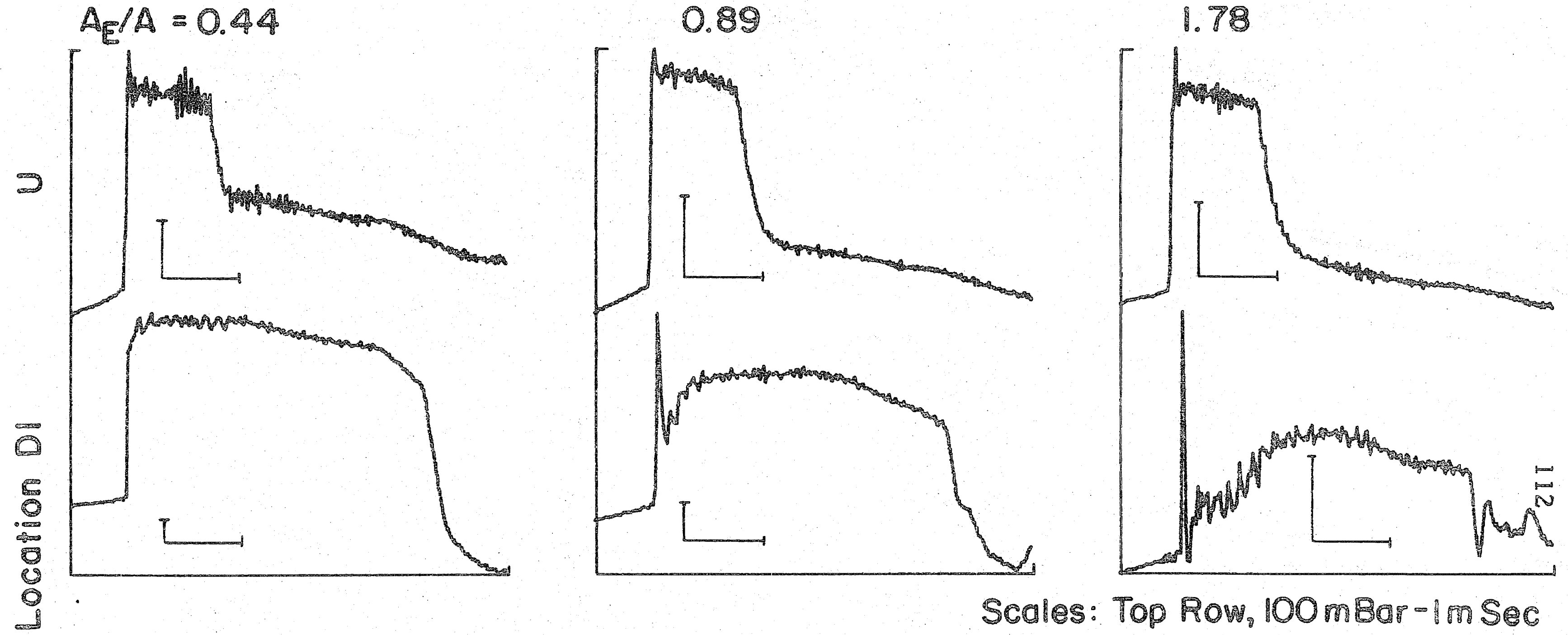

Scales: Top Row, 100 mBar - 1 m Sec
Bottom Row, 20 mBar - 1 m Sec

FIGURE 41 PRESSURE HISTORIES OF SHOCK PROPAGATION PAST PERFORATED TUBES WITHOUT ENCLOSURES, RESONANCE TUBE

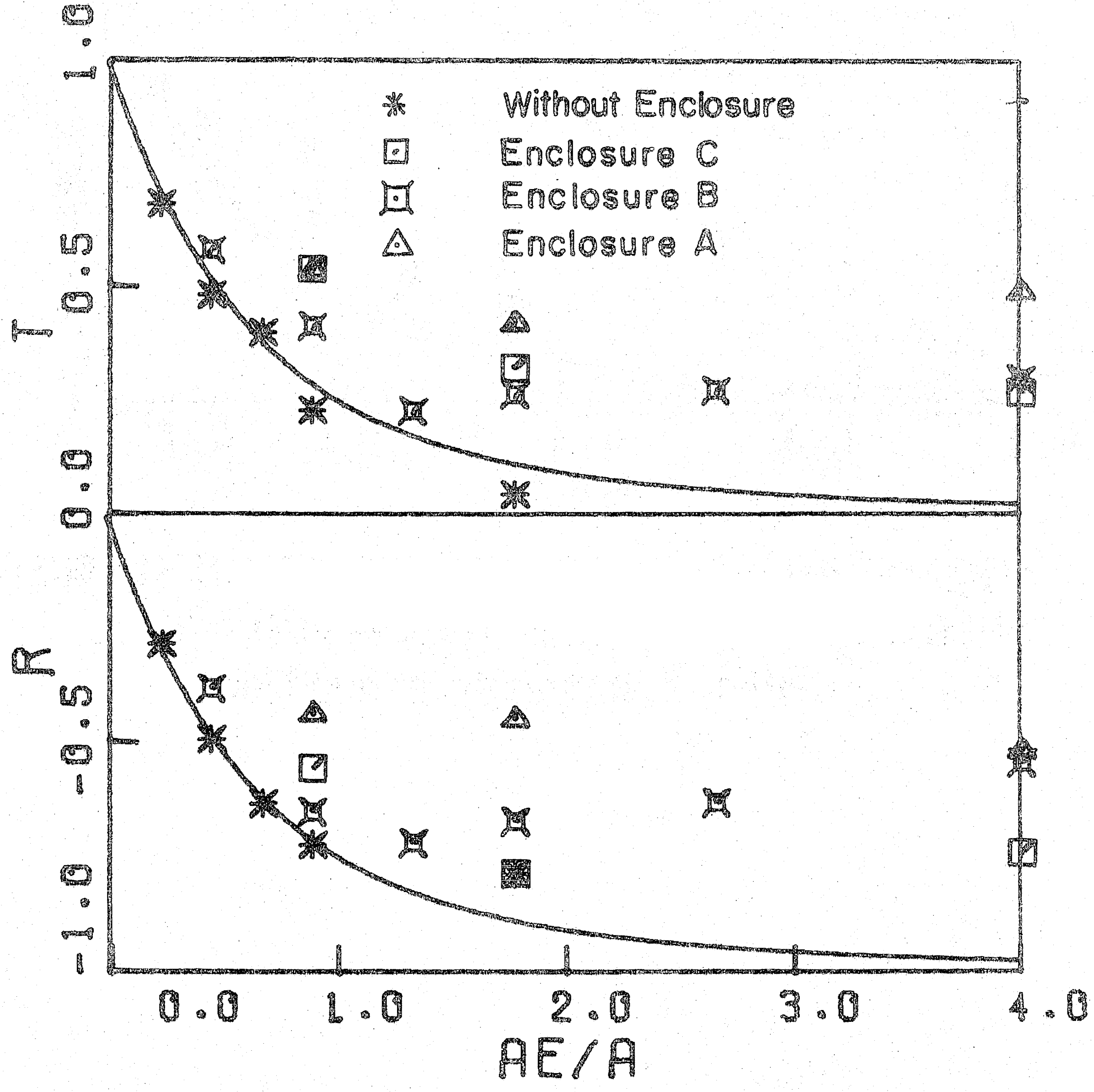

FIGURE 42 TRANSMISSION AND REFLECTION COEFFICIENTS OF PERFORATED TUBES, WITH AND WITHOUT ENCLOSURES, RESONANCE TUBE

the first-order theory.

Surprisingly, the data are in agreement with the theory; this was not the case with the single-pulse data. The conclusion is that the discharge coefficients are equal to unity for repetitive-pulse excitation, though they were less than unity for the single-pulse excitation.

To investigate this difference, the unknown initial velocity, U_1, in the repetitive-pulse experiments was estimated to see if it might explain the unusually high values of the discharge coefficients. To approximate the initial velocity, a constraint was employed; namely, that the total pressure in regions three and four be equal, as was the case in the single-pulse experiments for weak incident shocks.

The total pressure is the sum of the static and dynamic pressures. The static pressure is measured directly, and the velocity is the sum of wave-induced velocities and the unknown velocity, U_1. The initial velocity, U_1, is computed by equating total pressures in regions three and four (Eqn. C. 1). The velocities, U_1 - U_4, and the discharge coefficient for the resonance tube data are calculated in Appendix C. It turns out that for all runs, the initial velocity is directed into the resonance tube and is slightly higher than the change in velocity induced by the incident wave. The fluid in region three has a small velocity toward the perforate, as does the velocity in region four. The axial velocity of the fluid near the perforated section must, therefore, be very small, so the jets from the perforations are directed normal to the tube axis. This explains the large value of the observed discharge coefficients.

As a check, the initial velocity, U_1, in a solid tube (no perforations) was calculated another way. The time interval between shock arrival at locations U and D1 is measured, as shown in figure 43. With the distance between locations U and D1, the absolute shock speed is known. Using the ambient speed of sound and the shock Mach number calculated from the pressure jump across the shock, the relative shock speed is known. The difference in these speeds is the mean initial velocity between locations U and D1, also given in Appendix C. This computation confirms the direction and approximate amplitude of the initial velocity obtained with the previously discussed method.

4.1.4 Enclosure Effects

Two important consequences of enclosing the perforate section in an expansion chamber of finite volume are (1) the amplitude of the initial reflected and transmitted waves can be altered, and (2) waves driven into the enclosure reflect from its boundaries and re-enter the perforated section to be transmitted upstream and downstream in the main tube. Even though the quantitative effect of enclosures is not understood, one possible model of the process is shown in figure 44, where a plane wave is driven into the enclosure and reflects back and forth causing a compressive disturbance in the main tube each time it passes the perforated section. Figures 45, 46, and 47 present pressure wave forms for experiments where the perforate area ratios were 0.89, 1.78, and 4.00, respectively. In each figure, expansion chambers A, B, and C were used for enclosures.

In figures 37 and 38, the odd numbered waves in the downstream

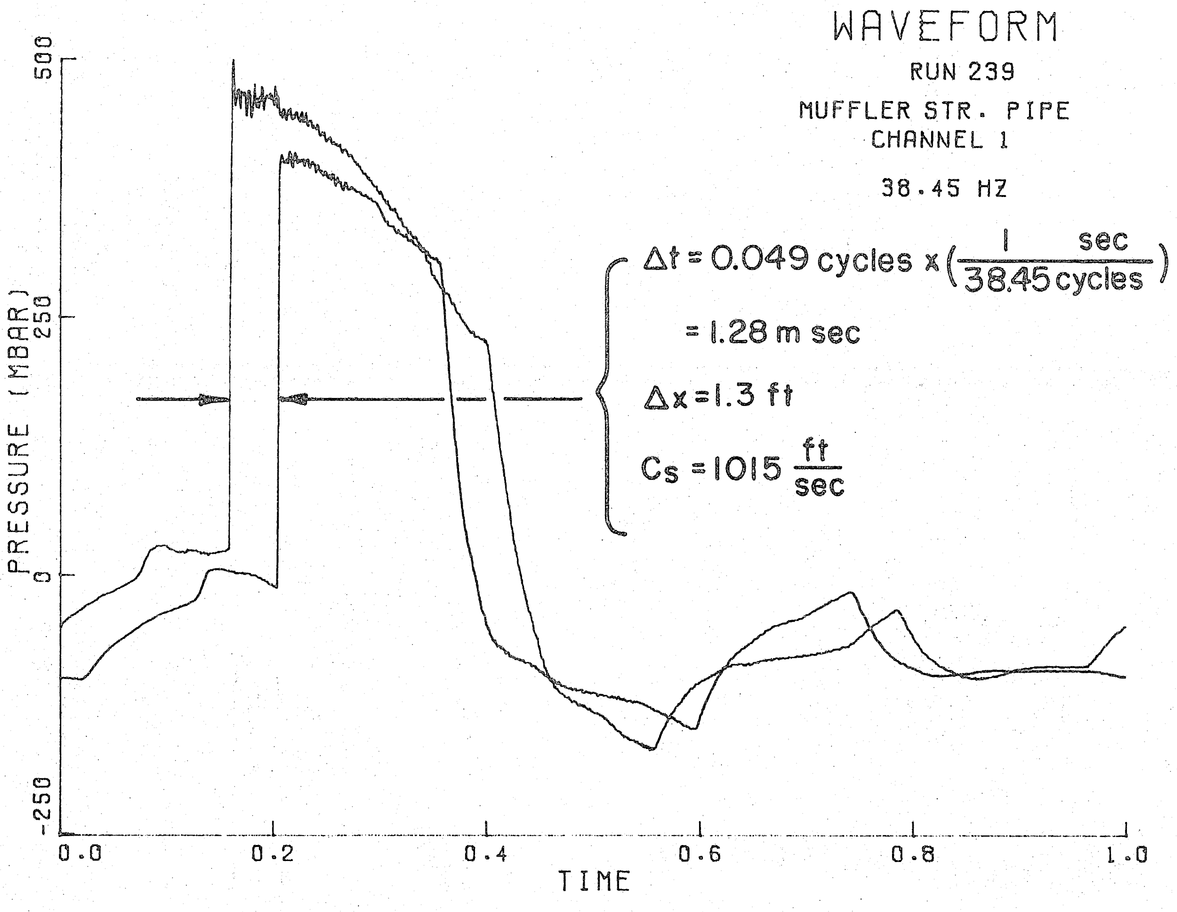

FIGURE 43 INITIAL TEST SECTION VELOCITY, RESONANCE TUBE

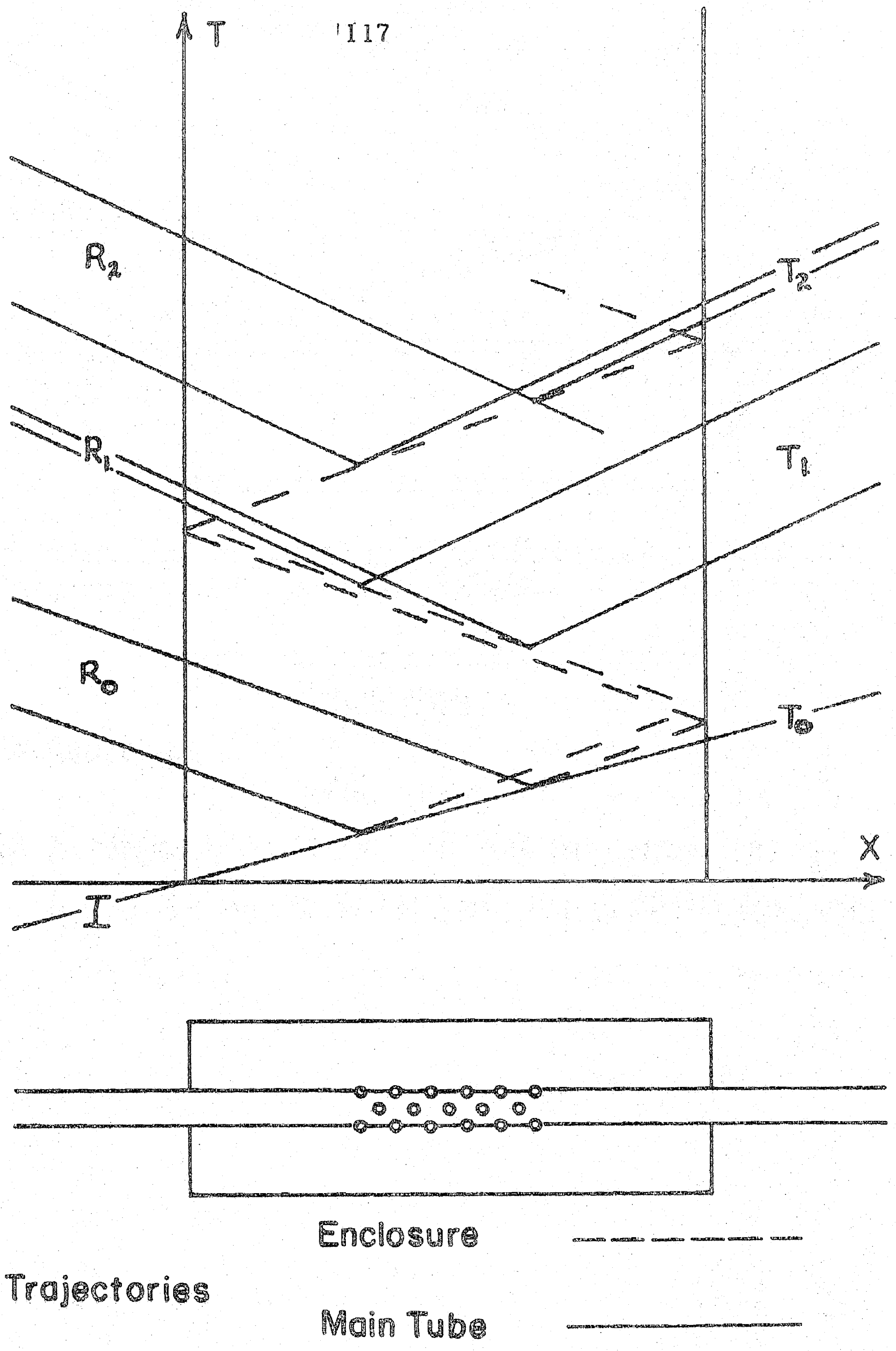

FIGURE 44 A PROPOSED MODEL OF THE INTERACTION OF A SHOCK WAVE WITH ENCLOSED PERFORATIONS

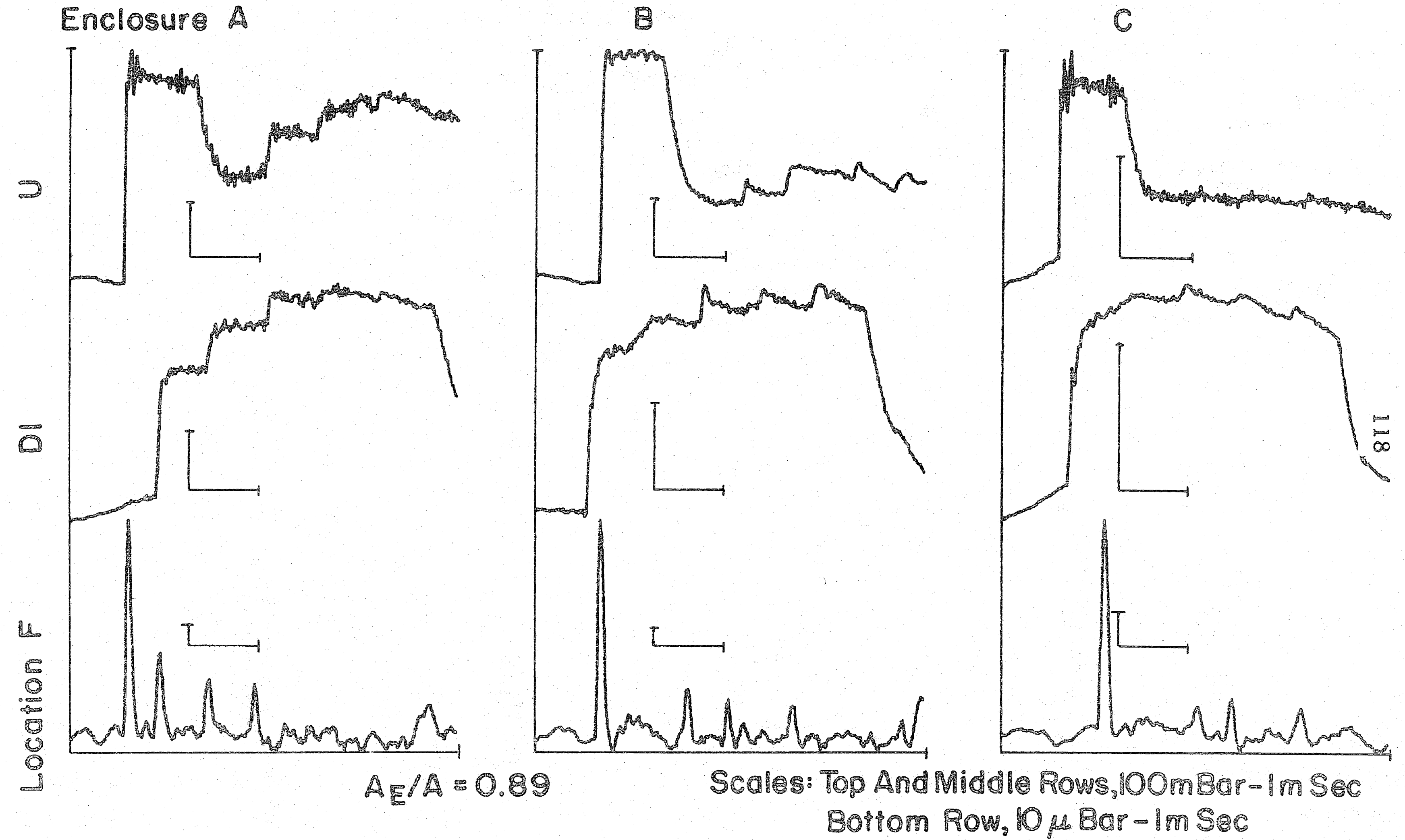

FIGURE 45 PRESSURE HISTORIES OF SHOCK PROPAGATION PAST PERFORATED TUBES, RESONANCE TUBE

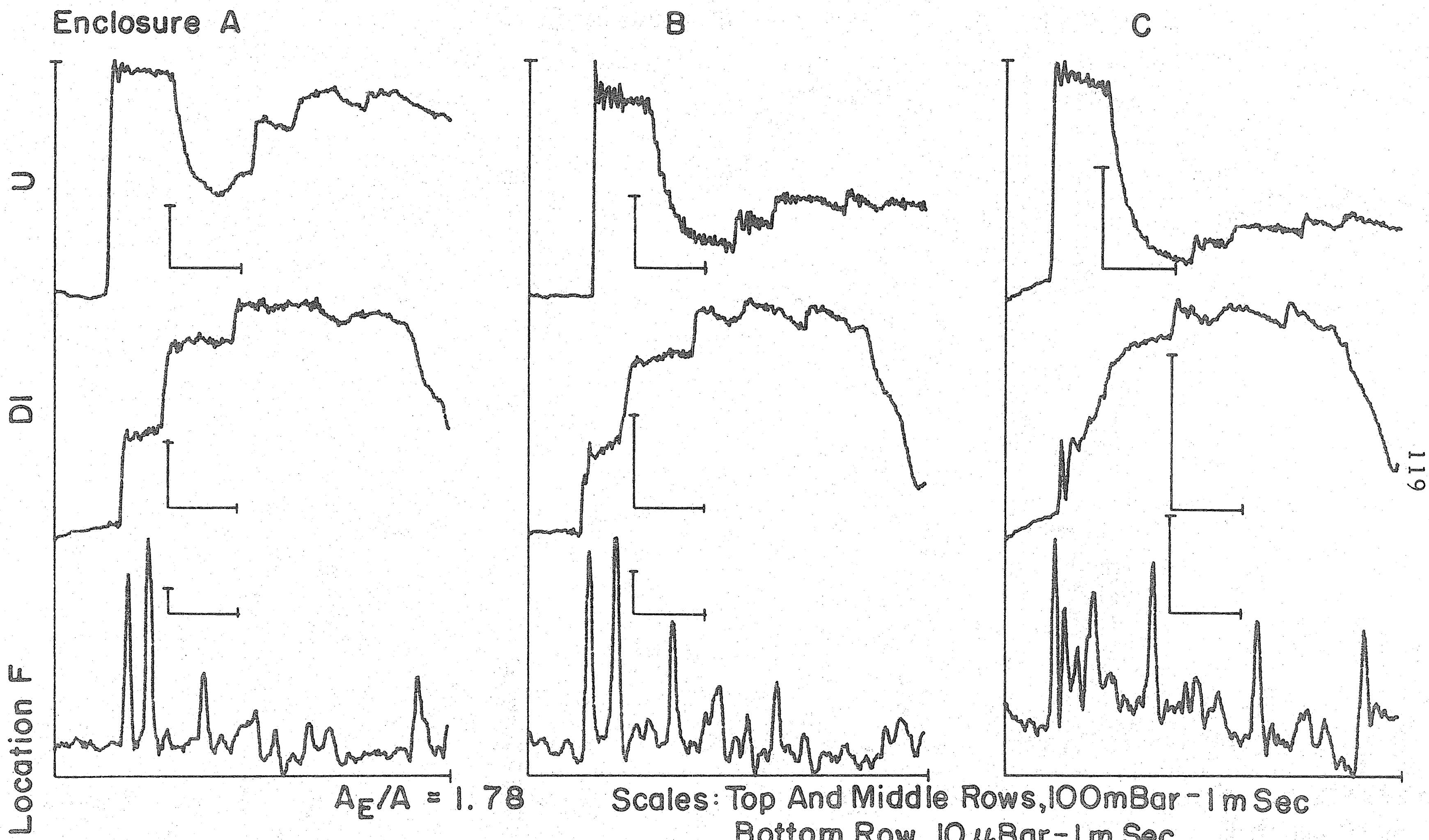

Scales: Top And Middle Rows, 100 mBar - 1 m Sec
Bottom Row, 10 μBar - 1 m Sec

FIGURE 46 PRESSURE HISTORIES OF SHOCK PROPAGATION PAST PERFORATED TUBES, RESONANCE TUBE

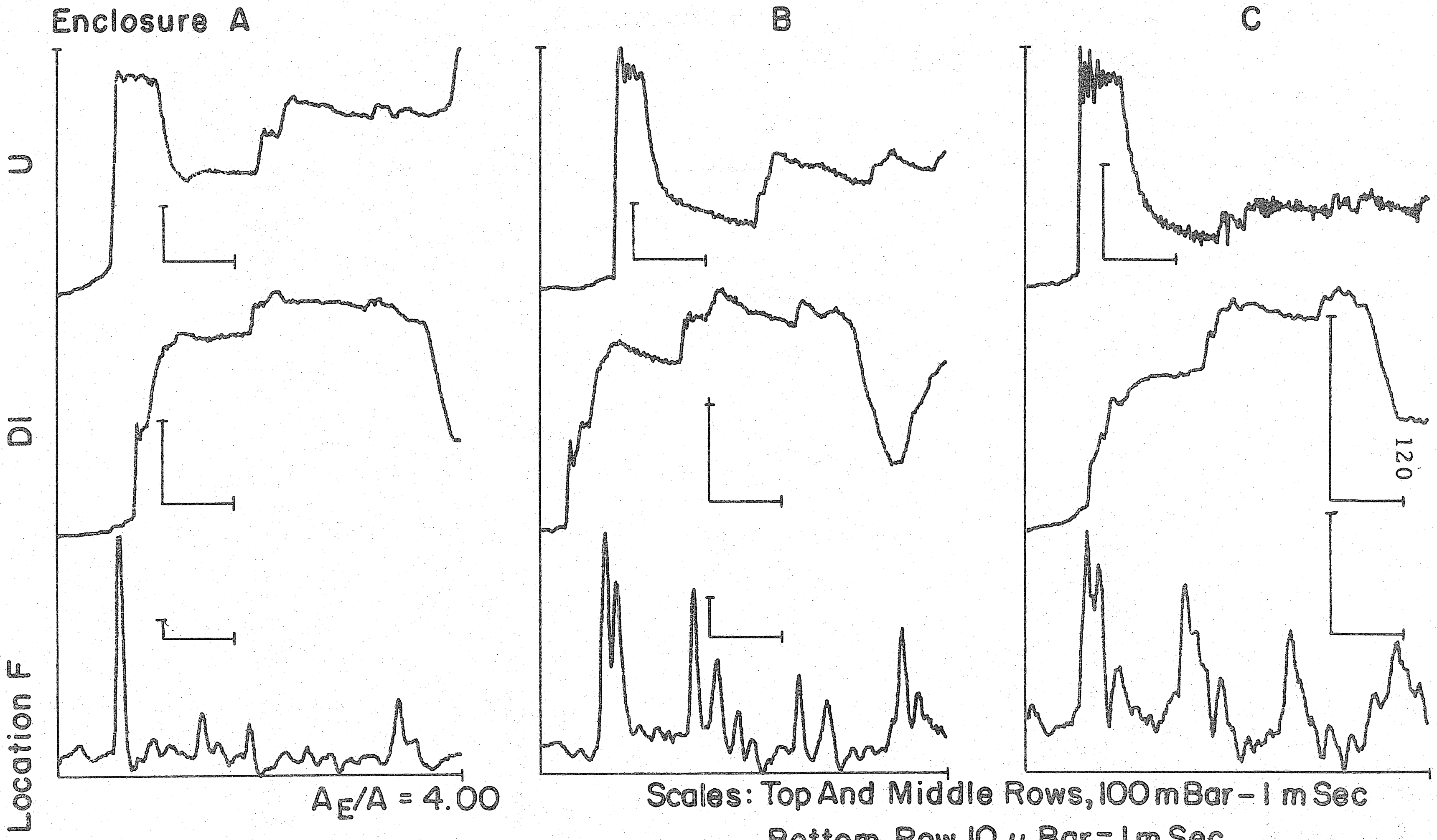

Scales: Top And Middle Rows, 100 m Bar - 1 m Sec

Bottom Row, 10 μ Bar - 1 m Sec

FIGURE 47 PRESSURE HISTORIES OF SHOCK PROPAGATION PAST PERFORATED TUBES, RESONANCE TUBE

tube are smoother compressions than the even numbered waves (the numbering scheme is defined in figure 44), which appear to be shocks. Thus, when the wave in the enclosure propagates past the perforated section in the downstream direction, the disturbance observed downstream in the main tube is steeper than the disturbance observed upstream. This result is consistent with the model proposed above.

In figure 45, the largest enclosure, expansion chamber C, has little affect on the wave form in that multiple reflected and transmitted waves are negligible. The effect is significant for smaller enclosures, as multiple reflected and transmitted waves are observed.

Increasing the perforate area ratio from 0.89 to 1.78 reduces the amplitude of the first transmitted wave, while the subsequent waves are stronger, as shown in figure 46. Enclosures A, B, and C all affect the wave form, as additional disturbances are observed at locations U and D1. At location D1, the odd numbered waves are observed to be smoother compressions than the even numbered waves.

In figure 47, which presents the largest perforate area ratio cases, all of the enclosures affect the wave forms. Increasing the perforate area ratio from 1.78 to 4.00 does not affect the amplitude of the primary disturbance. This was also the case with subsequent disturbances, which have a different timing since the perforate section has been lengthened.

The effect of enclosures on the amplitudes of the first reflected and transmitted waves is shown in figure 42. The effect that enclosures have on the transmission coefficient is not as clear as the effect they have on the resultant sound radiation (Section 5.2.2). In short, enclosures have only a small effect for small amounts of perforate area ratio. Specifically, for infinite enclosures, the transmission coefficient goes to zero at large perforate area ratios; however, the limiting value tends to unity for smaller enclosures.

The transmitted wave data for perforated tubes without enclosure and with enclosures A and B are consistent with this qualitative description. The data for enclosure C are not, as the transmission coefficients for two cases, $Ae/A = 0.89$ and 1.78, are greater than the equivalent data for smaller enclosures. This observation is not understood. For infinite enclosures, the reflection coefficient goes to (-1) at large perforate area ratios; however, the limiting value tends toward zero for smaller enclosures.

4.2 Expansion Chambers

The interaction of a shock wave with an expansion chamber muffler system is discussed in this section. The basic function of the conventional expansion chamber is to break up the incident shock into an infinite series of weaker pulses. The incident shock is weakened as it passes into the expansion chamber. As the weakened shock reflects between the downstream and upstream junctions, an infinite series of waves is transmitted into the inlet and outlet pipes. The waves transmitted into the tailpipe are compressions and have a total amplitude equal to that of the incident shock. An expansion wave is reflected into the inlet pipe when the shock initially enters the expansion chamber. An infinite series of compressions follows the expansion wave in the inlet pipe. The total amplitude of the compression waves is equal to the negative of the expansion wave.

The basic wave interaction processes are discussed in the first section, including the effects of incident shock strength, chamber area ratio, chamber length-to-diameter ratio. When the chamber length-to-diameter ratio is small the waves diffracted off the shock as it passes into the chamber do not have sufficient time or distance to coalesce with the weakened shock before it reaches the outlet. In this case, the diffracted waves change the form of the transmitted waves.

The amplitude of the reflected and transmitted waves are compared with the theory in Section 3. The effect of incident shock strength and chamber area ratio are discussed. Results from the resonance tube experiments are used to illustrate the effects of an inflow ahead of the shock.

4.2.1 Wave Forms

Expansion chambers A, B, and C were tested with and without inlets or outlets extended. In the single-pulse experiments, the incident shock Mach numbers were 1.07, 1.17, and 1.26. The incident and reflected waves were observed at location U1. The transmitted waves were observed in the long tailpipe at locations D1 and D3. Transducer location D3 was positioned 30 diameters from the downstream end of the expansion chamber, with the intent of observing a fully developed wave. This long tailpipe was used only in the single-pulse experiments. The radiated wave form was observed at location F in a second experiment with the standard length tailpipe, and the standard tailpipe was used exclusively in the repetitive pulse experiments. Typical pressure wave forms are presented in figures 48, 49,

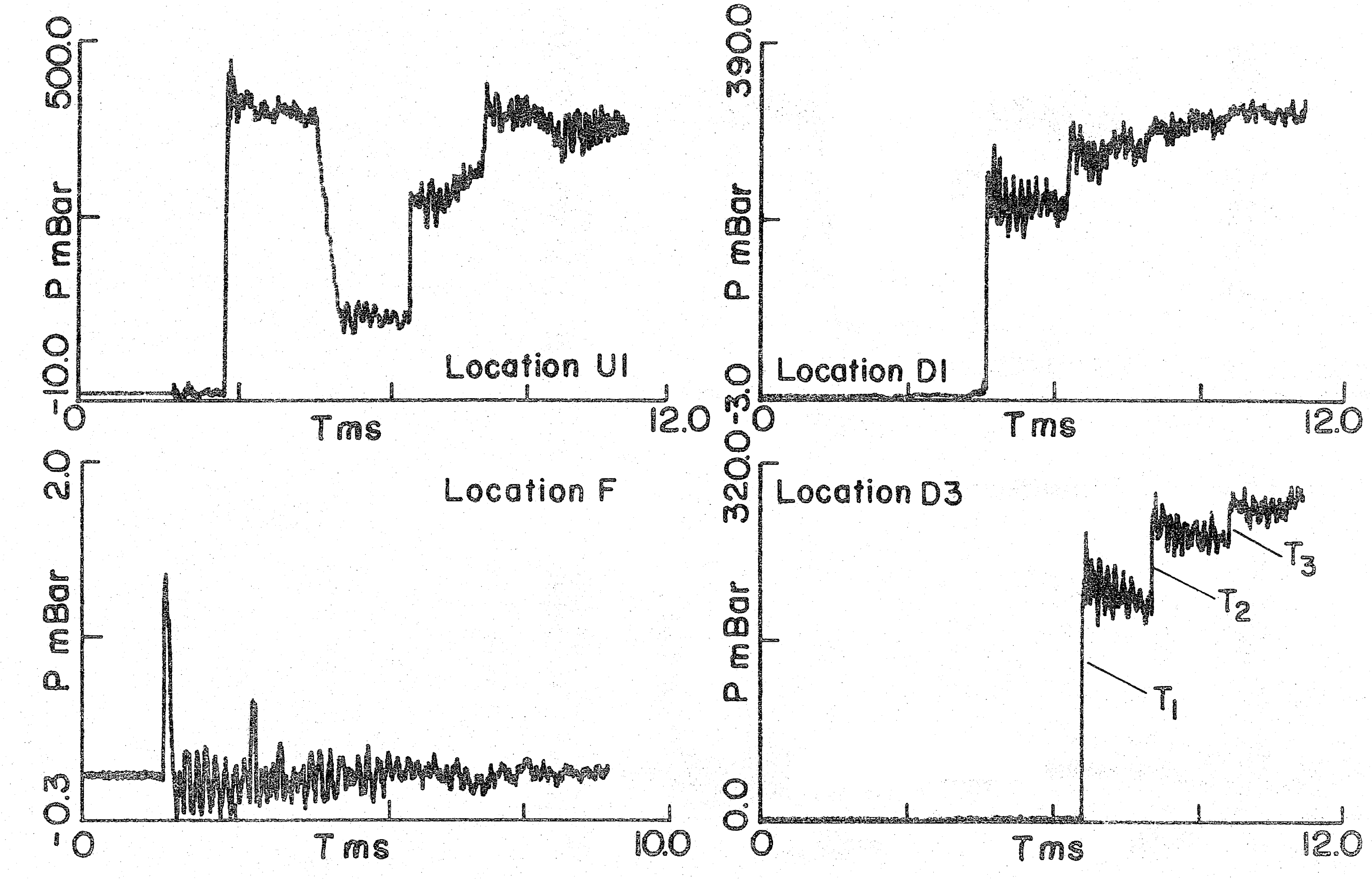

FIGURE 48 PRESSURE HISTORIES OF SHOCK PROPAGATION THROUGH EXPANSION CHAMBER, B. Ms = 1.17, SHOCK TUBE

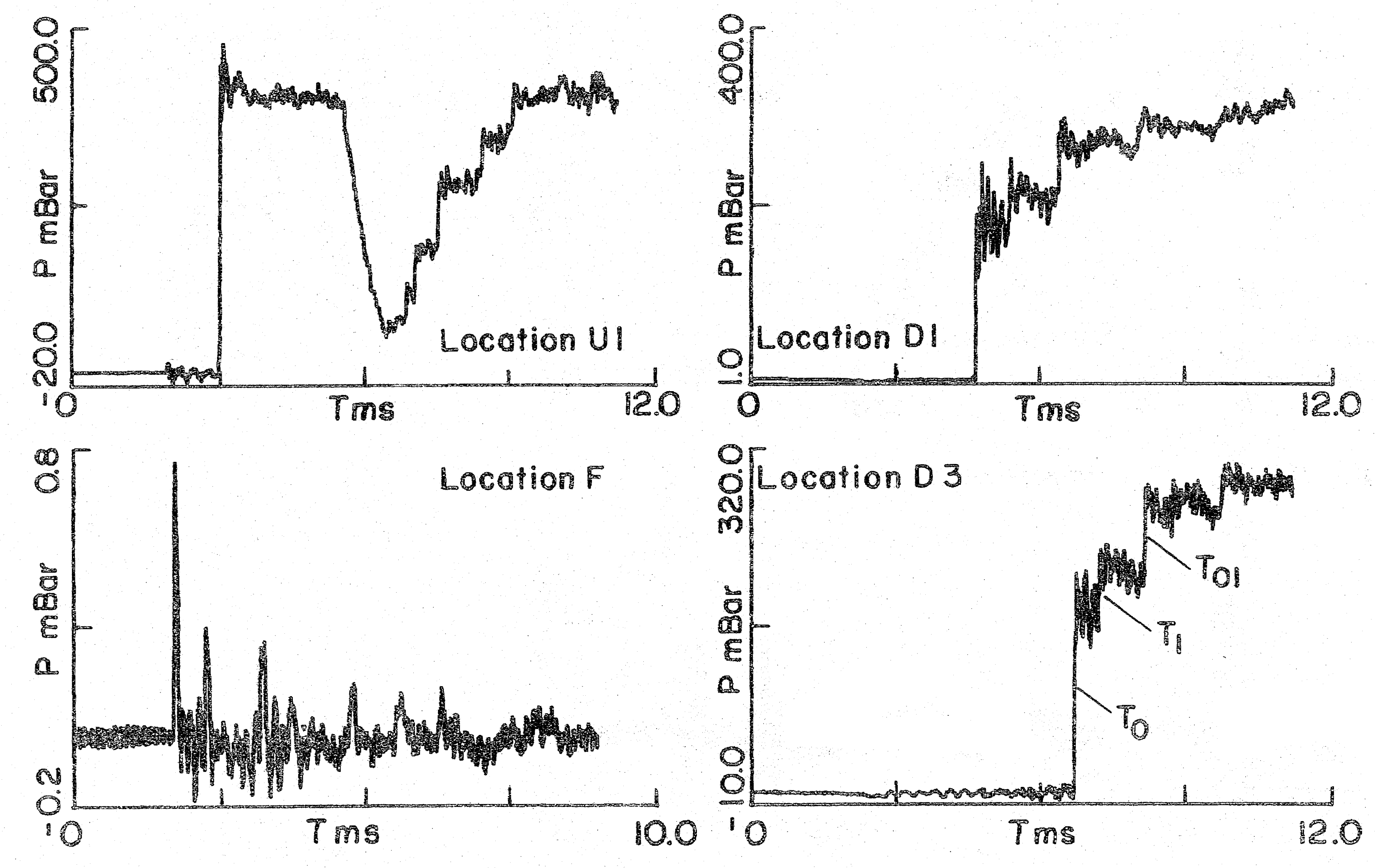

FIGURE 49 PRESSURE HISTORIES OF SHOCK PROPAGATION THROUGH EXPANSION CHAMBER, B, WITH INLET EXTENSION. $M_s = 1.16$, SHOCK TUBE

and 50 (pressure wave forms for location F will be discussed in Section 5).

Figure 48 presents the pressure wave forms for the case of the standard expansion chamber B. An X-T diagram of the shock-wave interaction is shown in figure 23.

The pressure between the transmitted shocks, T_1, T_2, etc., is smooth and nearly constant for small area ratios. For larger area ratios, the pressure fluctuations between the transmitted shocks are increased (Fig. 51). These fluctuations are presumably caused by diffracted waves of the incident shock. For chambers with large length to diameter ratios, aspect ratio, the disturbance at the downstream junction is merely a shock. For smaller aspect ratios, the diffracted waves have not coalesced with the leading disturbance when it reaches the downstream junction, causing the rapid fluctuations observed behind the first shock.

The amplitude of the incident shock does not affect the relative amplitude of the first shock to the diffracted waves. For the case of $M_s = 1.07$ and chamber C, shocks are formed in the compressive portions of the diffracted waves, as can be seen at location D3. The shocks in the rather sawtooth-like wave form have an approximate spacing of 230 μsec and shock strength of $M_s = 1.01$. The spacing of the shocks in the diffracted wave form is close to the period of the first radial mode of chamber C ($f = \frac{3.83}{2\pi} (\frac{2a}{d}) = 3.68$ kHz or $\Delta t = 272$ μsec; Davis, 1954). For the largest incident shock strength, $M_s = 1.26$, the spacing between the shocks in the diffracted wave is 235 μsec, and their strength is $M_s = 1.035$. The ratio of the amplitude

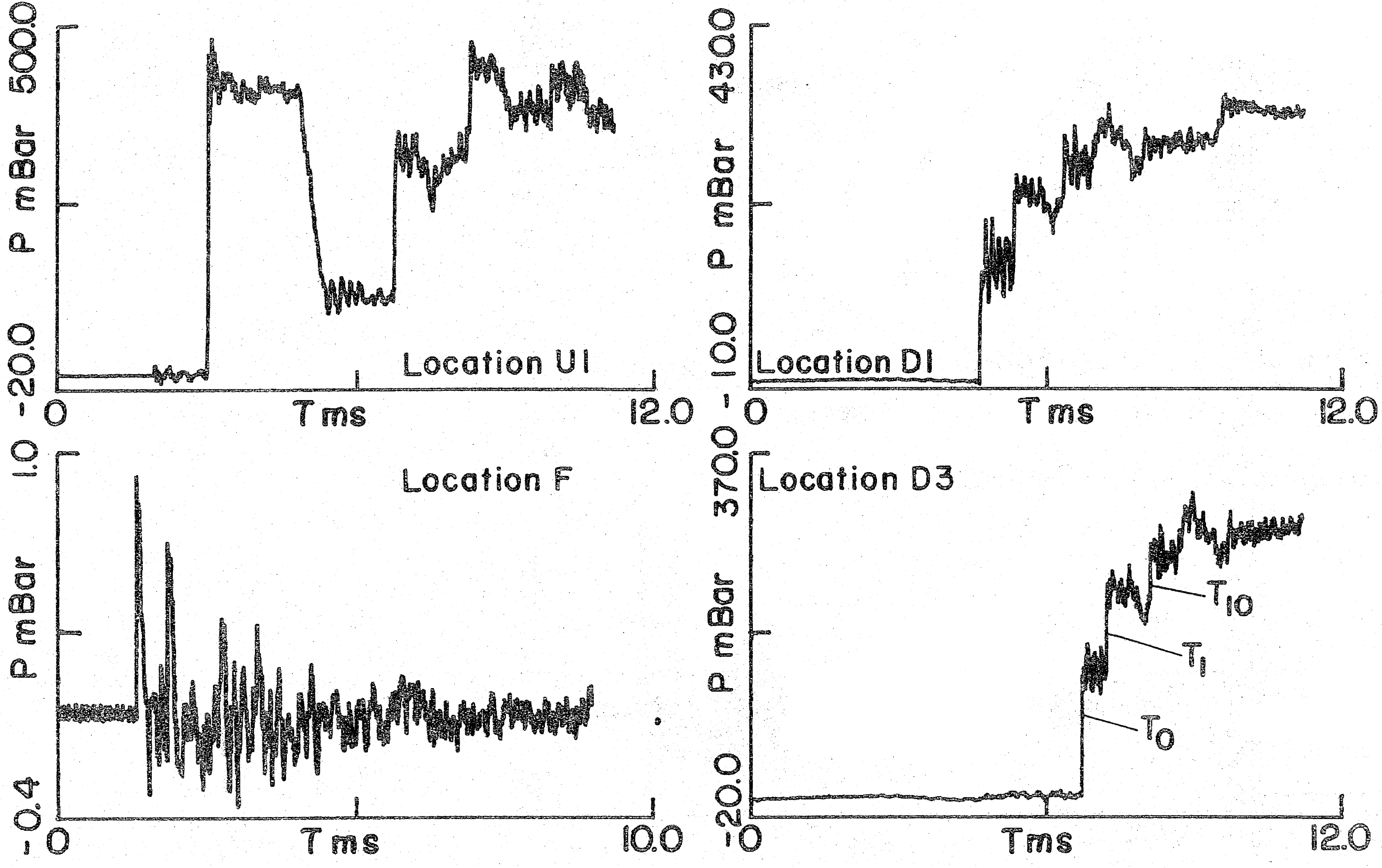

FIGURE 50 PRESSURE HISTORIES OF SHOCK PROPAGATION THROUGH EXPANSION CHAMBER, B, WITH OUTLET EXTENSION. Ms=1.16, SHOCK TUBE

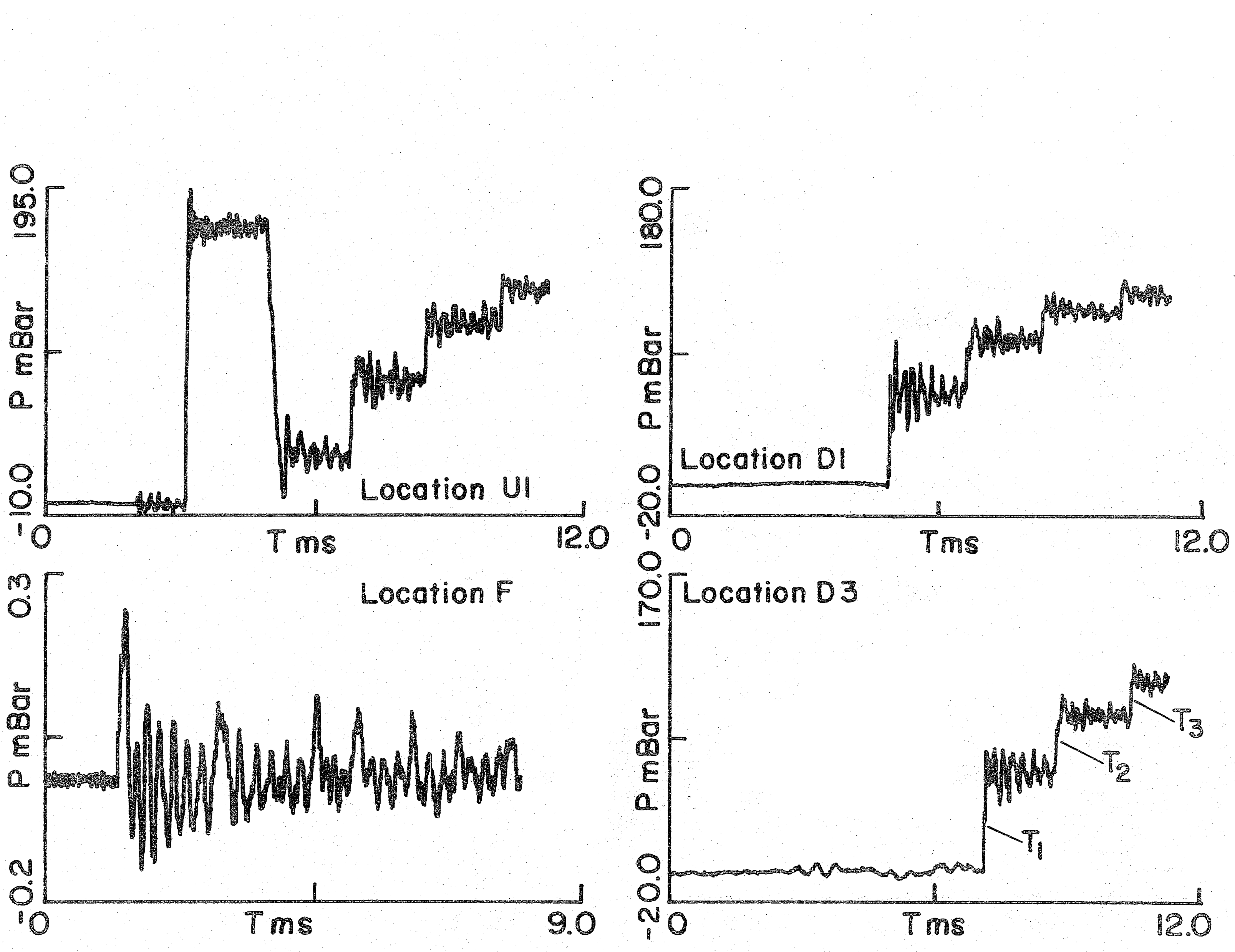

FIGURE 51 PRESSURE HISTORIES OF SHOCK PROPAGATION THROUGH EXPANSION CHAMBER, C. Ms = 1.07, SHOCK TUBE

of the shocks in the diffracted waves to the incident shock is in both cases 0.12.

The pressure wave forms for the extended inlet chamber B with incident shock Mach number of 1.16 are presented in figure 49. An X-T diagram of the shock wave interaction is shown in figure 26.

When the incident shock interacts with the junction between the extended inlet and the main chamber, an expansion wave propagates upstream in the inlet pipe, and a compression propagates upstream in the annulus around the inlet pipe and downstream into the main chamber. The extension of the inlet pipe, which divides the transmitted wave into two portions, causes new waves in the downstream tailpipe which were not observed in the standard expansion chamber experiments. Although the disturbances are more numerous in the downstream tailpipe, the amplitude of the primary disturbance is reduced by extending the inlet.

Increasing the area ratio with the inlet pipe extended reduces the amplitude of the primary disturbance in the downstream tailpipe, while the amplitudes of the subsequent disturbances are slightly increased. The amplitude of the reflected expansion is increased when the inlet extends into the chamber. The pressure behind the primary disturbance for the largest area ratio case rapidly fluctuates at significant amplitude, as was noted with the standard expansion chamber, and presumably occurs for the same reasons.

Figure 50 presents the pressure wave forms for expansion chamber B and extended outlet and incident shock Mach number of 1.16. An X-T diagram of the shock wave interaction is shown in figure 27.

When the outlet pipe of a standard expansion chamber is extended into the chamber, a portion of the first disturbance in the main chamber passes into the downstream tailpipe without amplifying. The rest of the wave continues into the annulus around the extended outlet. When the wave in the annulus reflects from the end of the chamber and interacts with the expansion chamber to outlet junction (Fig. 27), a compression wave propagates upstream in the main chamber and downstream into the tailpipe. Although the disturbances in the tailpipe are more numerous, the amplitude of the primary disturbance is reduced by extending the outlet.

Increasing the area ratio with the outlet pipe extended reduces the amplitude of the primary disturbance in the tailpipe, while the amplitude of the subsequent disturbances increases slightly. The pressure behind the primary disturbance in the largest area ratio (or smallest aspect ratio) fluctuates rapidly at a significant amplitude.

The most striking feature observed in the transmitted waves is the formation of a sawtooth-like wave form behind the leading shock front. From the outset of these experiments, it was thought that the diffraction process was inherently axisymmetric and, at least for weak shocks, the diffracted waves would coalesce in a purely geometrical manner (Fig. 3). That is, the spacing between pulses should decrease as the front gets further from the area change. This argument leads one to the conclusion that the diffracted waves should overtake the leading front. However, we observe a rather constant spacing. The amplitude of the sawtooth is also constant over the lengths of propagation in these experiments. In support of the argument that the diffracted series of pulses behind the leading shock front is a one-dimensional type of motion, is the observation that the amplitude and spacing remain constant over rather long distances in the tailpipe.

4.2.2 Wave Amplitudes

The wave amplitude data for expansion chambers with and without extended inlets or outlets for the case of single pulse excitation are compared with theory. The amplitudes of the first three transmitted waves and the first reflected wave, which were identified in the X-T diagrams, are plotted against area ratio for the case of three incident shock strengths.

For the standard expansion chamber case, the reflected and transmitted wave amplitudes are presented in figure 52, and the theory of Section 3.3.2 is plotted for comparison. The comparison of the transmitted wave amplitudes with the theory is best for the lowest incident shock strength (the theory slightly overestimates the observed values). The deviation of the observed amplitudes from the predicted values is increased for stronger incident shocks. Overall, the effect of incident shock strength is quite small. The comparison of the reflected wave amplitudes with theory shows agreement for $M_s = 1.07$; but for increased incident shock strength, the reflected wave is stronger than predicted by linear theory.

For the extended inlet case, the reflected and transmitted wave amplitudes are presented in figure 53, and the theory of Section 3.4.2 is plotted for comparison. For the low Mach number case, the predicted values of T_0 and T_{01} agree with the observed amplitudes, while the predicted value of T_1 overestimates the data.

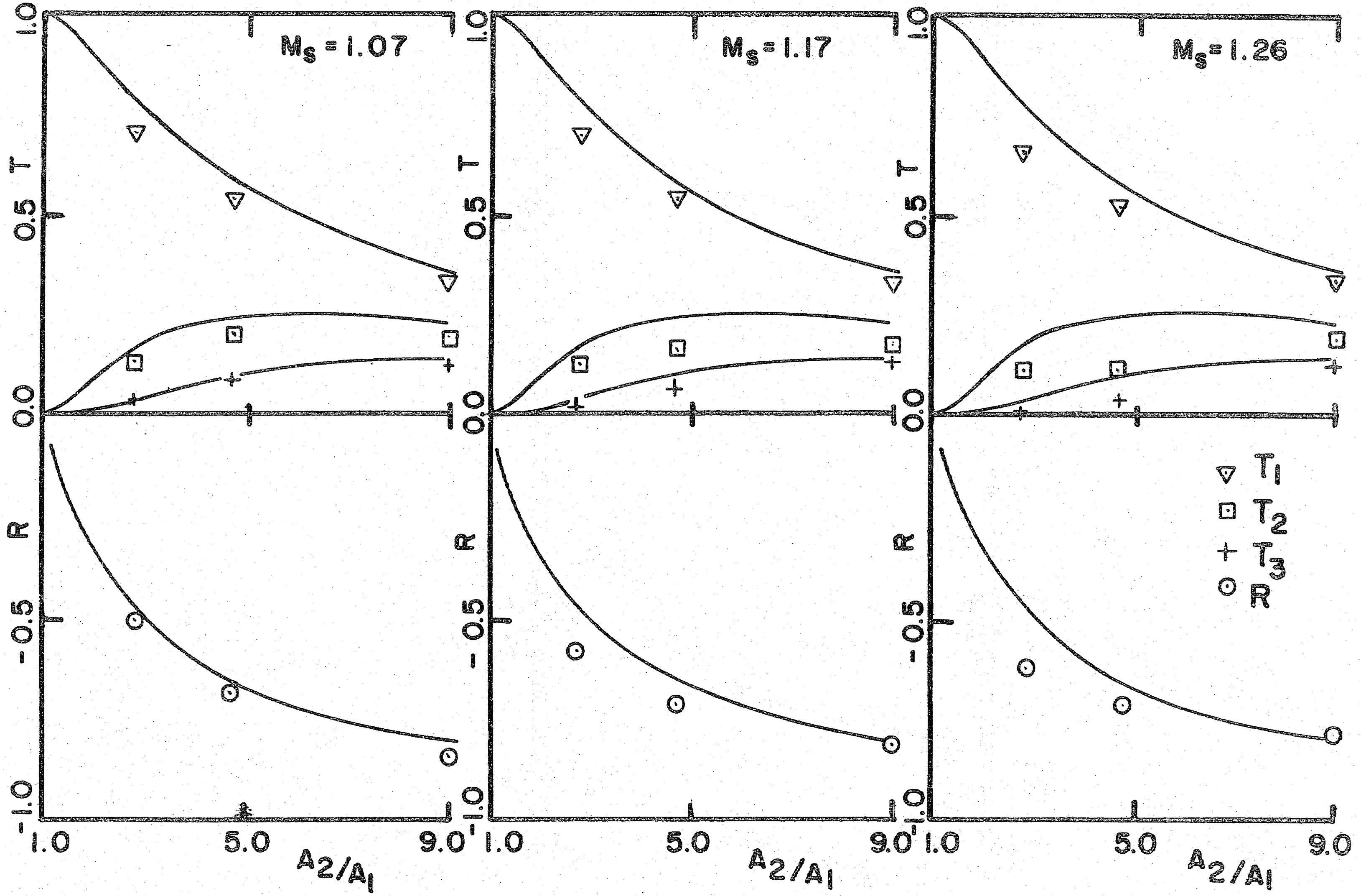

FIGURE 52 TRANSMISSION AND REFLECTION COEFFICIENTS OF EXPANSION CHAMBERS, SHOCK TUBE

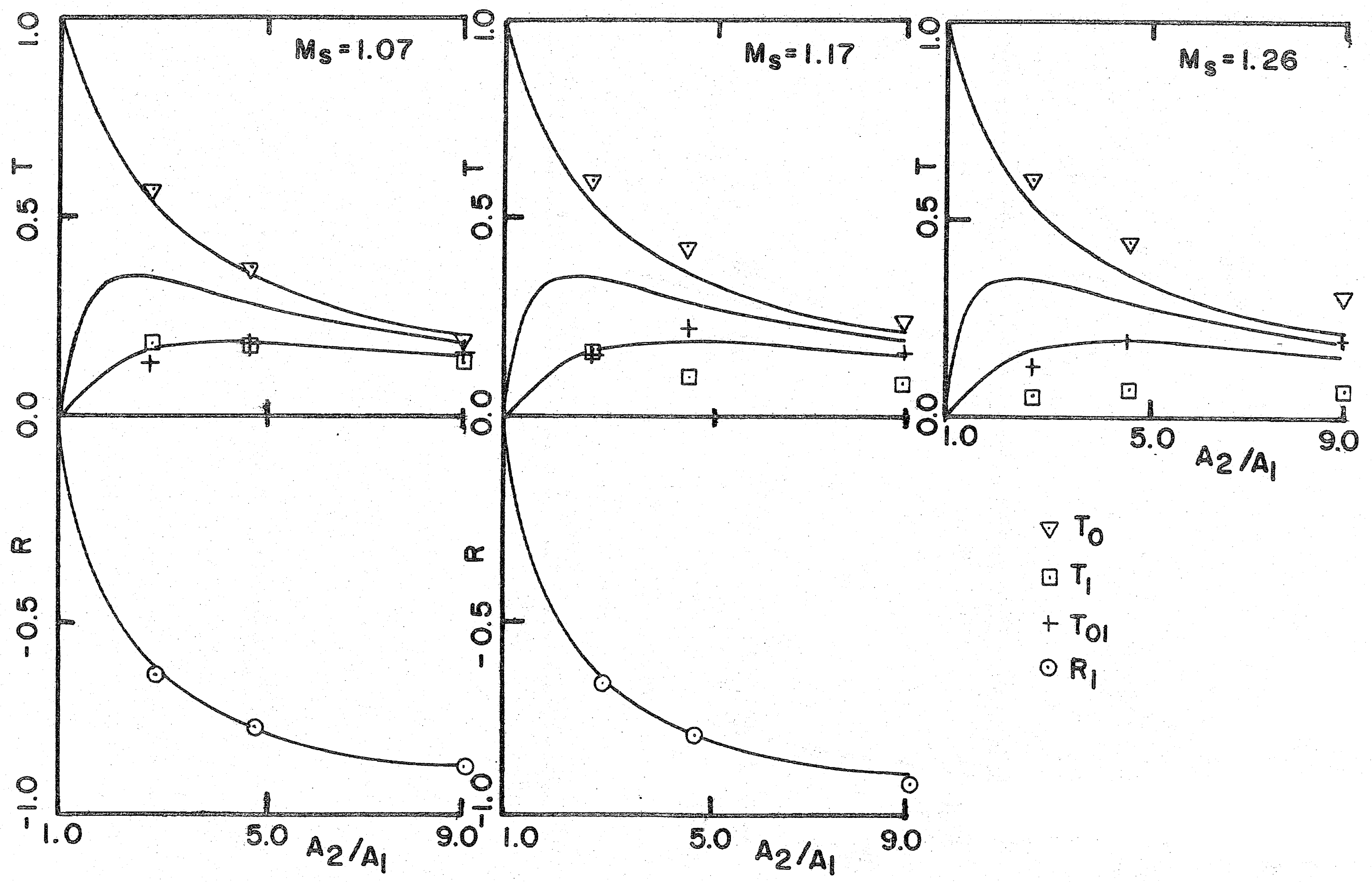

FIGURE 53 TRANSMISSION AND REFLECTION COEFFICIENTS OF EXPANSION CHAMBERS WITH INLET EXTENSIONS, SHOCK TUBE

For higher Mach numbers, the observed amplitude of T_0 is increased, and the observed amplitude of T_1 is decreased. The observed amplitude of T_{01} agrees quite well with predicted values for all Mach numbers. The observed reflected wave amplitudes agree with the predicted values for $M_s = 1.07$ and 1.17; however, for $M_s = 1.26$, the second reflected wave, R_2 (Fig. 26), has overtaken the tail of the first reflected wave, R_1, preventing the total amplitude of R_1 from being observed.

The diffraction process initiated by the arrival of a shock wave at the open end of a tube (the extended inlet in this case), is a very messy problem, involving both shock dynamics and nonsteady viscous flows. The most that can be said is that for short times and acoustic shocks, the flows must be inviscid and potential. Therefore, the fluid can flow around the 180° turn at the end of the tube. Only for this ideal case can one expect that the diffraction process will result in the propagation of waves of equal strength into the annulus and the main chamber.

For $M_s = 1.07$, the data indicate that the ideal description is approximately correct; however, for stronger shocks, this is not the case. For stronger incident shocks, the nonlinearity in the shock diffraction process may result in the wave in the main chamber being stronger than the wave in the annulus.

For the extended outlet case, the transmitted wave amplitudes are presented in figure 54, and the theory of Section 3.4.3 is plotted for comparison. The predicted values of the amplitudes of T_0 and T_{10} agree with observed values for all Mach numbers. The predicted

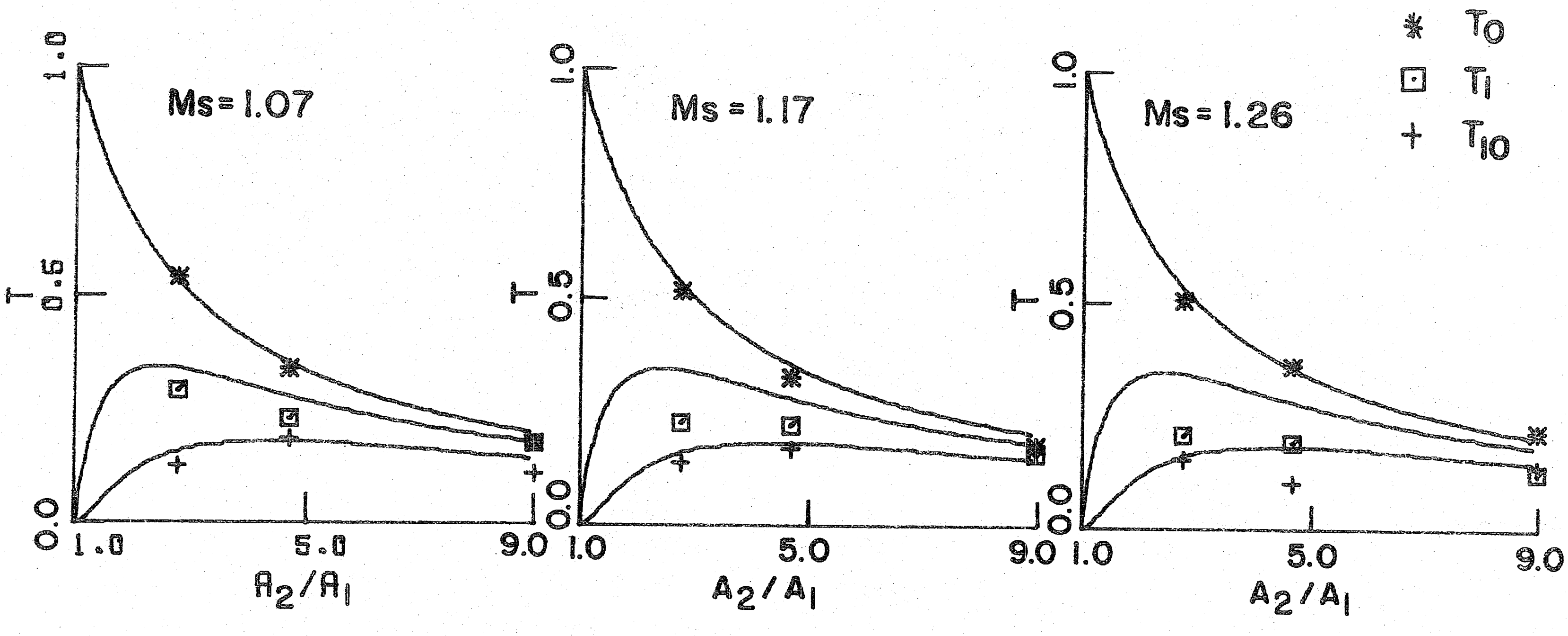

FIGURE 54 TRANSMISSION COEFFICIENTS OF EXPANSION CHAMBERS WITH OUTLET EXTENSIONS, SHOCK TUBE

values of the amplitude of T_1 are above the observed values. The deviation is small for low Mach numbers and increases slightly for higher Mach numbers. The reasons for the increase at high shock Mach numbers are no doubt similar to those discussed for the extended inlet case.

4.2.3 The Effect of Mean Flow on Wave Amplitudes

The wave amplitude data for expansion chambers with and without inlets or outlets extended for the case of repetitive pulse excitation are compared with theory in this section. The amplitude of the first three transmitted waves and the first reflected wave, which were identified in X-T diagrams, are plotted against area ratio. The incident shock Mach number varied from 1.11 to 1.17, depending on the muffler system.

The standard expansion chamber data on transmitted waves are compared with theory in figure 55. The agreement is good for small area ratios, but for the large area ratio (or small aspect ratio), the predicted values are low. The data for reflected waves from the standard expansion chamber and the extended inlet chamber are presented in figure 56. In both cases, the observed reflection coefficients are larger than the predicted values.

The data for transmitted waves from extended inlet chambers are compared with theory in figure 57. The predicted values of T_0 and T_{01} agree with the observed values, while the theory overestimates the observed value of T_1 in every case.

The data for transmitted waves from extended outlet chambers are compared with theory in figure 58. The predicted value of T_0 and

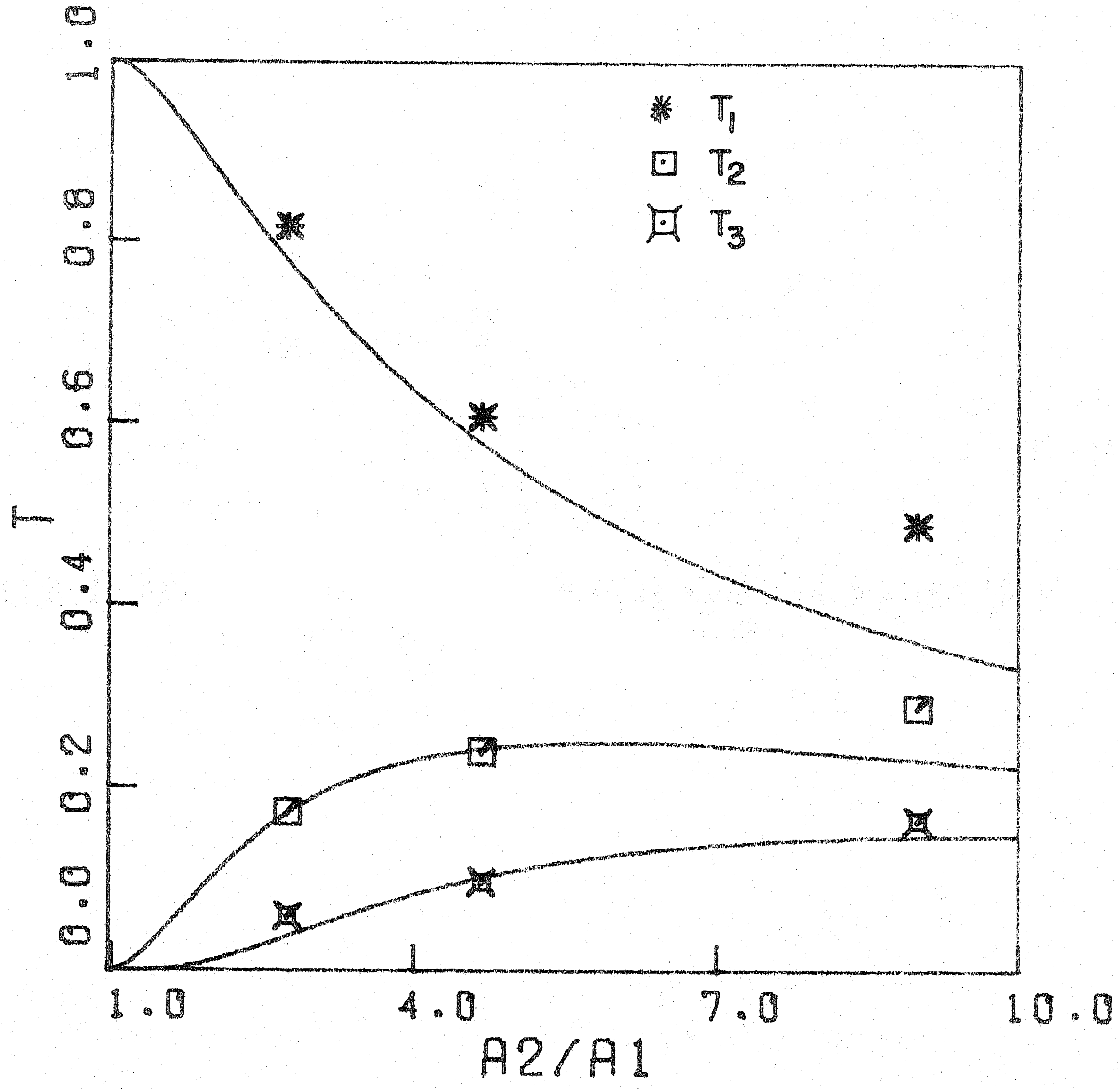

FIGURE 55 TRANSMISSION COEFFICIENTS OF EXPANSION CHAMBERS, RESONANCE TUBE

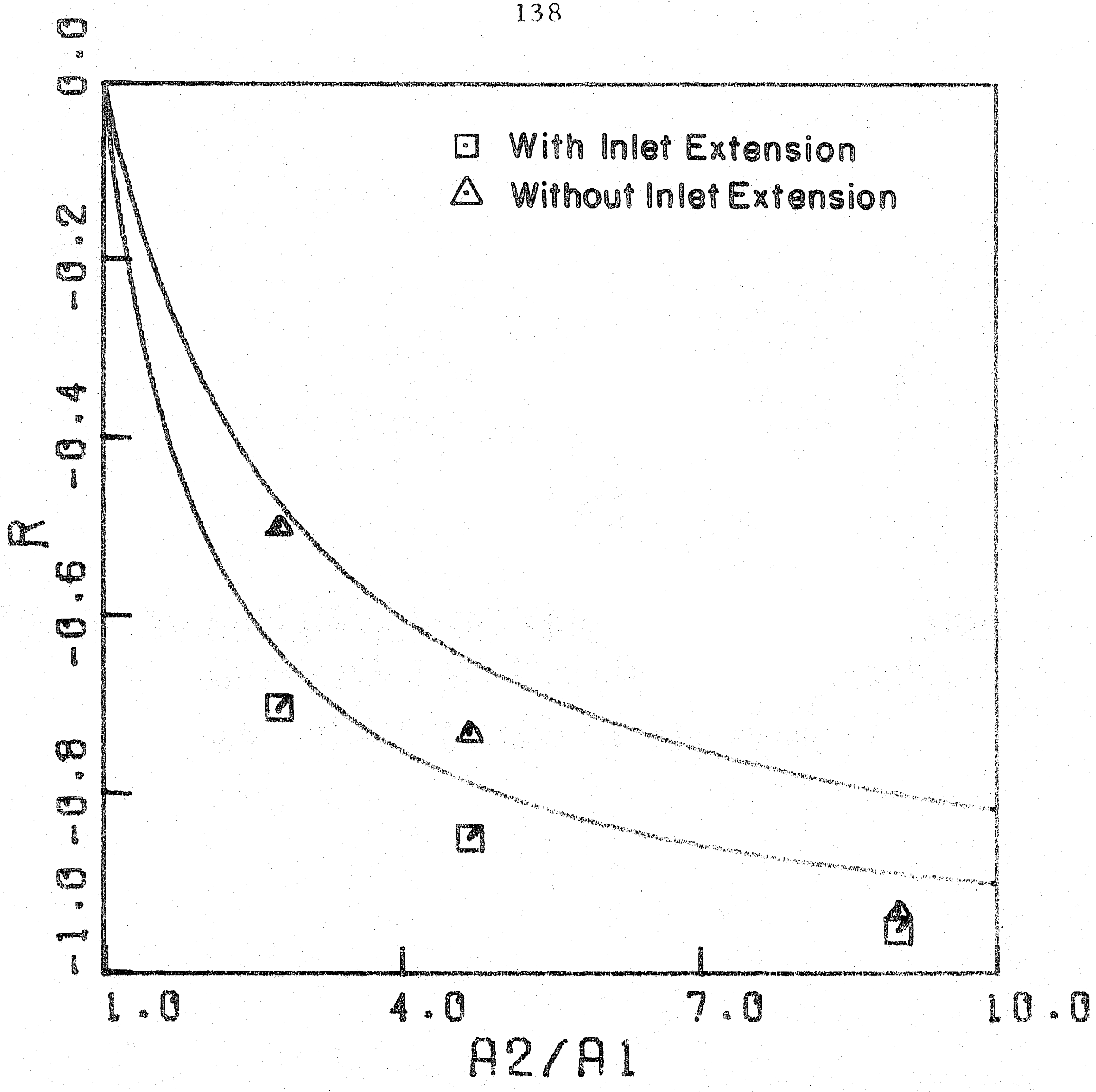

FIGURE 56 REFLECTION COEFFICIENTS OF EXPANSION CHAMBERS WITH AND WITHOUT INLET EXTENSIONS, RESONANCE TUBE

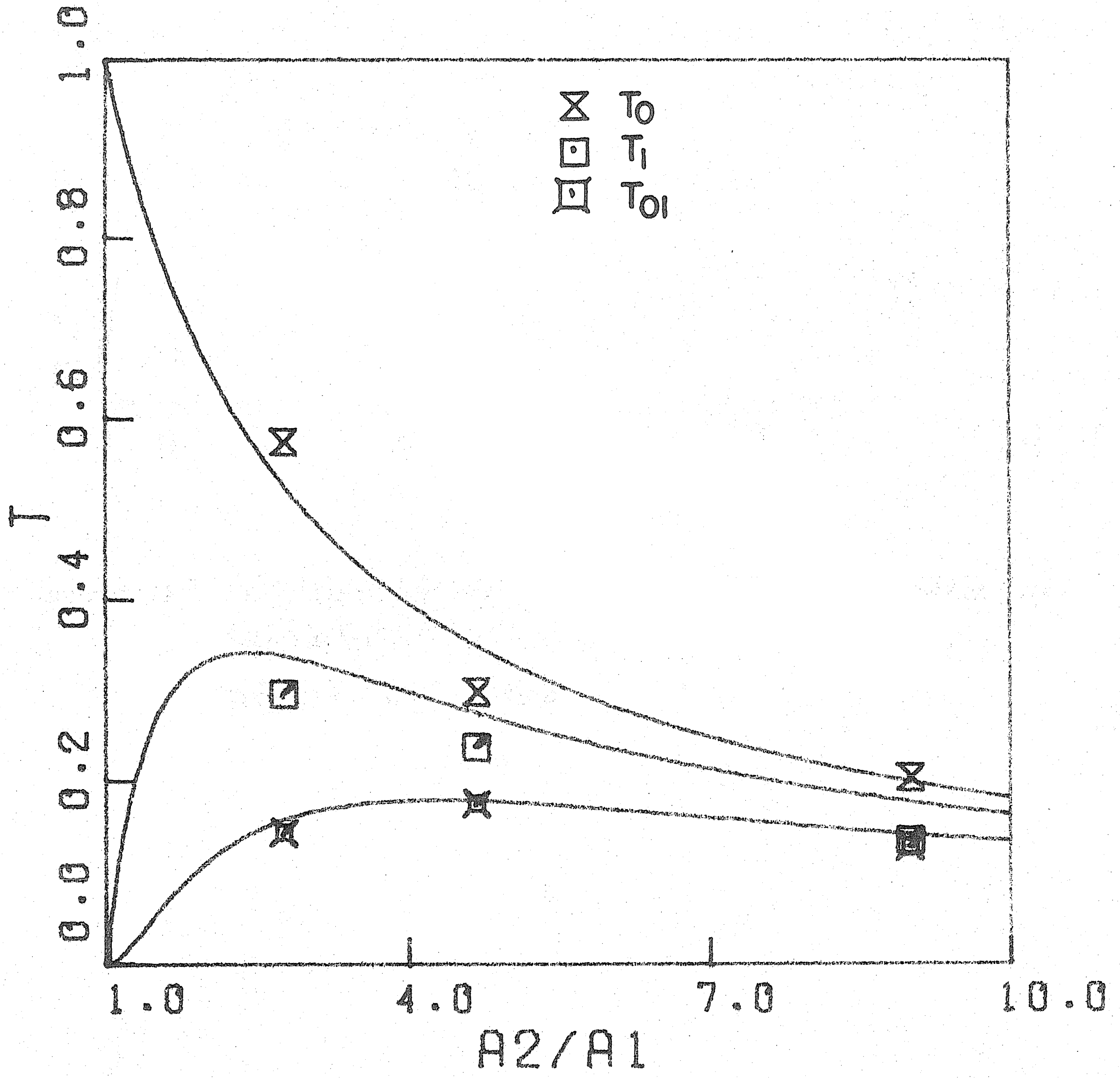

FIGURE 57 TRANSMISSION COEFFICIENTS OF EXPANSION CHAMBERS WITH INLET EXTENSIONS, RESONANCE TUBE

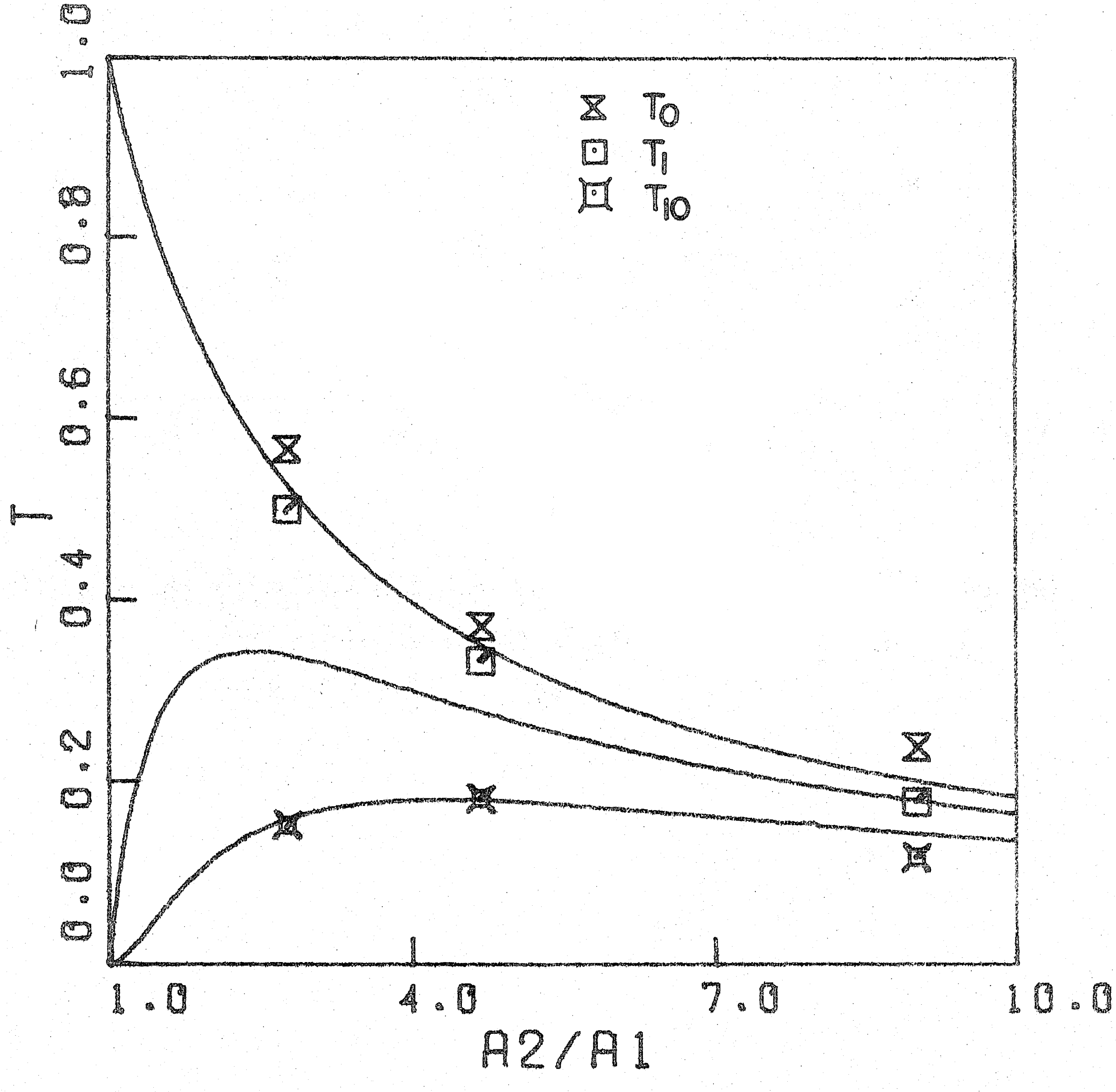

FIGURE 58 TRANSMISSION COEFFICIENTS OF EXPANSION CHAMBERS WITH OUTLET EXTENSIONS, RESONANCE TUBE

T_{10} agree with observed values, while the theory underestimates the observed value of T_1 in every case.

Comparing the single and repetitive pulse excitation data for expansion chamber mufflers, we have observed (1) only small differences in the reflected and transmitted wave data for the standard chamber, (2) for the extended inlet chamber, the first transmitted wave is weaker in the repetitive excitation case, while only small differences are observed for the following waves, and (3) for the extended outlet chamber, the second transmitted wave is stronger in the repetitive excitation case, while only small differences are observed for the first and third transmitted waves.

To summarize the results for the three variations of expansion chamber mufflers, we have observed that (1) increasing the area ratio decreases the amplitude of the primary disturbance and increases the amplitudes of the subsequent disturbances, observed in the tailpipe, (2) extensions can significantly reduce the amplitude of the primary disturbance for a fixed area ratio, and (3) for the largest area ratio, or as importantly, the smallest aspect ratio, the effects of diffraction are significant. The waves diffracted at the upstream junction have not coalesced with the primary disturbance when it reaches the downstream junction and lead to rapid fluctuations in pressure observed in the tailpipe behind the primary disturbance. Thus, for small aspect ratios, the form of the transmitted waves is altered.

V. RESULTS - EXTERNAL WAVES

5.1 Sound Radiation from Open Pipes

When a weak shock reflects from the open end of a pipe, sound is radiated to the far field. Initially, a toroidal wave is diffracted off the incident shock as it passes through the exit. In this way the energy in the plane incident shock is redistributed spherically to the far field.

The theory for the sound radiation produced by the reflection of a plane weak shock from the tailpipe exit was given in Section 3.5, and is compared with measurements in this section. The form of the sound radiation is a narrow pulse. On the tube axis, the pulse is rectangular and has amplitude equal to the incident shock, while at 90 degrees the pulse is a distorted ellipse.

The predictions from the linear theory at 90 degrees agree with measurements when the incident shock is weak. For stronger shocks, the radiated pulse distorts due to nonlinearity, while the amplitude and decay rate of the radiated pulse does not appear to be significantly changed by nonlinear effects. In the near field, the amplitude of the radiated pulse is rather directional.

5.1.1 Radiated Wave Forms

Radiated wave forms produced in the single and repetitive pulse facilities are presented in this section. In the experiments using the resonance tube, the wave forms were observed in the near and far fields and on and off the tube axis. In the single-pulse experiments, the wave form was observed in only one position (in this case, the incident shock Mach number was varied).

The purpose of the single-pulse experiments was to observe the effects of incident shock strength on the radiated wave form. The microphone was located 34.6 diameters from the source and at 90 degrees to the tube axis. The pressure signals were digitized by computer (Section 2.3.2). The incident shock Mach numbers were 1.04, 1.07, 1.17, and 1.20. The wave forms are shown in figure 59.

The wave form is almost symmetric for the weakest shock. The wave fronts are steeper and the wave tails are smoother for stronger shocks. For very narrow fronts, diffraction of waves over the microphone is important. For the strongest Mach number, the wave front is so thin that pressure doubling occurs on the face of the 1/8 inch microphone for about six μsec. Therefore, for shock strengths above 1.17, the measured maximum-slope wave-front thickness is limited by the rise time of the microphone (six μsec).

In the repetitive-pulse experiments, radiated wave forms were recorded on and off the tube axis and in the near and far field. The incident shock Mach number was 1.17.

Figure 60 shows the radiated wave form six diameters from the exit on the axis and at 10 diameters at 90 degrees to the tube axis. The shock Mach number was 1.17. For the on-axis pressure measurements, the pressure was measured with a fast-rise (2 μsec) piezoelectric pressure transducer (PCB model 112A21). The transducer was flush mounted in the center of a 15 cm diameter baffle. The baffle was oriented normal to the local direction of propagation. Since the pulses were narrow, diffraction waves from the edge of the baffle do not reach the transducer until after the entire pulse has reflected from the face of the transducer.

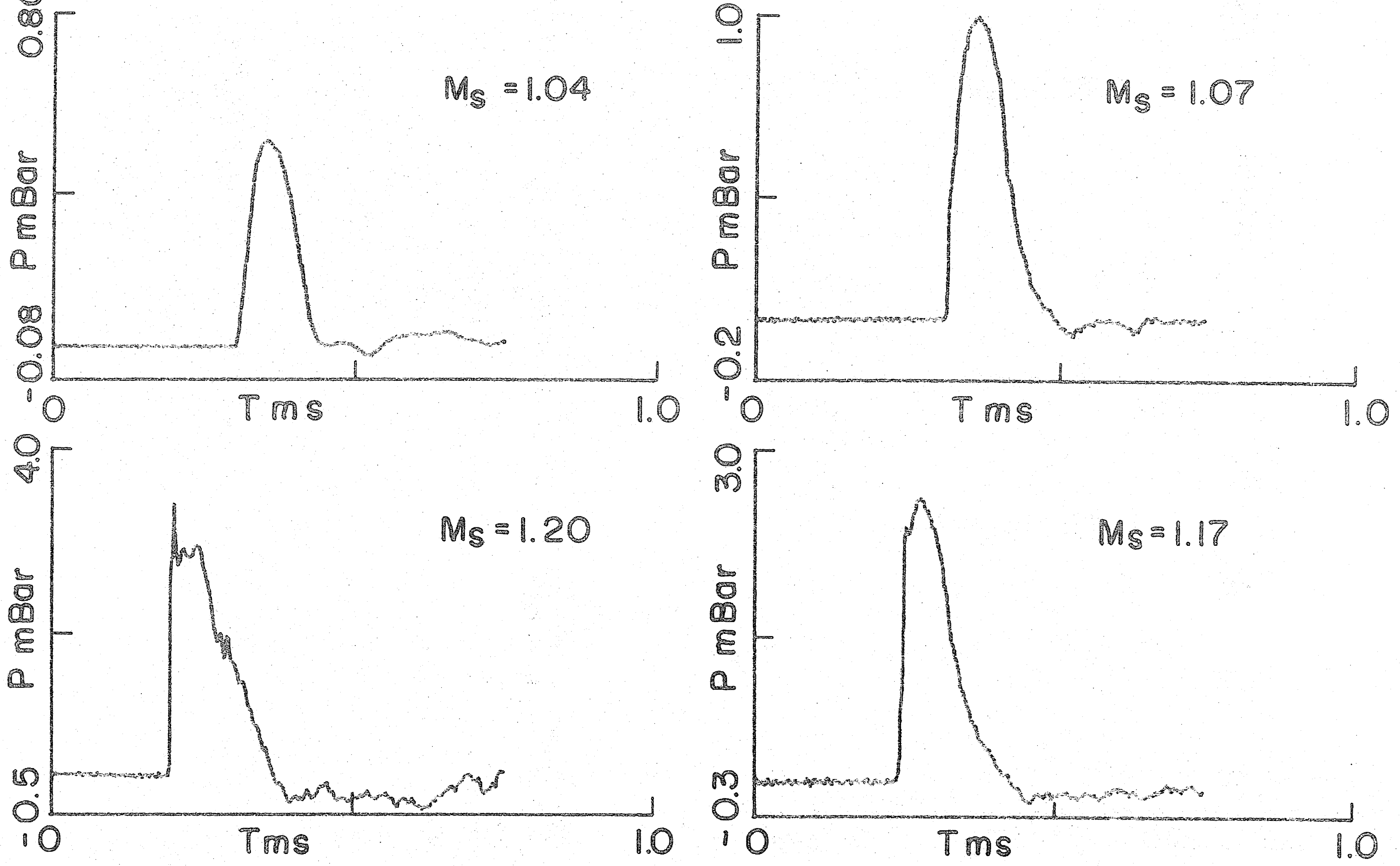

FIGURE 59 RADIATED PRESSURE HISTORIES OF SHOCKS PROPAGATING OUT OF CIRCULAR TUBES, SHOCK TUBE

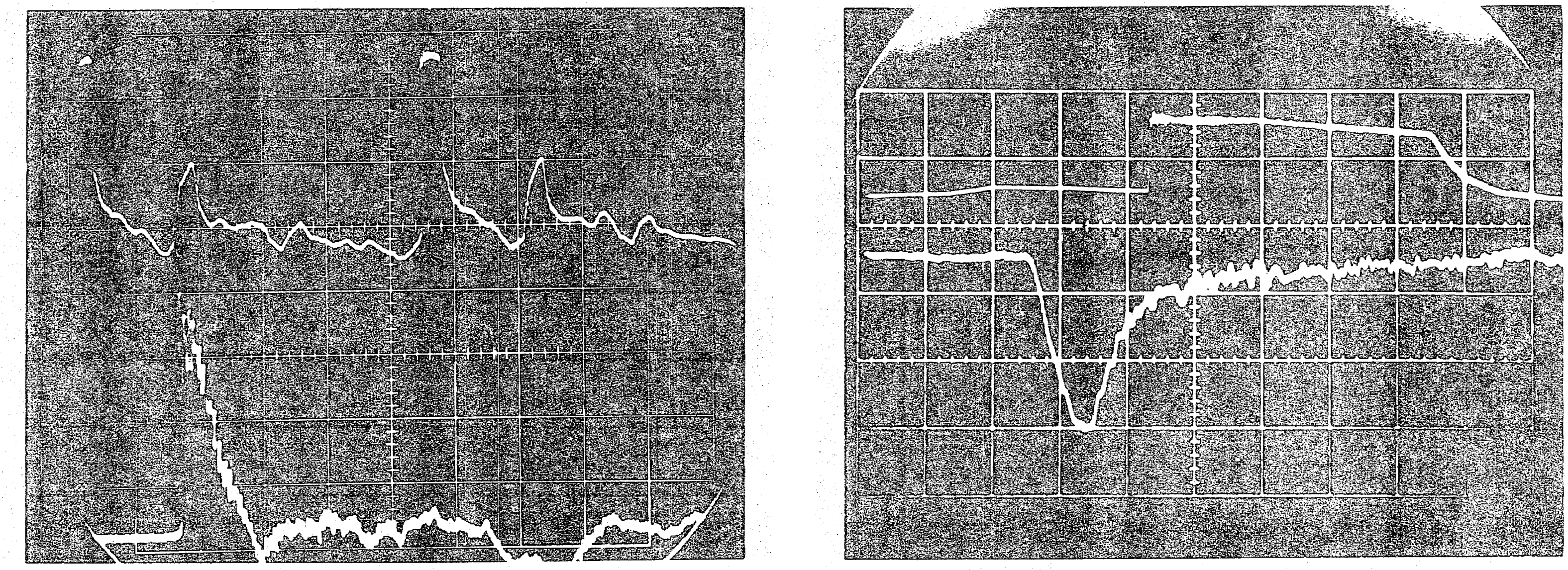

A

B

BEAM	WAVEFORM	SENSITIVITY	VERTICAL	HORIZONTAL	SENSITIVITY	VERTICAL	HORIZONTAL	
upper	internal	$2.28 \frac{mB}{mV}$	$50 \frac{mV}{cm}$	$5 \frac{mS}{cm}$	$68.9 \frac{mB}{V}$	$5 \frac{V}{cm}$	$1 \frac{mS}{cm}$	
lower	external	$1.33 \frac{mB}{mV}$	$10 \frac{mV}{cm}$	$50 \frac{\mu S}{cm}$	$(92.5 \frac{\mu B}{mV}$	$10 \frac{mV}{cm}$	$100 \frac{\mu S}{cm})$	inverted

FIGURE 60 RADIATED PRESSURE WAVE FORMS: (A) ON TUBE AXIS, AND (B) AT 90° TO TUBE AXIS, $\omega = 36.4$ HZ, RESONANCE TUBE

As predicted by the theory, the pulse was narrower on axis than off axis. However, while the width of the pulse radiated at 90 degrees is quantitatively predicted (measured 140 μsec, predicted 110 μsec), the on-axis pulse width is considerably thicker than the theory predicts (measured 55 μsec, predicted 2 μsec). The wave form measured on the axis is also not predicted by the theory. The idealized theory (the pure Heaviside function source strength) predicts a rectangular wave form whose amplitude is that of the incident shock. However, a small amount of nonlinearity (c.f. figure 2) causes the diffracted expansion waves to travel across the back side of the shock, resulting in a thicker wave with a weaker shock front. This explanation is consistent with on-axis measurements. This nonlinear process, which takes place in the near field, has an effect on the far field pulse only near the axis.

5.1.2 Wave Amplitude

Measurements of the radiated sound produced in both repetitive and single-pulse excitation experiments by the reflection of a weak shock from the open end of a tube are compared with predictions in this section.

For the single-pulse excitation experiments, the peak radiated pressure is compared with theory in figure 61. Using the reflection time computed by Rudinger, the amplitude of the radiated pressure pulse is $\frac{1.41}{2\pi} \frac{D}{r}$, or 6.48×10^{-3} at 34.6 diameters. As discussed in section 3.5, the reflection time, in which the velocity in the tailpipe exit doubles, is important. When the reflection time is much longer than the characteristic time D/a, the amplitude of the radiated pulse is

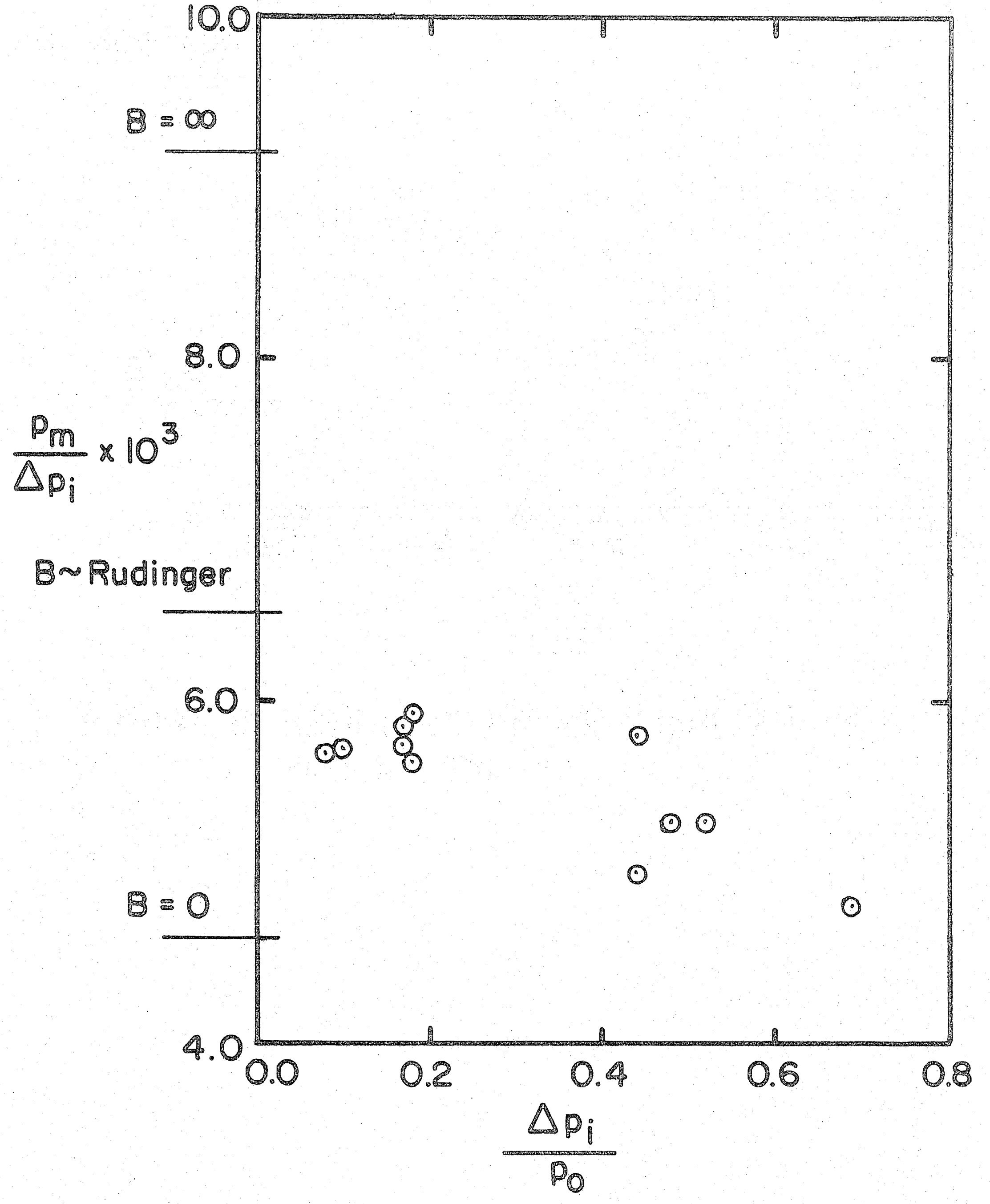

FIGURE 61 RADIATED PULSE AMPLITUDES, SHOCK TUBE

$\frac{1.0}{2\pi}\ \frac{D}{r}$, i.e., there is no contribution from the doubling. When the reflection time is much shorter than the characteristic time, the amplitude of the radiated pulse is $\frac{2.0}{2\pi}\ \frac{D}{r}$, or the portion of the radiated pulse due to velocity doubling is equal to the portion due to the velocity behind the shock.

For weak shocks, measured amplitudes of the radiated pulse indicate that the reflection time is roughly 50% longer than acoustic theory predicts ($t = 3\ D/a$ or $B = 1.15$). For stronger shocks, the measured amplitudes indicate very long reflection times ($B = 0$). The reason for this change in reflection time is not known. For weak shocks, the reflection occurs fast enough to affect the amplitude of the radiated pulse, and for stronger shocks, only the velocity behind the shock contributes to the radiated pulse.

To investigate the amplitude decay and directionality of the sound pulses radiated from the tailpipe exit of the resonance tube facility, the pressure was measured on the tailpipe axis from 2 to 20 diameters and at 90 degrees from 2 to 176 diameters. The range of pressure levels observed varied four orders of magnitude so that three transducers were required. Their locations are shown in figure 62.

The ground plane is 13 diameters below the tailpipe exit and extends for 55 diameters in the horizontal direction. Measurements are made in the plane of the tailpipe exit or on the tailpipe axis. As the radiated pulse is emitted spherically from the tailpipe exit, the portion below the exit plane reflects from the ground plane. As a result of observing the incident wave with a fast time scale, the

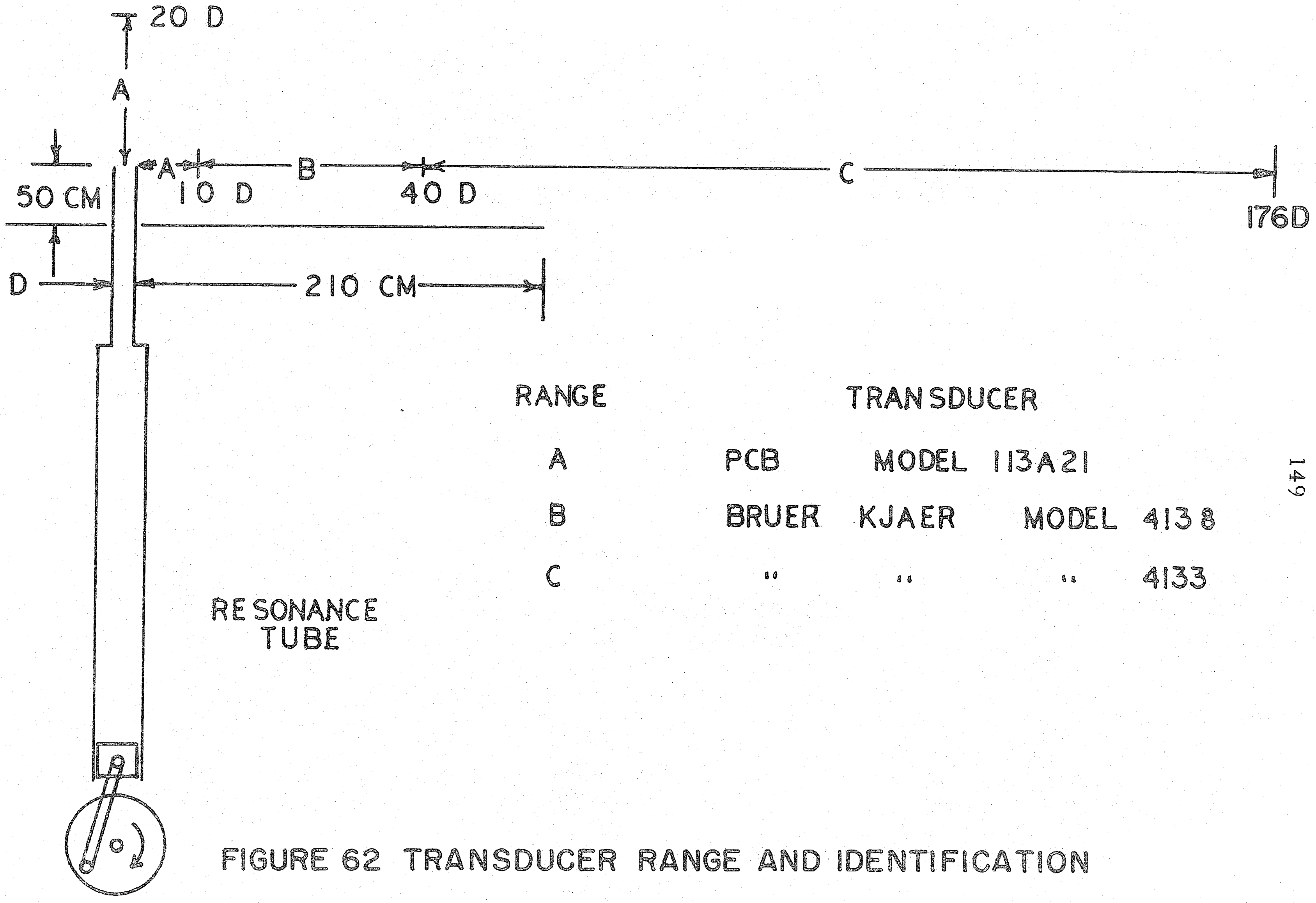

RANGE	TRANSDUCER		
A	PCB	MODEL 113A21	
B	BRUER	KJAER	MODEL 4138
C	"	"	" 4133

FIGURE 62 TRANSDUCER RANGE AND IDENTIFICATION

reflected wave is not seen. When the pulse passes the edge of the ground plane, a circular wave is diffracted off the edge. Aside from the diffracted wave, the waves which reach location F have no knowledge of the ground plane. Since the diffracted wave is not detected at location F, the observations are taken as a good approximation of the free-field pulse.

The peak amplitudes of the pulses are normalized by the shock amplitude and plotted in figure 63 against distance of travel normalized by the diameter of the tube. Near the source, the peak pressure is much higher and decays much faster on axis than at 90 degrees. Since the amplitudes are equal at 20 diameters, the amplitudes must be approximately equal above and below the tailpipe exit plane, or the pulse is spherical. At 90 degrees to the tube axis, the amplitude decays inversely with distance. No distortion is observed with distance of propagation; the wave fronts do not steepen, nor do their tails smooth out.

For the resonance tube experiments, the pulse is essentially radiated spherically, as opposed to the shock tube experiments where the pulse is hemispherical. Thus, the source strength must be divided by two ($p_m = \frac{\Delta p}{2} \frac{1.41}{2\pi} \frac{D}{r} = \Delta p \, .112 \frac{D}{r}$). The predicted peak pressure of the radiated pulse is in reasonable agreement with measurements as shown in figure 63.

Sloan and Nettleton (1975) have measured the pressure history of a shock propagating through a very large discontinuous area change. Measurements were made only on the axis. The three main differences between the experiments discussed in the current work and those of

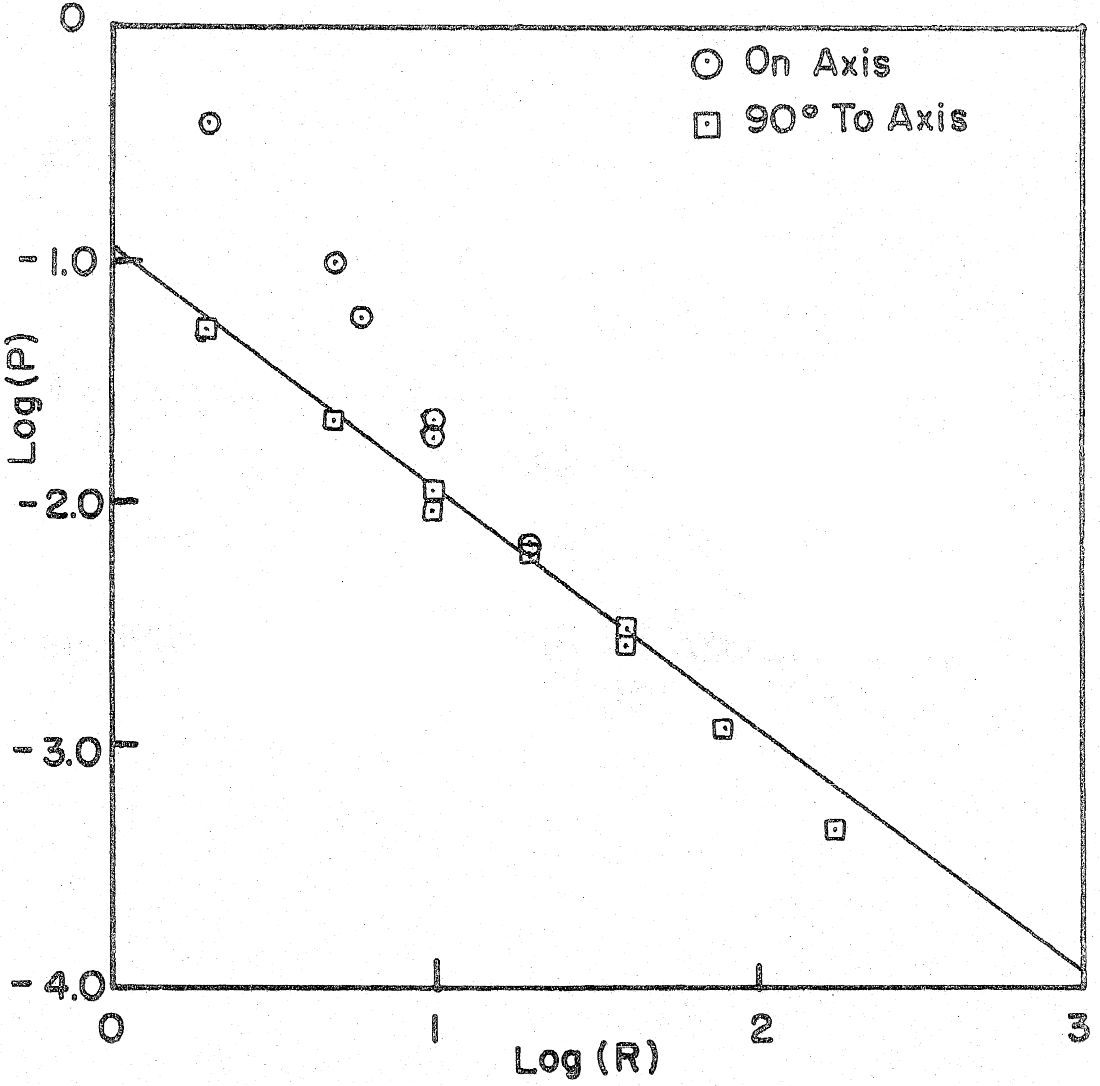

FIGURE 63 RADIATED PULSE AMPLITUDES, RESONANCE TUBE

Sloan and Nettleton are their use of: (1) stronger shocks, (2) a discontinuous area change, which in the near field is equivalent to an open end in a baffle, and (3) measuring stations which were confined to the near field ($\frac{r}{D} < 4.0$). In addition, three regions of propagation (Fig. 63a) are identified, which are: (1) the region between the open end and the point where the diffracted waves reach the axis, point Q, (2) a transition region from point Q to the point where the shock strength begins to decay spherically, point S, and (3) beyond point S where the spherical decay is apparently centered at point P.

The apparent origin is located by extrapolation of the data beyond point S to the point where the pressure was infinite (the point source). A linear plot of the data is used to locate the point where the spherical decay begins (Fig. 63b). The point where the diffracted waves reach the axis is defined as the point at which the measured pressure is first below the amplitude of the incident shock.

The locations of points P, Q, and S from the current work are compared with locations reported by Sloan and Nettleton in Table 3. In all cases, point Q is located within one diameter of the exit. The data from the current work shows a longer transition region than the lengths observed by Sloan and Nettleton. The amount of the disagreement is larger than one might expect; however, it is reasonable that the transition region be longer for weaker shocks, because nonuniformities in shock strength move more slowly along the shock front for weaker shocks.

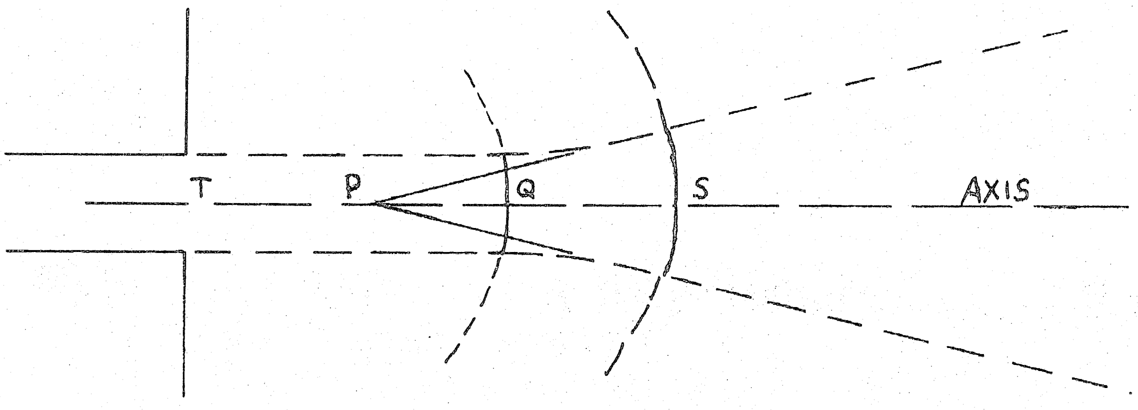

FIG.63a SHOCK WAVES THROUGH DISCONTINUOUS AREA CHANGES (Sloan and Nettleton, 1975)

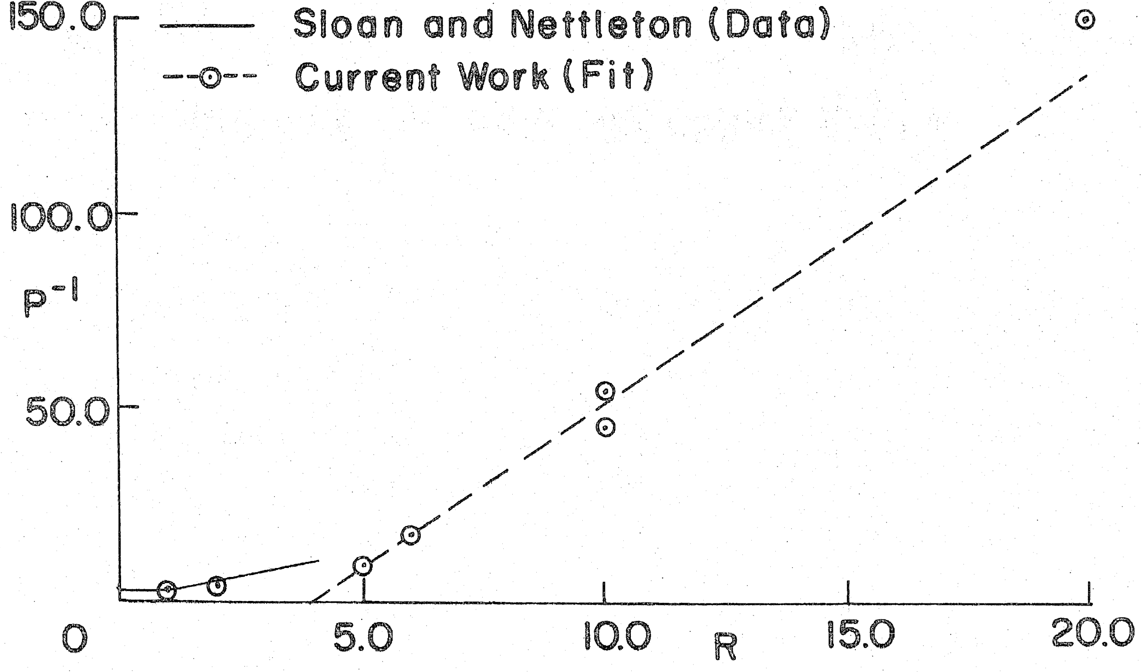

FIG.63b ON AXIS PRESSURE DECAY

DATA	M_s	$(\frac{\overline{TQ}}{D})$	$(\frac{\overline{TP}}{D})$	$(\frac{\overline{TS}}{D})$
Current Work	1.16	1.0 ± 0.2	3.89	5.0
Sloan and Nettleton	1.55	.76 ± 0.04	0.67 ± 0.06	1.4
	1.92	.78 ± 0.02	0.56 ± 0.03	1.3
	2.14	.76 ± 0.04	0.43 ± 0.06	1.0
	2.42	.72 ± 0.06	0.48 ± 0.06	1.0

COMPARISON OF DATA FROM CURRENT WORK WITH DATA FROM SLOAN AND NETTLETON

TABLE 3

5.2 <u>Sound Attenuation by Enclosed Perforated Tubes</u>

The sound radiation produced by the transmission of a shock wave through enclosed perforations is presented in this section. In particular, the measured wave forms and sound pressure levels or attenuations are presented and compared with the theory of Section 3.5.

For infinite enclosures with small perforated area ratios, the radiated wave is the standard narrow pulse, because the transmitted wave in the muffler tailpipe is a shock. For larger perforated area ratios or, just as importantly, long sections of perforations, the transmitted wave is more complex, as discussed in Section 4.1.1. The trailing portion of the transmitted wave has the largest amplitude and is a smooth compression with a slow rise time. The relative amplitude of the pulse radiated by a smooth compression is much smaller than the pulse radiated by a shock of equal amplitude.

The infinite-enclosure cases provide a base-line attenuation for the finite enclosure cases. However, we have found a critical perforate area ratio, where the enclosure becomes important. For perforate area ratios above critical, the enclosure prevents further increases in attenuation.

5.2.1 Wave Forms

In the single-pulse experiments, the location of the perforations was such that for infinite-enclosure case, the sound radiated from the tailpipe was isolated from the sound radiated from the perforations. The perforations were enclosed by the room in which the shock tube is located; and since the tailpipe extended through a sealed hole in the wall, the two sources of sound were isolated.

The radiated wave forms for the infinite enclosure cases revealed a very interesting result. For small perforate area ratios, the transmitted wave is a shock and the radiated wave is a narrow pulse. However, for larger area ratios, the transmitted wave is a shock followed by a sharp expansion which is in turn followed by a smooth compression, raising the pressure to p_4 (c.f. Section 4.1.1). Figure 64 shows the wave forms at locations U, D1, D2, and F.

By the time that the transmitted wave reaches the exit, the amplitude of the leading shock has decayed to a fraction of the amplitude of the smooth compression. The leading shock produces the initial radiated pulse. Using the amplitude of the shock at location D2, $\Delta p = 39$ mBar, the amplitude of the leading radiated pulse should be 253 μBar. The measured pressure is 160 μBar.

The new result is that, since the rise time of the smooth compression is so long, the amplitude of the radiated pulse is reduced. If the smooth compression were a shock of the same amplitude, $\Delta p = 150$ mBar, the amplitude of the radiated pulse would be 973 μBar. The measured amplitude of the second pulse is 115 μBar. The maximum-slope rise time of the transmitted wave at location D2, which is 1.20 msec, is about eleven times the characteristic time of the tailpipe, 110 μsec.

Thus, we observe that increasing the rise time of the wave front inside of the tailpipe reduces the amplitude of the radiated pulse. The characteristic time for the sound radiation process is the acoustic travel time across the tailpipe, D/a. Qualitatively, only rise times longer than the characteristic time should reduce the amplitude of the radiated pulse at 90°, which is consistent with our observations.

The radiated wave forms from the repetitive-pulse excitation experiments are shown in figures 45, 46, and 47. The effect of enclosures, as was noted in Section 4.1.3, is that even numbered

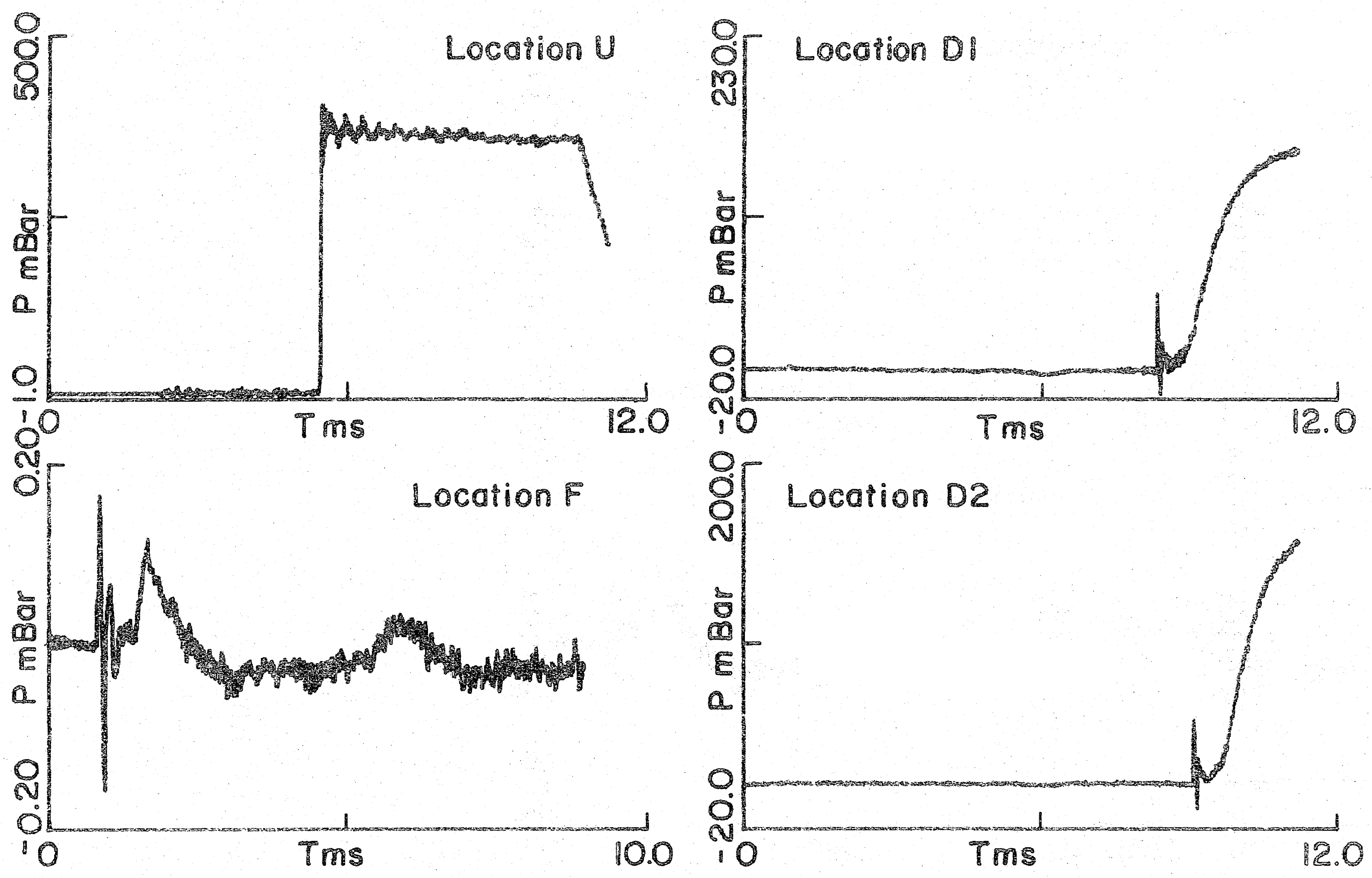

FIGURE 64 PRESSURE HISTORIES OF SHOCK PROPAGATION PAST A PERFORATED TUBE $A_E/A = 4.00$, SHOCK TUBE

transmitted waves are smoother compressions than the odd numbered waves. In a few cases, the even numbered waves are smooth enough that shocks do not form before they reach the tailpipe exit; this is seen in figure 45, enclosure B, where the second radiated pulse is smooth, unlike those produced by shocks.

When the length of the perforated tube approaches the enclosure length, for perforate area ratios $AE/A \doteq 4.0$, the odd-numbered transmitted waves may overtake the even-numbered waves. In figure 47, the enclosure B and C cases depict this situation. The first two radiated pulses are almost superimposed. If the tailpipe was longer or the incident shock stronger, the first pair of transmitted waves would have coalesced, in which case the attenuation would be reduced.

5.2.2 Radiated Sound Pressure Levels

The maximum attenuation that can be achieved by a perforated tube muffler of a given area ratio is the infinite-enclosure case. The attenuation in this case is the base-line value to which all enclosed perforated tube mufflers can be compared. The attenuation is plotted against perforated area ratio and compared with the theory in figures 65 and 66. For the case of single-pulse excitation, the discharge coefficient is used to correct the perforate area ratio (Section 4.1.2). The theory assumes no enclosure and should be compared with the infinite enclosure cases.

The predicted attenuations are about 2 decibels less than measured values for small area ratios, while for large area ratios, the predicted values are much less than measured values. For large area ratios, the deviations occur for the same reasons as were discussed

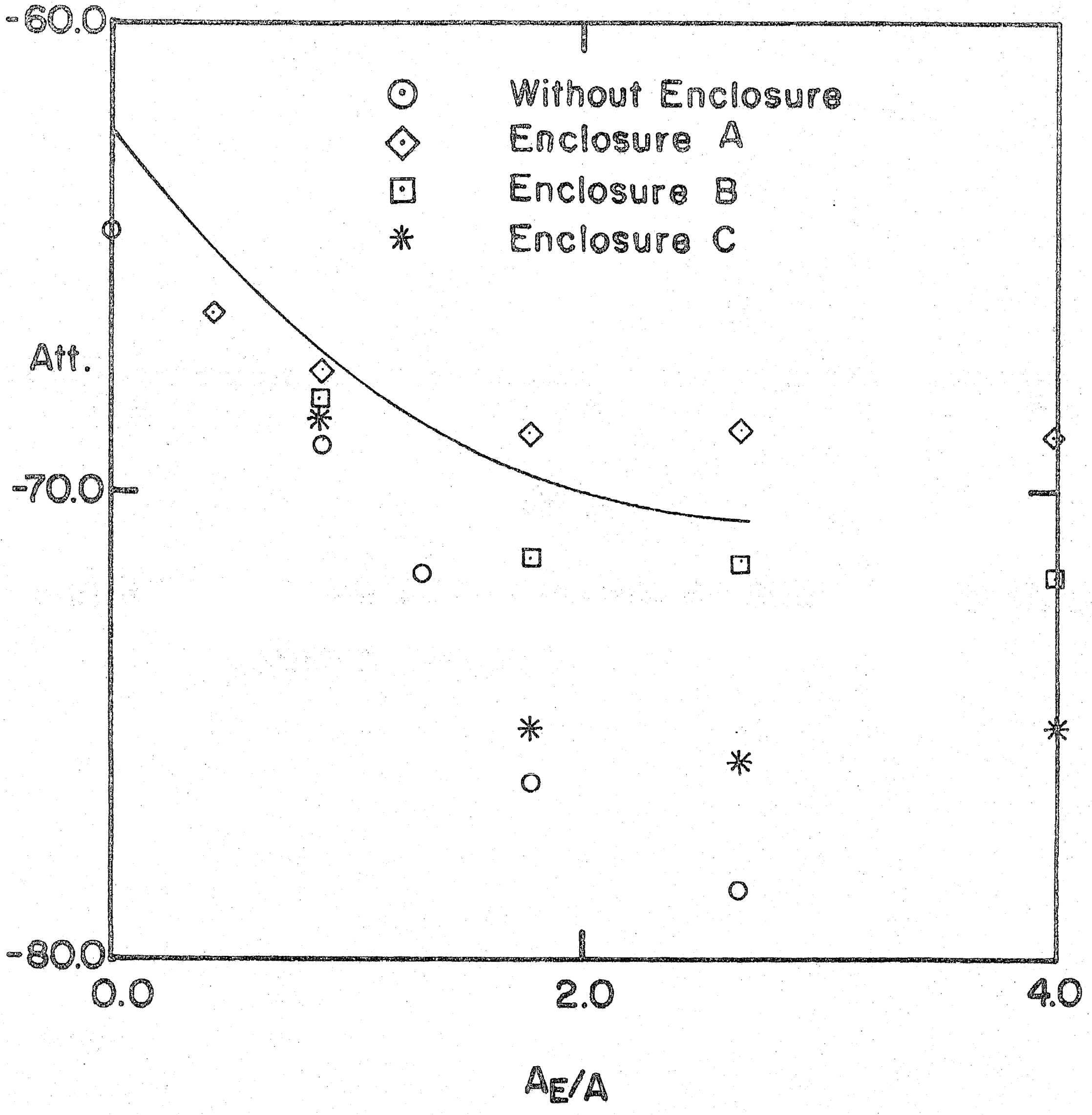

FIGURE 65 SOUND ATTENUATION BY PERFORATED TUBES, SHOCK TUBE

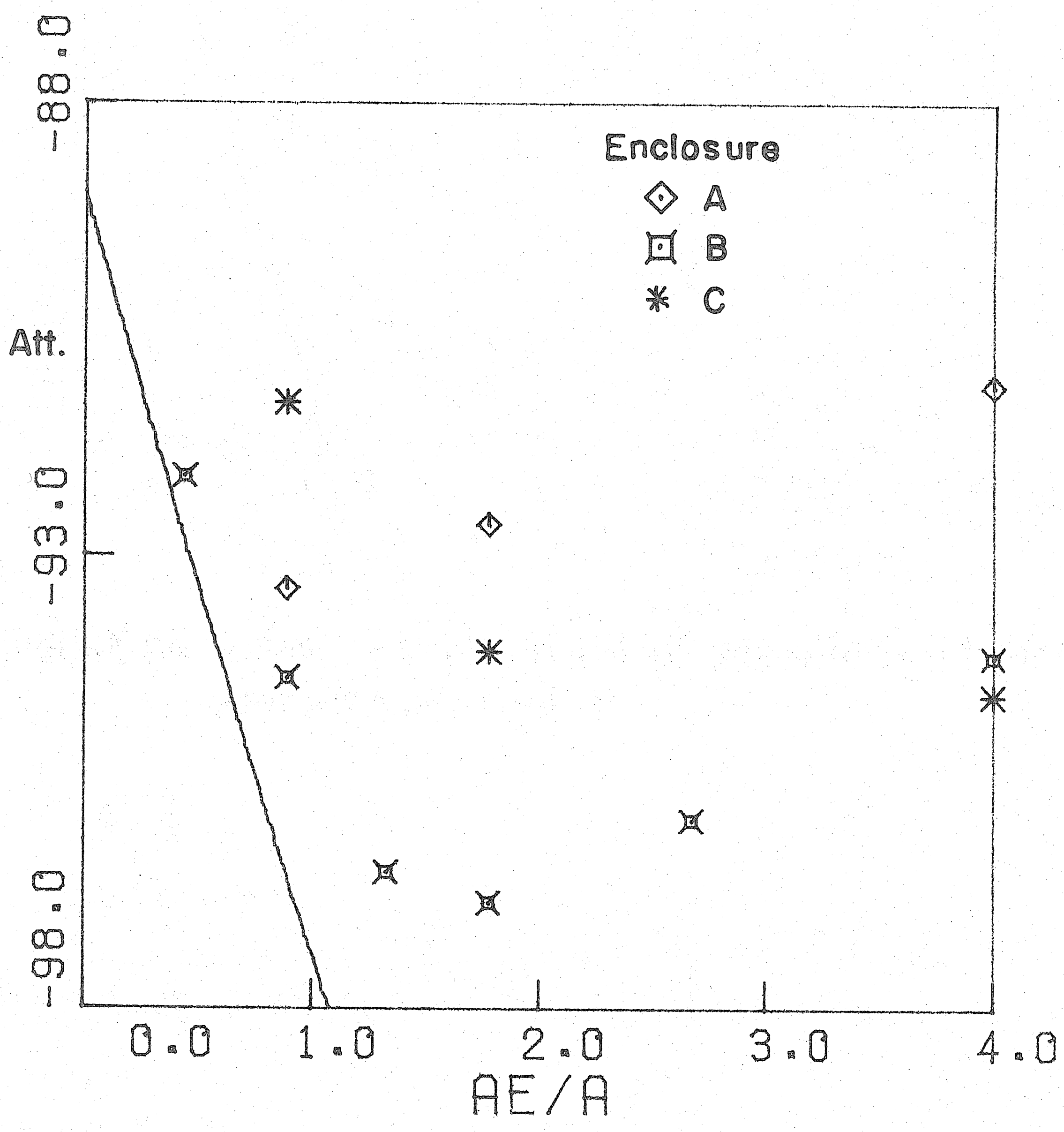

FIGURE 66 SOUND ATTENUATION BY PERFORATED TUBES, RESONANCE TUBE

in Section 5.2.1.

For small perforate area ratios, the enclosure has no effect on the attenuation. However, as the perforate area ratio increases, at some point the enclosure becomes important and prevents further increases in the attenuation. This perforate area ratio is denoted as critical. The critical point is a function of the enclosure area ratio, as can be seen in figure 65. Further, for a given enclosure, only small changes in attenuation are observed for perforate area ratios above critical.

The attenuation data from the repetitive-pulse experiments are consistent with the single-pulse data except for the largest enclosure. The data are compared with the theory of Section 3.5 in figure 66. Enclosures A and B have a critical area ratio similar to those observed in the single-pulse case. One distinct difference is apparent. The attenuation in the repetitive pulse case goes through a distinct maximum at the critical area ratio; whereas, in the single-pulse case, the attenuation simply asymptotes to a maximum at the critical area ratio. Enclosure C exhibits an additional anomaly in that each data point appears to be shifted to a lower attenuation than is consistent with the single-pulse data.

5.3 Sound Attenuation by Expansion Chambers

The sound radiation produced by the transmission of a shock through an expansion chamber muffler system is presented in this section. In particular, expansion chambers with and without inlets or outlets extended were excited by single and repetitive pulses, the amplitude of which varied almost one order of magnitude.

Measurements of radiated wave forms and SPL's are presented and compared with theory.

5.3.1 Wave Forms

Typical radiated pressure histories (location F) for expansion chambers with and without inlets or outlets extended were presented in figures 48, 49, and 50. For the expansion chamber B, figure 48, the pulses created by the series of transmitted shocks can be seen. However, there is additional pressure oscillation between the radiated pulses. This is even more pronounced for larger area ratios, as shown in figure 51, expansion chamber C. The internal shock dynamics, causing a sawtooth wave form in the tailpipe, is discussed in Section 4.2.1. The sawtooth wave form is responsible for the pressure fluctuation between the radiated pulses. The case of expansion chamber B with extended inlet is shown in figure 49. The spacing between the radiated pulses is reduced, because the extension causes new waves to appear in the transmitted wave form (c.f. figure 26). The case of expansion chamber B with extended outlet is shown in figure 50. The additional radiated pulses are stronger for the case of extended outlets than inlets because of the internal nonlinear interactions (Section 4.2.2).

5.3.2 Sound Pressure Levels

A comparison of measured and predicted values of the SPL, produced by the transmission of a shock through an expansion chamber muffler system, is presented in this section. Also, results from repetitive and single-pulse excitation experiments are compared.

For the case of the expansion chamber, the attenuation is plotted against area ratio in figures 67 and 68 for single and repetitive pulse excitation, respectively. The single pulse measurements show an attenuation of 65 decibels at 34.6 diameters for the case when the area ratio is one, which is in agreement with the predicted value. Increasing the area ratio increases the attenuation; however, the measured increase is not as large as the theory predicts. This discrepancy is due to diffracted waves inside the muffler (Section 4.2.1). There seems to be no strong dependence on shock Mach number; for each area ratio, the measured SPL's are within one decibel. Qualitatively, the same results are shown in figure 68 for repetitive-pulse excitation.

For expansion chambers with extended inlet, two effects are observed. As shown in figure 69 for single-pulse excitation, the effects of diffraction reduce the expected increase of attenuation with area ratio. Also, the effect of amplitude (shock Mach number) is important. The performance of the inlet extension deteriorates rapidly with increasing amplitude (Fig. 53). This loss of performance has a pronounced effect on the resultant attenuation. For small area ratio, the attenuation decreases one decibel from $M_s = 1.17$ to $M_s = 1.26$; and for large area ratio, the equivalent decrease is four decibels.

The same effects are shown for expansion chambers with extended outlets in figure 70. Again, relatively small differences between predictions and measurements for low shock strengths, due to diffraction effects, are observed; and larger discrepancies are observed for stronger shocks.

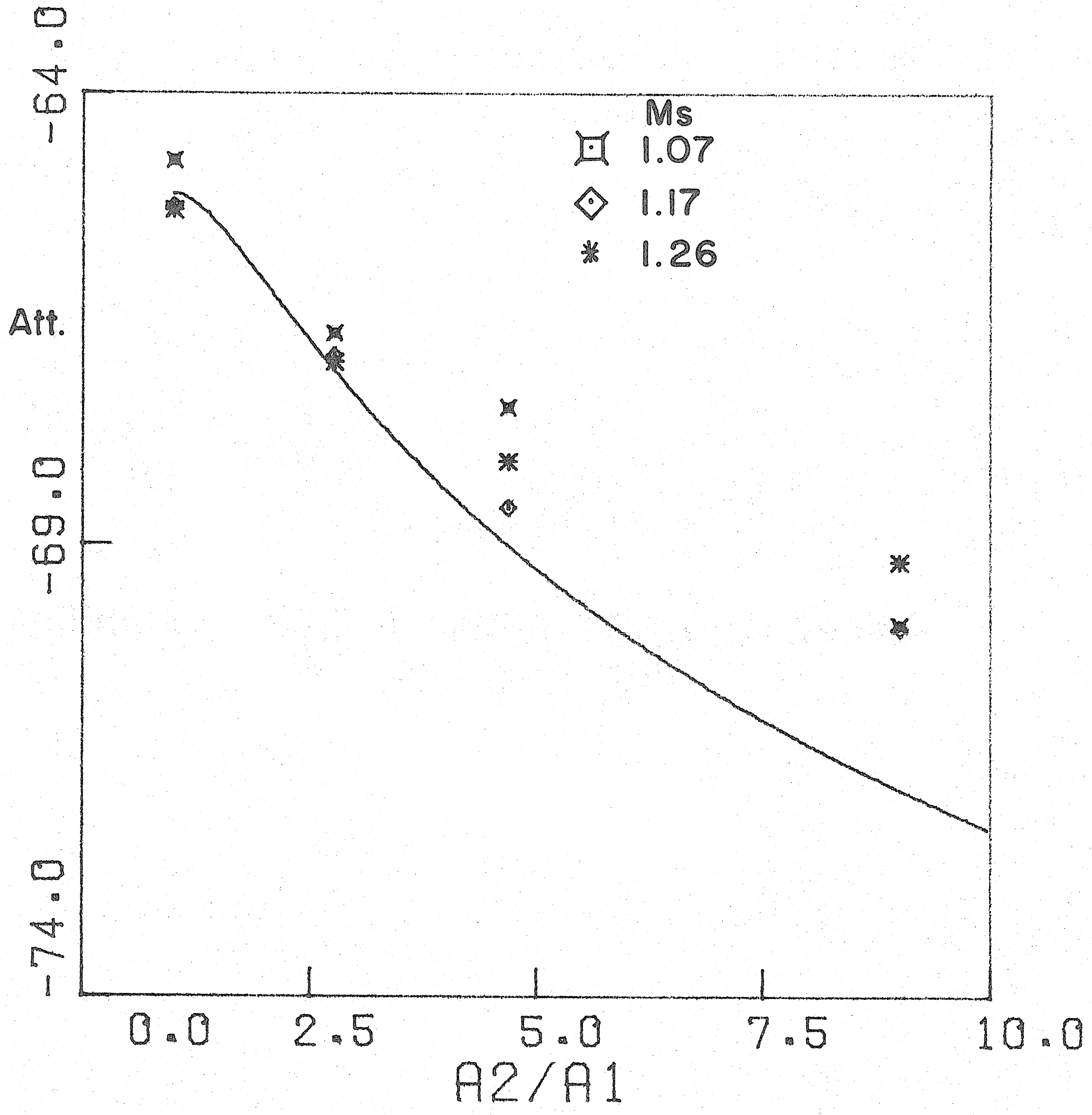

FIGURE 67 SOUND ATTENUATION BY EXPANSION CHAMBERS, SHOCK TUBE

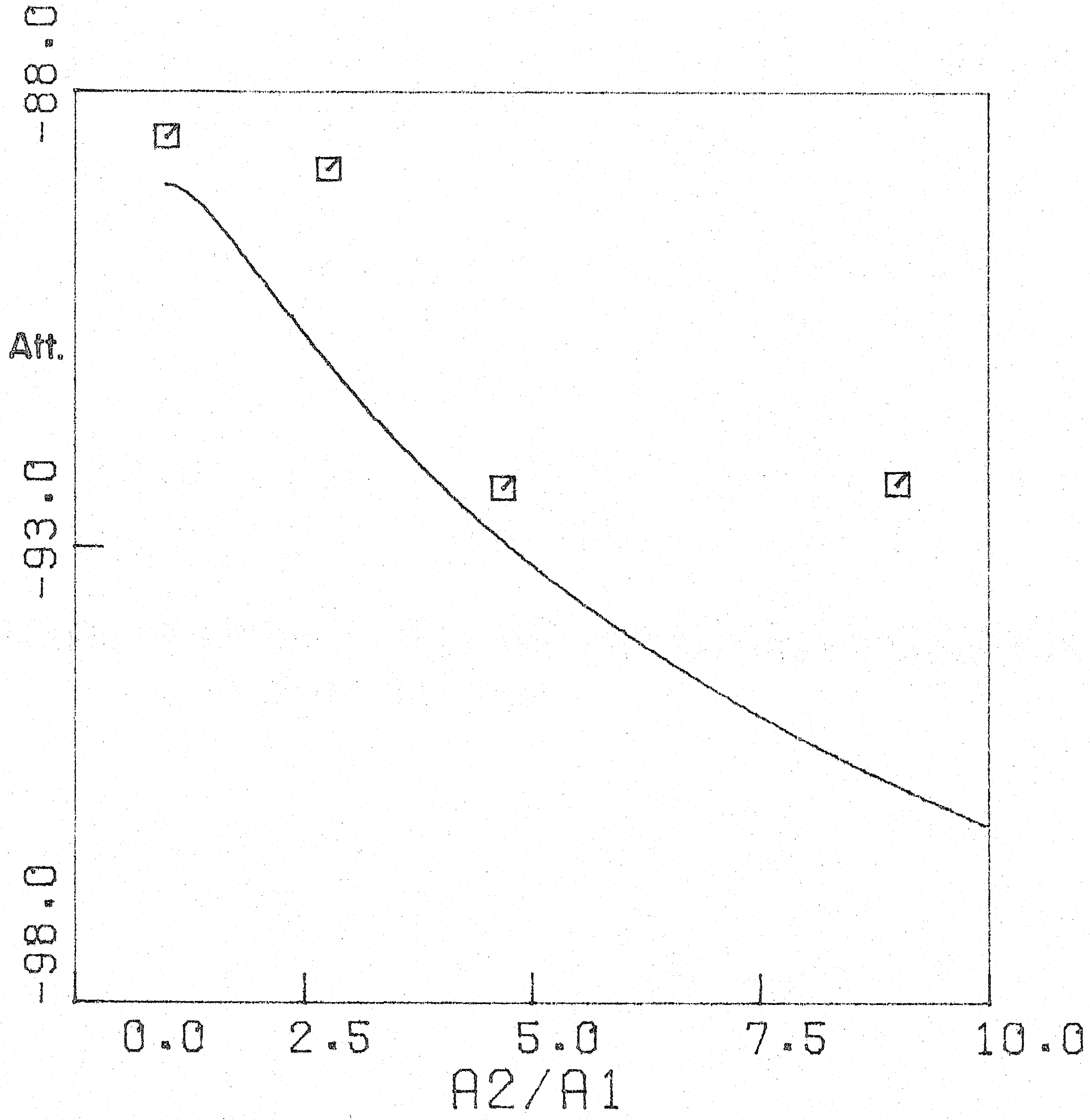

FIGURE 68 SOUND ATTENUATION BY EXPANSION CHAMBERS, RESONANCE TUBE

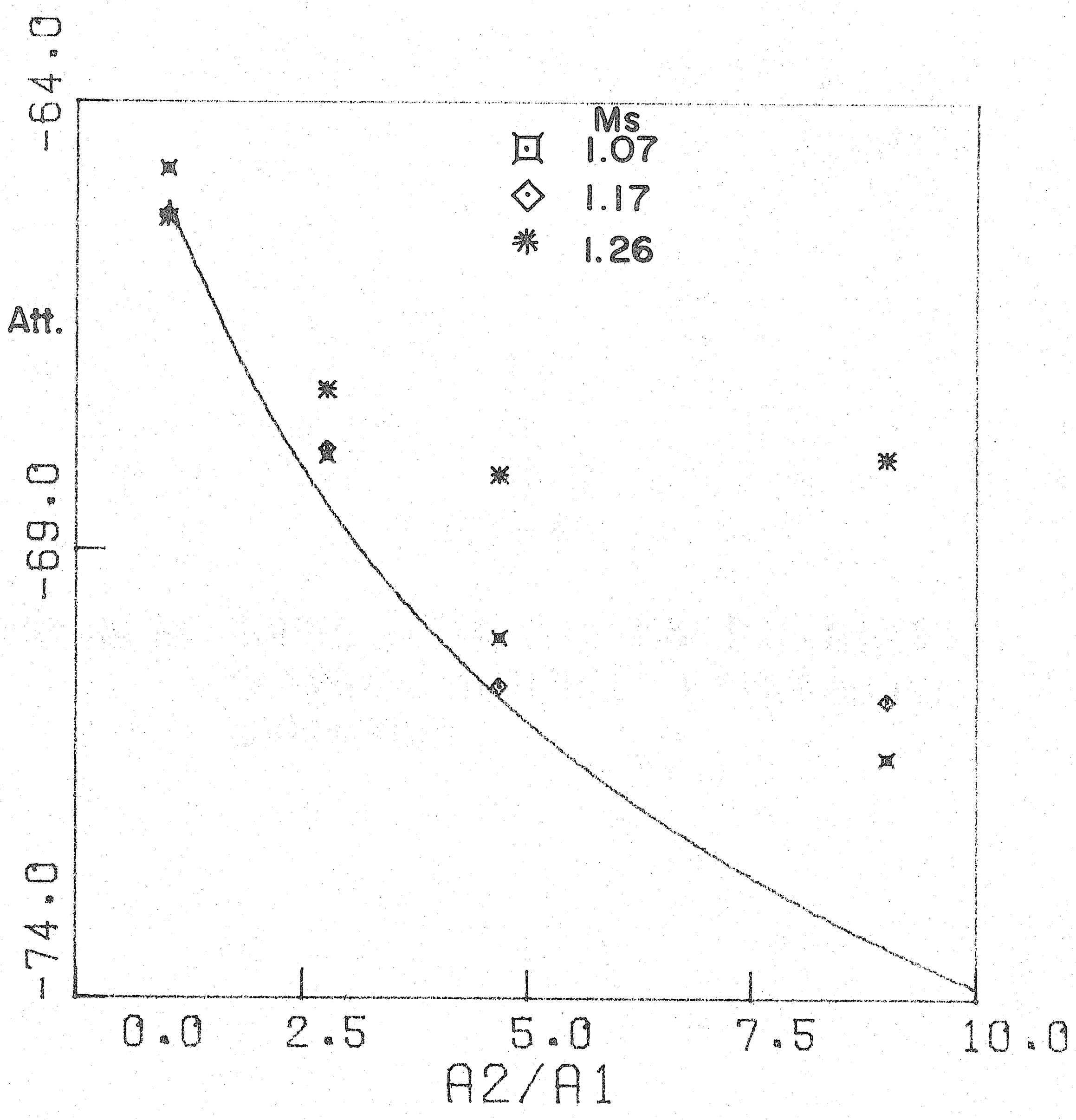

FIGURE 69 SOUND ATTENUATION BY EXPANSION CHAMBERS WITH INLET EXTENSIONS, SHOCK TUBE

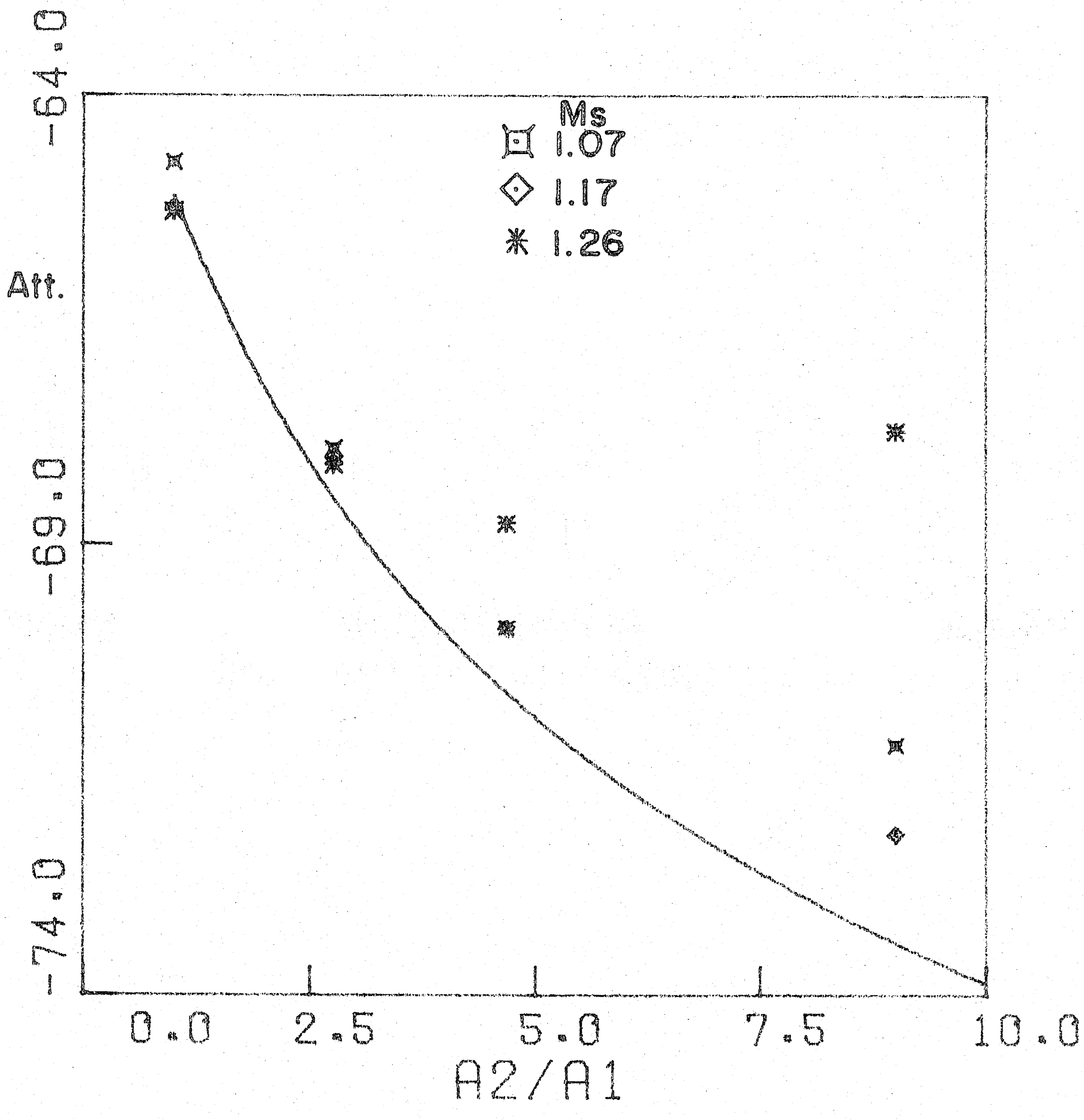

FIGURE 70 SOUND ATTENUATION BY EXPANSION CHAMBERS WITH OUTLET EXTENSIONS

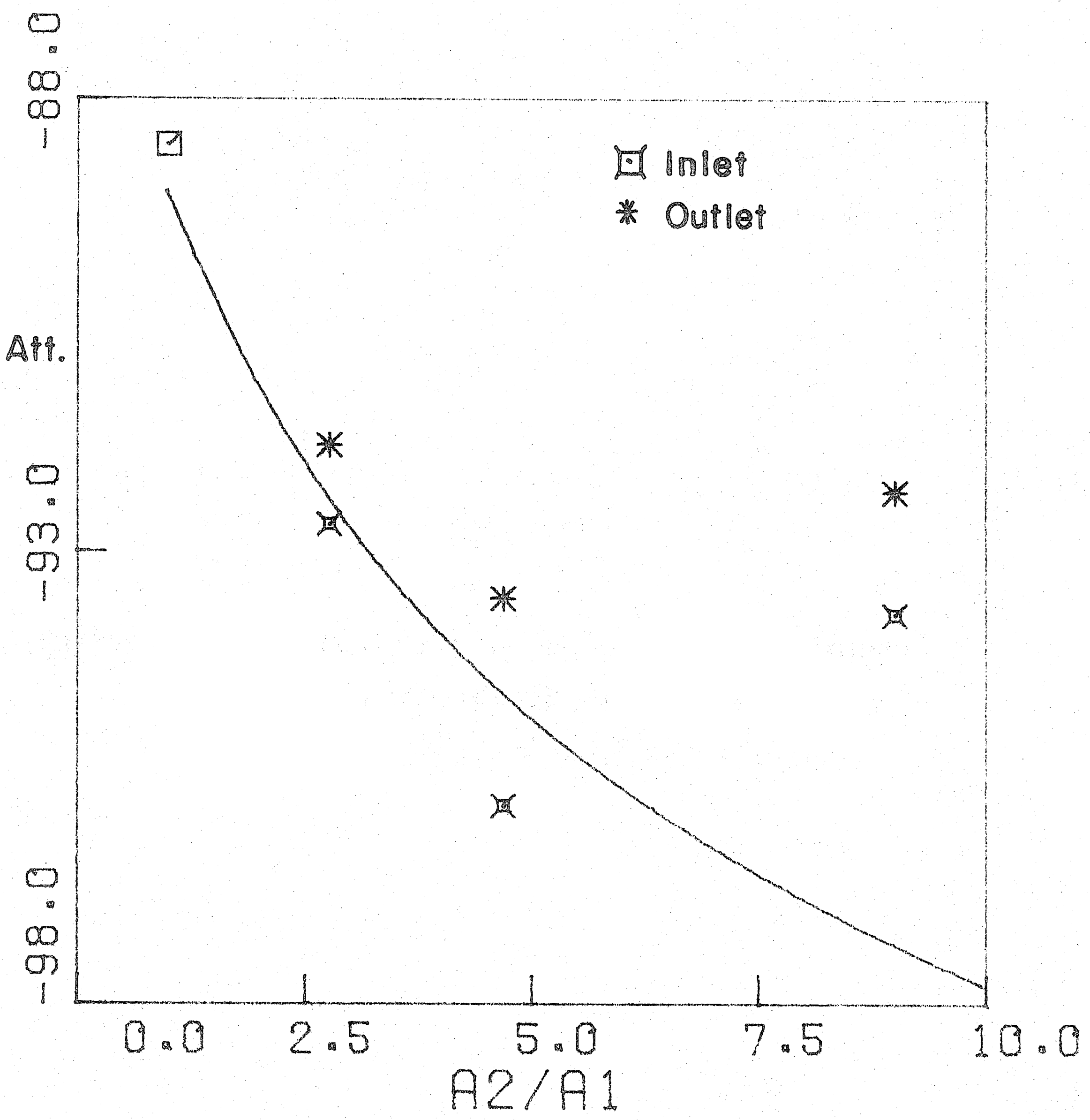

FIGURE 71 SOUND ATTENUATION BY EXPANSION CHAMBERS WITH INLET OR OUTLET EXTENSIONS, RESONANCE TUBE

Repetitive excitation results for expansion chambers with extended inlets and outlets are presented in figure 71. Interestingly enough, the inlet extension is the only case for which larger measured attenuations were observed than predicted. Quantitative agreement is shown for both extensions except for the largest area ratio. For the inlet extension, the discrepancy for the largest area ratio is about equal to that observed for single-pulse excitation. However, for the outlet extension, the discrepancy is more than twice that measured for single-pulse excitation.

VI. SUMMARY OF RESULTS

6.1 Internal Waves

6.1.1 Perforations

The strength of a shock wave after propagating through a length of perforated tubing and the rate at which the shock approaches its asymptotic strength depend on incident-shock strength and perforate area ratio. The attenuation is quite severe for weak incident shocks, but the asymptotic strength is achieved only at large distances. Conversely, for stronger shock waves, the attenuation is drastically reduced, but asymptotic strengths are observed at relatively small distances. The reduction in attenuation for stronger shock waves is caused by two mechanisms: (1) the basic nonlinearity of the Bernoulli equation describing the mass flux through the perforations, and (2) tilting of the jets through the perforations toward the downstream direction, with resultant reduction of their cross-sectional area.

When a length of perforated tubing is enclosed by an expansion chamber, we note two basic effects: (1) the amplitude of the primary disturbance is altered, and (2) additional disturbances re-enter the main tube from the enclosure and propagate in both the upstream and downstream directions. The effect that an enclosure has on the amplitude of the primary disturbance is not understood.

6.1.2 Expansion Chambers

As a result of a shock wave interacting with an expansion chamber with or without internal extensions, a series of disturbances are produced in the tailpipe and inlet pipe. The amplitude and form of the disturbances are dependent upon muffler geometry and incident-shock strength. The amplitude of each disturbance depends most strongly on the area ratio; however, its form is affected by the muffler length-to-diameter (aspect) ratio.

a.) Standard Expansion Chamber: For mufflers of moderate aspect ratio, measured transmission and reflection coefficients agree reasonably well with predictions for all shock strengths; however, for small aspect ratios, the predicted wave attenuation is not observed. This result is also noted in terms of radiated noise; that is, for small aspect ratios, the predicted noise attenuation is not observed. This disagreement is caused by the generation of diffracted waves which do not smooth out in short mufflers, but follow the initial disturbance down the tailpipe.

b.) Inlet Extension: As a result of the incident shock diffracting around the inlet extension, waves are propagated into the annulus and into the main chamber. For weak incident shocks, they are of equal strength as the theory predicts; however, for stronger incident shocks, the wave in the main chamber is much stronger than the wave in the annulus.

c.) Outlet Extension: When the incident shock arrives at the upstream junction, a wave is transmitted into the main chamber. The outlet extension allows a portion of the wave in the main chamber to pass without change into the tailpipe. The rest of the wave, which is in the annulus, reflects from the closed end . The interaction of the reflected wave with the outlet extension depends on the details of the diffraction process. A portion of the reflected wave is diffracted into the outlet extension, and the rest continues upstream into the main chamber. Observations of transmitted waves indicate that the interaction with the outlet extension is less dependent upon incident shock strength than the equivalent interaction with the inlet extension.

6.2 External Waves

The sound radiated by the arrival of a weak shock at the open end of a circular duct is a narrow pulse. Acoustic theory says that the pulse width should vary significantly with viewing angle, but observations have shown only small changes. The wave form is symmetric at 90° to the tube axis, while on the tube axis the wave form contains a shock. The amplitude in the near field is quite directional (larger on the axis than at 90°).

As a result of inserting a muffler system between the source (exhaust port) and the tailpipe exit, the radiated sound per unit of incident shock amplitude is reduced. The effect of the muffler system is to transform each incident shock into a series of shocks in the tailpipe or, more importantly, to transform the virtual source strength of the incident shock into a series of weaker sources.

6.2.1 Perforations

Long sections of perforations severely attenuate weak shocks, but, even more important, they change the rise time of the transmitted wave. The rise time of a strongly attenuated transmitted wave is $O(2L/a)$, where the length of the perforated section is L and the speed of sound is a. Increased rise times cause substantial decreases in the amplitude of the radiated pulse. We have observed a reduction in pulse amplitude of a factor of eight for a rise time of eight D/a, where the tube diameter is D.

Enclosures have no effect on the sound attenuation for small perforate area ratios; however, as the perforate area ratio increases, the enclosure eventually inhibits further increase in the sound attenuation. Beyond the critical perforate area ratio, the sound attenuation depends only on the enclosure volume, and for a given enclosure, the maximum sound attenuation for an incident shock Mach number of 1.17 is 1.1 decibels per unit of enclosure area ratio greater than unity.

6.2.2 Expansion Chambers

The sound radiation produced by the transmission of a shock through an expansion chamber can be predicted for large aspect ratios; however, for small aspect ratios, corrections must be made to account for internal diffracted waves. These results are independent of incident shock strength for Mach numbers between 1.07 and 1.26.

For expansion chambers with internal extensions, sound attenuation is increased for low incident shock strength; while for increasing incident shock strength, the internal transmission characteristics deteriorate, thus reducing the sound attenuation.

6.3 Applications

Results from this work can be incorporated into muffler design in three ways: (1) the basic single pulse scheme provides a simplified method for estimating sound attenuation, (2) new designs may be motivated by some of the general results, and (3) direct use of specific results.

The single pulse approach can be used to compare new designs, as has been done in this work for conventional designs (expansion chambers with and without extensions). There are several general results which can possibly lead to new designs. (1) Near large area changes, diffraction effects cause the transmitted shock front to be stronger on the axis than off the axis (Section 5. 1). (2) Thickening the transmitted wave front, reduces the sound radiation (Section 5. 2). Theoretically, the amplitude of the pressure pulse radiated by the arrival of a shock at an opening in a tube is related to an included angle of dependence, Ψ (Section 3. 5).

There may be a number of ways to thicken the transmitted wave; one example is a long section of perforated tubing. The mechanism which is responsible for thickening the wave is discussed in Section 4. 1. In addition to extending the time dependence of the wave, possibly the open end geometry can be designed to spread the spatial dependence of the radiation to the free field. The effect of a new open end geometry could be evaluated using the results of Section 3. 5. Side exits in mufflers, rather than downstream exits, have been investigated by Kelsay (1975). A careful look at wave diffraction effects at corners may be the key to improving the side exit configurations.

Specific results suggest that: (1) perforations should be used downstream of area changes because of nonlinear effects (Section 3. 2), (2) when the length of the enclosure is twice the length of the perforated section of tubing, the transmitted waves have equal spacing (Fig. 44), (3) to enhance the thickening effect, perforations should extend for several tube diameters and (4) short tailpipes will reduce the ability of transmitted waves to coalesce, which will reduce the sound attenuation.

APPENDIX A

NUMERICAL SOLUTION OF SECOND ORDER EQUATIONS

The equations governing the interaction of a weak shock with a perforate tube are derived in section 3.2. Retaining the second order terms in the steady flow equations accounts for the recovery of dynamic pressure in the downstream tube. The total pressure in region 3 is used to compute the pressure drop, or the exit velocity, rather than the static pressure.

The second order set of equations,

$$\begin{aligned} \frac{a}{2}B^2(R-1)^2 + B^2(R+1) - \frac{a}{2}(1-R-T)^2 &= 0 \\ \frac{a}{2}B^2\,T^2 + B^2\,T - \frac{a}{2}(1-R-T)^2 &= 0 \end{aligned} \tag{A.1}$$

is solved using a modified Newton's method for systems of equations given in Ref. 7. The method is used to find the solution of a system of equations of the form

$$\underset{\sim}{f}(\underset{\sim}{x}) = 0 \tag{A.2}$$

where $\underset{\sim}{f}$ is a N component vector composed of functions $f_i(\underset{\sim}{x})$. (N is two in this case.) The method finds the solution vectors by solving a similar equation,

$$\underset{\sim}{g}(\underset{\sim}{x}) = \underset{\sim}{x} - A\underset{\sim}{f}(\underset{\sim}{x}) \tag{A.3}$$

where A is a constant nonsingular n-th order matrix and $\underset{\sim}{g}(\underset{\sim}{x}) = \underset{\sim}{x}$, so that a solution vector of equation (A.3) is also a solution of vector equation (A.2). To solve equation (A.3) we guess initial solution vector, x^0, and computing

$$\underset{\sim}{g}(\underset{\sim}{x}) = \underset{\sim}{x}^{0} - A\underset{\sim}{f}(\underset{\sim}{x}^{0}) = \underset{\sim}{x}' \tag{A.4}$$

we use

$$\underset{\sim}{g}(\underset{\sim}{x}^{\nu+1}) = \underset{\sim}{x}^{\nu} - A\,\underset{\sim}{f}(\underset{\sim}{x}^{\nu}) = x^{\nu+1} \qquad (A.5)$$

for the iteration scheme. It can be shown that the method will converge to the solution vector, $\underset{\sim}{x}^*$, when

$$G(x) = \frac{\partial}{\partial X_J} g_i(\underset{\sim}{x}) = I - A\frac{\partial}{\partial X_J} f_i(\underset{\sim}{x}) \qquad (A.6)$$

is sufficiently small. G(x), in the matrix norm sense, must be small, which is the case when the constant matrix, A, is approximately the inverse of the nonsingular Jacobian matrix. Therefore, Newton's method puts

$$A = J(x^{\nu})^{-1} \qquad (A.7)$$

or rewriting equation (A.5),

$$\underset{\sim}{g}(\underset{\sim}{x}^{\nu+1}) = \underset{\sim}{x}^{\nu} - J(x^{\nu})^{-1}\cdot\underset{\sim}{f}(\underset{\sim}{x}^{\nu}) = \underset{\sim}{x}^{\nu+1} \qquad (A.8)$$

Hence we only need solve

$$J(\underset{\sim}{x}^{\nu})\cdot\underset{\sim}{\delta}(\underset{\sim}{x}^{\nu+1}) = -\underset{\sim}{f}(\underset{\sim}{x}^{\nu}) \qquad (A.9)$$

where

$$\underset{\sim}{\delta}(\underset{\sim}{x}^{\nu+1}) = \underset{\sim}{x}^{\nu+1} - \underset{\sim}{x}^{\nu} \qquad (A.10)$$

This is a simple linear system of equations. In this case the functions are

$$f_1(x_1, x_2) = \frac{a}{2}B^2(X_1 - 1)^2 + B^2(X_1 + 1) - \frac{a}{2}(1 - X_1 - X_2)^2 = 0 \qquad (A.11a)$$

$$f_2(x_1, x_2) = \frac{a}{2}B^2(X_2)^2 + B^2(X_2) - \frac{a}{2}(1 - X_1 - X_2)^2 = 0 \qquad (A.11b)$$

and the components of the Jacobian Matrix are

$$J_{11}(\underset{\sim}{x}) = a B^2 (x_1 - 1) + B^2 + a(1 - x_1 - x_2)$$

$$J_{12}(\underset{\sim}{x}) = J_{21}(\underset{\sim}{x}) = a(1 - x_1 - x_2) \tag{A.12}$$

$$J_{22}(\underset{\sim}{x}) = a B^2 x_2 + B^2 + a(1 - x_1 - x_2)$$

and the solution vector, x*, is obtained by solving equation (A.9), which is

$$\underset{\sim}{\delta}(\underset{\sim}{x})^{\nu+1} = - J(\underset{\sim}{x}^{\nu})^{-1} \cdot \underset{\sim}{f}(\underset{\sim}{x}^{\nu}) \tag{A.13}$$

The code is programmed on Solo and computation is done in double precision arithmetic. Convergence is defined by

$$|\delta_1(\underset{\sim}{x}^{\nu})|^2 + |\delta_2(\underset{\sim}{x}^{\nu})|^2 < 10^{-10} \tag{A.14}$$

The equations are solved for x_1 and x_2 for various values of the parameters used in the experiments.

APPENDIX B

SHOCK TUBE DATA HANDLING PROGRAM

The major features of the flow past a section of perforated tube were established by calculating the flow conditions in regions 2 through 4 and the exit, from the wave amplitude data. The data handling program used the pressure in regions 1 through 4, the initial test section conditions, and the perforate area ratio to calculate Mach number, static and stagnation temperature, density and pressure, and exit mass flow.

Using the incident and transmitted shock amplitude,

$$\frac{\Delta P}{P} = \frac{2\gamma}{\gamma+1}\left(M_s^2 - 1\right) \tag{B.1}$$

the incident and transmitted shock Mach number was calculated. The shock Mach number is used to calculate the state variables and local Mach numbers in regions two and four.

$$u_2 = a_1 \left[\frac{2}{\gamma+1}\left(M_s - M_s^{-1}\right)\right] \tag{B.2a}$$

$$\rho_2 = \rho_1 \left[M_s / \left(M_s - u_2/a_1 \right) \right] \tag{B.2b}$$

$$a_2 = a_1 \left[1 + (\gamma-1)\, u_2/a_1 \left(M_s - \frac{1}{2}\, u_2/a_1 \right) \right]^{1/2} \tag{B.2c}$$

The conditions in region three are calculated using nonsteady expansion equations and isentropic relations to relate regions two and three.

$$a_3 = a_2 \left(P_3 / P_2 \right)^{\frac{\gamma-1}{2\gamma}} \tag{B.3a}$$

$$\rho_3 = \rho_2 \left(P_3 / P_2 \right)^{\frac{1}{\gamma}} \tag{B.3b}$$

$$u_3 = u_2 - \frac{2}{\gamma-1}\left(a_3 - a_2 \right) \tag{B.3c}$$

Now all the state variables and Mach numbers are known in regions one through four, which is sufficient to calculate the stagnation conditions in these regions.

$$P_o = P \left[1 + \frac{\gamma-1}{2} m^2 \right]^{\frac{-\gamma}{\gamma-1}} \tag{B.4a}$$

$$T_o = T \left[1 + \frac{\gamma-1}{2} m^2 \right]^{-1} \tag{B.4b}$$

$$\rho_o = \rho \left[1 + \frac{\gamma-1}{2} m^2 \right]^{\frac{-1}{\gamma-1}} \tag{B.4c}$$

$$a_o = a \left[T_o / T \right]^{\frac{1}{2}} \tag{B.4d}$$

Now the exit conditions are calculated assuming the flow expands to a subsonic Mach number isentropically from region three to atmospheric pressure. This is true only in the limit of infinitely thin walls.

$$m_e^2 = \frac{2}{\gamma-1} \left[1 - \left(P_1 / P_{03} \right)^{\frac{\gamma-1}{\gamma}}) \right] \tag{B.5a}$$

$$T_e = T_{03} \left[1 + \frac{\gamma-1}{2} m_e^2 \right] \tag{B.5b}$$

$$\rho_e = \rho_{03} \left[1 + \frac{\gamma-1}{2} m_e^2 \right]^{\frac{1}{\gamma-1}} \tag{B.5c}$$

$$a_e = a_{03} \left[T_e / T_{03} \right]^{\frac{1}{2}} \tag{B.5d}$$

With the exit flow conditions, the discharge coefficient, σ , is given by

$$\sigma = A \left(\rho_3 u_3 - \rho_4 u_4 \right) / A_e \rho_e u_e \tag{B.6}$$

the ratio of actual to ideal exit mass flow.

APPENDIX C

ESTIMATION OF INITIAL TEST SECTION CONDITIONS IN THE RESONANCE TUBE

The procedure, discussed in Section 4.1.3, to approximate the conditions in region one in the resonance tube uses the result from the shock tube runs that the stagnation pressure is constant between regions three and four.

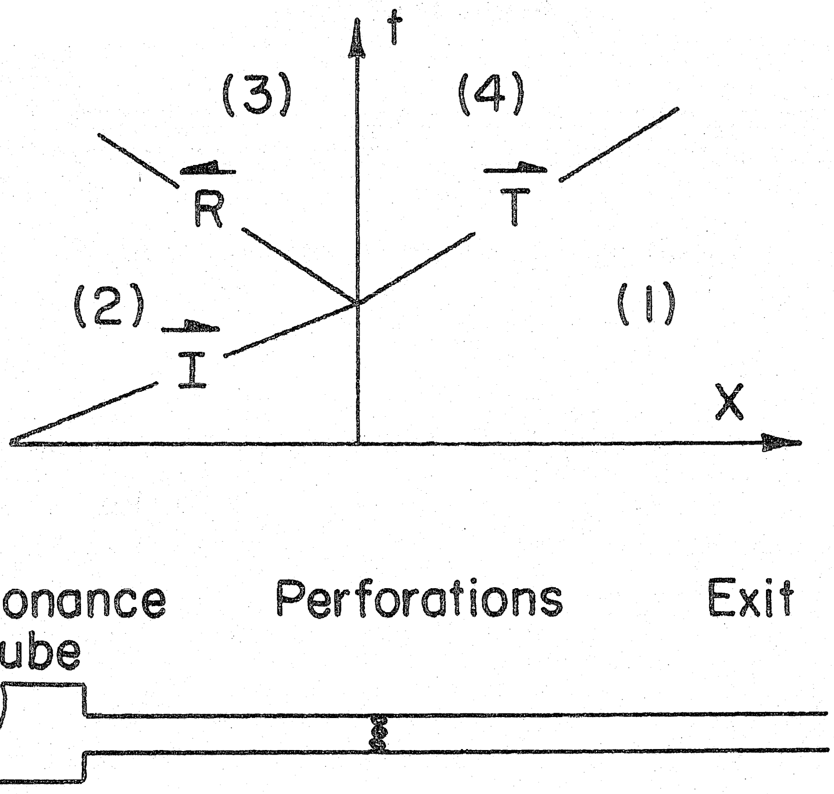

Positive velocity in positive X direction.

Figure 72

The velocities of interest are (e.g., figure 72)

U1 = UNKNOWN

$$U2 = \Delta u_i + u1$$

$$U3 = \Delta u_i + u1 - R\Delta u_i = (1-R)\Delta u_i + u1$$

$$U4 = T\Delta u_i + u1$$

where T and R are the measured values of the transmission and reflection coefficient. The restraint that the total pressure, the low Mach number approximation of the stagnation pressure, in regions three and four must be equal gives

$$P_4 + \tfrac{1}{2}\rho\,(T\Delta u_i + u1)^2 = P_3 + \tfrac{1}{2}\rho\left((1-R)\Delta u_i + u1\right)^2 \qquad \text{(C.1)}$$

or

$$\frac{u1}{\Delta u_i} = \frac{\left(\frac{P_4 - P_3}{\frac{1}{2}\rho\Delta u_i^2}\right) - (1-R)^2 + T^2}{2(1-R-T)} \qquad \text{(C.2)}$$

which is used to construct the following table.

TABLE 3

					(velocity ~ fps)				
RUN	(A_e/A)	ΔUi	T	R	U1	U2	U3	U4	σ
249	.89	213	.235	-.716	-243	-30	123	-193	1.01
250	.67	225	.516	-.627	-275	-50	90	-198	1.04
251	.44	241	.487	-.487	-262	-21	96	-144	1.08
252	.22	295	.688	-.277	-355	-60	21	-152	1.18
239	0				-321				

REFERENCES

1. Alfredson, R. J. and Davies, P. O. A. L. 1971 Performance of Exhaust Silencer Components. J. Sound and Vib. 15, 175.
2. Chester, W. 1949 The Propagation of a Sound Pulse in the Presence of a Semi-Infinite Open-Ended Channel. I. Royal Society of London, Phil. Trans. 242, 68.
3. Chester, W. 1964 Resonant Oscillations in Closed Tubes. J. Fluid Mech. 18, 44.
4. Chisnel, R. F. 1957 The Motion of a Shock Wave in a Channel, with Applications to Cylindrical and Spherical Waves. J. Fluid Mech. 2, 286.
5. Davies, P. O. A. L. 1964 The Design of Silencers for Internal Combustion Engines. J. Sound and Vib. 1, 185.
6. Davis, D. D. et al. 1954 Theoretical and Experimental Investigation Mufflers with Comments on Engine-exhaust Muffler Design. NACA Report 1192.
7. Honda, M. et al. 1974 Study on the Motion of Shock Waves Propagating along Perforated Ducts. Rep. Inst. High Speed Mech. Tohoku Univ. 30, 1.
8. Isaacson, E. and Keller, H. B. 1966 Analysis of Numerical Methods, Wiley, New York.
9. Jimenez, J. 1973 Nonlinear Gas Oscillations in Pipe, Part I. J. Fluid Mech. 59, 23.
10. Kelsay, R. E. and Margolis, D. An Experimental Investigation of Two-Stroke Internal Combustion Engine Performance. SAE Paper No. 750859.

REFERENCES (Cont'd)

11. Lettau, E. 1939.

12. Levine, H. and Schwinger, J. 1948 On the Radiation of Sound from an Unflanged Circular Pipe. Physics Review 73, 383.

13. Nomura, K. and Naitoh, H. 1971 Some Development Aspects of 2-Stroke Cycle Motorcycle Engines. SAE Trans. 80, 317.

14. Morse and Ingard 1968 Theoretical Acoustics, McGraw-Hill, New York.

15. Papoulis, A. 1962 The Fourier Transform and Its Applications, McGraw-Hill, New York.

16. Rayleigh, J. W. S. 1877 Theory of Sound, Dover, New York.

17. Rosciszewski, J. 1959 Calculations of the Motion of Non Uniform Shock Waves. J. Fluid Mech. 8, 337.

18. Rudinger, G. 1957 The Reflection of Pressure Waves of Finite Amplitude from an Open End of a Duct. J. Fluid Mech. 2, 48.

19. Sachs, M. P. and Allen, D. L. 1972 Effects of High-Intensity Sound on Muffler Element Performance. J. Acous. Soc. Amer. 52, 725.

20. Sloan, S. A. and Nettleton, M. A. 1975 J. Fluid Mech. 71, 769.

21. Smith, J. A. 1967 An Experimental Investigation of the Structure of Reflecting, Ionizing Shocks in Xenon. Ph.D. Thesis, Cal. Inst. of Tech.

22. Stewart, G. V. and Lindsay, R. B. 1930 Acoustics, D. Van Nostrand.

23. Stokes, G. M. et al. An Experimental Study of Porosity Characteristics of Perforated Materials in Normal and Parallel Flow.

REFERENCES (Cont'd)

NACA TN 3085.

24. Sturtevant, B. 1974 Nonlinear Gas Oscillations, Part II. J. Fluid Mech. 63, 97.

25. Szumowski, A. P. 1972 Motion of a Shock Wave Along a Perforated Duct. Prace Naukowe Mechanika, Politechnika Warszawska. Nr. 18. (Scientific Works Mechanics. Polytechnic Warsaw, Poland).

26. Troshin, V. I. 1959 Gas Flow through an Opening in a Channel Wall. PMM J. Appl. Math. and Mech. 23, 1340.

27. Whitham, G. B. 1957 A New Approach to Problems of Shock Dynamics, Part I. Two-Dimensional Problems. J. Fluid Mech. 2, 146.

28. Whitham, G. B. 1974 Linear and Nonlinear Waves, Wiley, New York.

29. Wu, J. H. T. and Ostrowski, P. P. 1971 "Shock Attenuation in a Perforated Duct," Shock Tube Research, Proceedings of the Eighth International Shock Tube Symposium, London, Chapman and Hall.